

NATIONAL CENTER FOR COMPUTATIONAL  
HYDROSCIENCE AND ENGINEERING

---

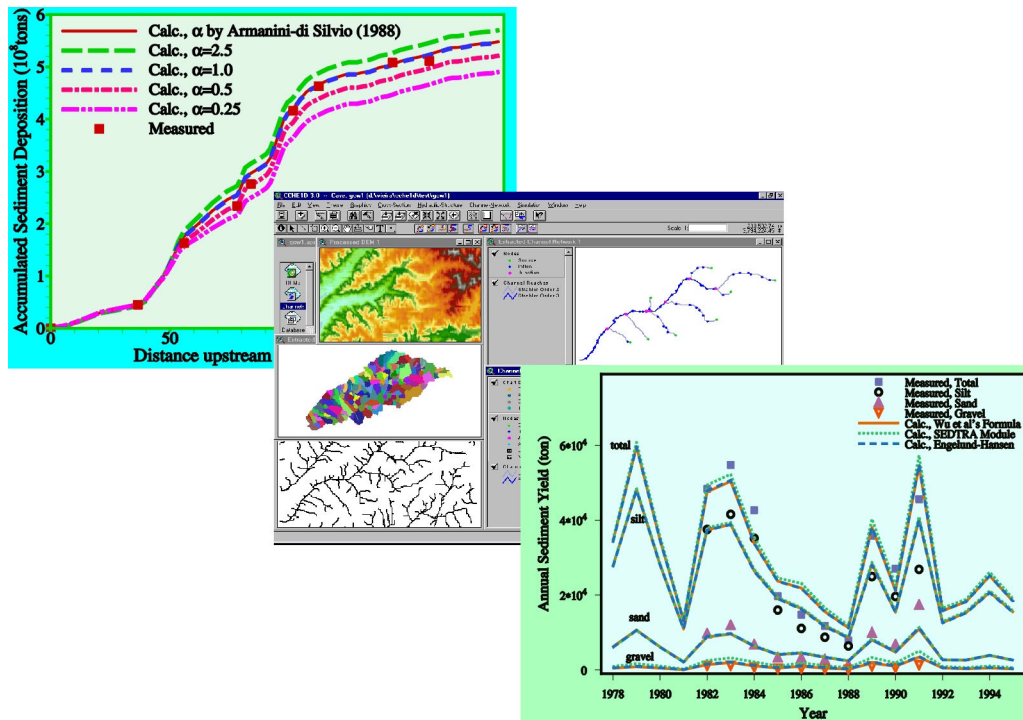
## One-Dimensional Channel Network Model CCHE1D Version 3.0 – Technical Manual

---

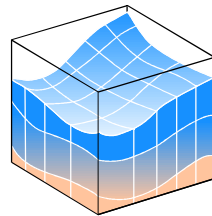
Technical Report No. NCCHE-TR-2002-1

January 2002

*Weiming Wu and Dalmo A. Vieira*



School of Engineering  
The University of Mississippi  
University, MS 38677



NATIONAL CENTER FOR COMPUTATIONAL  
HYDROSCIENCE AND ENGINEERING

Technical Report No. NCCHE-TR-2002-1

One-Dimensional Channel Network Model  
CCH1D 3.0 – Technical Manual

Weiming Wu, PhD  
Research Assistant Professor

Dalmo A. Vieira  
Research Associate

The University of Mississippi

January 2002

## Acknowledgements

CCHE1D 2.0 was based on the computational software DWAVENT and BEAMS, but it had significant improvements and many new features, such as dynamic wave model, non-equilibrium sediment transport model, semi-coupled numerical solution procedure and multiple options for flow and sediment calculations. CCHE1D 3.0 is a further updated version, which implements the general cross-section definition method, the hybrid dynamic/diffusive model, the digitizing interface, etc., for more general applications.

CCHE1D is a result of the research project sponsored by the USDA Agricultural Research Service under Specific Research Agreement No. 58-6408-7-035 and The University of Mississippi, and monitored by the USDA-ARS National Sedimentation Laboratory. Dr. Eddy J. Langendoen, Dr. Ligeng Li, Dr. Donghuo Zhou, Dr. Yun Zhang, Dr. Abdul Khan and Mr. Fernando Toro are acknowledged for their contributions. Dr. Ronald Bingner of the USDA National Sedimentation Laboratory is also acknowledged for his professional consultation and help. This work is supervised by Prof. Dr. Sam S.Y. Wang.

## Disclaimer

The CCHE1D model (version 3.0) was developed by the National Center for Computational Hydroscience and Engineering (NCCHE) of The University of Mississippi. CCHE1D is a complex program that requires engineering expertise to be used correctly. The reliability and accuracy of any results obtained from CCHE1D should be carefully examined by experienced engineers.

## Contents

Chapter 1	Introduction.....	1
1.1	Background of the CCHE1D Project.....	1
1.2	Components and Capabilities of CCHE1D Model .....	2
1.3	Limitations of CCHE1D Model.....	3
1.4	Contents of This Manual.....	3
Chapter 2	Channel Network Delineation and Cross Section Definition .....	4
2.1	Channel Network Delineation .....	4
2.2	Cross Section Definition.....	5
Chapter 3	1-D Hydrodynamic Model.....	7
3.1	Governing Equations for Open-Channel Flows.....	7
3.1.1	Dynamic Wave Model .....	7
3.1.2	Diffusive Wave Model.....	7
3.2	Discretization of Governing Equations.....	8
3.3	Iteration Scheme and Linearization .....	9
3.4	Solution Algorithm .....	12
3.5	Boundary Conditions .....	13
3.5.1	Inflow Boundary Conditions.....	13
3.5.2	Outflow Boundary Conditions.....	13
3.5.3	Confluences.....	14
3.5.4	Hydraulic Structures .....	15
3.6	Supplemental Treatments for Flow Calculations.....	23
3.6.1	Friction Slope Formulation .....	23
3.6.2	Manning's Roughness Coefficient $n$ .....	24
3.6.3	Momentum Correction Factor $\beta$ .....	24
3.6.4	Handling of Small Flow Depth .....	24
3.6.5	Simulation of Transcritical Flow .....	25
Chapter 4	1-D Sediment Transport Model .....	26
4.1	Sediment Transport in Channels.....	26
4.1.1	Governing Equations for Sediment Transport .....	26
4.1.2	Discretization of Governing Equations.....	27
4.1.3	Solution of Algebraic Equations .....	29
4.1.4	Boundary Conditions .....	30
4.1.5	Properties of the Numerical Method.....	31
4.1.6	Comments on Sediment Calculation.....	35
4.2	Bank Erosion and Mass Failure .....	35

4.2.1 Bank Toe Erosion .....	35
4.2.2 Bank Mass Failure .....	36
4.3 Empirical Formulas for Sediment Transport .....	37
4.3.1 Sediment Transport Capacity Formulas.....	37
4.3.2 Bed-Material Porosity .....	43
4.3.3 Non-equilibrium Adaptation Length $L_s$ .....	44
4.3.4 Division between Wash Load and Bed-Material Load.....	46
4.3.5 Mixing Layer Thickness .....	47
4.3.6 Settling Velocity of Sediment Particles .....	47
4.4 Summary of the Options for Sediment Calculation.....	48
Chapter 5 Landscape Analysis and Watershed Modeling .....	50
5.1 Landscape Analysis .....	50
5.2 Watershed Modeling.....	50
Chapter 6 Basic Data Requirements.....	52
6.1 Geometric Data .....	52
6.1.1 Cross Section Data .....	52
6.1.2 Reach Length Data.....	52
6.1.3 Channel Roughness Data .....	52
6.1.4 Channel Junctions .....	53
6.2 Flow Data.....	53
6.2.1 Inflow Discharge Conditions .....	53
6.2.2 Outlet Boundary Conditions .....	53
6.3 Sediment Data .....	53
6.3.1 Sediment Properties .....	53
6.3.2 Inflow Sediment Data .....	54
6.3.3 Bed Material Data .....	54
6.3.4 Bank Material Data .....	54
6.4 Hydraulic Structure Data .....	54
6.4.1 Bridge Crossings .....	54
6.4.2 Culverts .....	54
6.4.3 Drop Structures .....	55
6.4.4 Measuring Flumes.....	55
6.5 Watershed Data .....	55
Chapter 7 Model Verification and Testing .....	56
7.1 Comparison of Diffusive and Dynamic Wave Models.....	56
7.1.1 Steady Backwater Profile due to Impoundment .....	56
7.1.2 Steady Flow through a Channel Contraction .....	59

7.1.4 Unsteady Flow in a Natural Channel Network .....	61
7.2 Test of Sediment Transport Capacity Formulas .....	63
7.3 Model Test against Experimental Data.....	66
7.3.1 Degradation of Channel Bed with Uniform Sediment.....	66
7.3.2 Degradation of Channel Bed with Non-uniform Sediment .....	71
7.3.3 Channel Aggradation due to Non-uniform Sediment Overloading .....	75
7.4 Model Test against Field Data .....	81
7.4.1 Flood Routing in the Pu-Tze River.....	81
7.4.2 Long-Term Sedimentation Process in the Danjiangkou Reservoir.....	84
7.4.3 Unsteady Flow and Sediment Transport in the East Fork River .....	89
Chapter 8 Model Applications.....	94
8.1 Model Application to Goodwin Creek Watershed .....	94
8.1.1 Watershed Description.....	94
8.1.2 Simulation Procedures and Results.....	94
8.1.3 Sensitivity Analysis .....	101
8.1.4 Effects of Hydraulic Structures on Erosion Control .....	110
8.2 Model Application to the Pa-Chang River .....	112
8.2.1 Case Description .....	112
8.2.2 Flood and Sediment Routing in the Pa-Chang River .....	112
8.2.3 Effectiveness of Channel-Stabilization Structures in the Pa-Chang River .....	115
References .....	117

## Chapter 1 Introduction

### 1.1 Background of the CCHE1D Project

The Demonstration Erosion Control (DEC) Project is an interagency cooperative effort among the US Army Corps of Engineers (COE), the Natural Resources Conservation Service (NRCS) and the Agricultural Research Service (ARS) of the US Department of Agriculture. As an experimental project, COE and NRCS installed a system of control structures, including low and high drop structures, bank stabilization works, levees, flood retarding structures and rise pipe structures, to reduce watershed and channel erosion in the foothills of the Yazoo basin in Mississippi, and have monitored and measured flow discharge, stage, and sediment yield. The National Center for Computational Hydroscience and Engineering (NCCHE) of the University of Mississippi, in cooperation with the USDA-ARS National Sedimentation Laboratory (NSL), developed the flow and sediment routing computer models DWAVENT (Diffusive WAVE model for channel NETworks, Langendeon, 1996) and BEAMS (Bed and Bank Erosion Analysis Model for Streams, Li et al., 1996; Zhang and Langendeon, 1997), which simulate the long-term effects of hydraulic structures on flow and sediment yield, to support the DEC project. Since 1998, a new one-dimensional numerical model for flow and sediment transport in channel networks, called CCHE1D, has been developed at NCCHE based on DWAVENT and BEAMS. The new flow model CCHE1DFL includes the diffusive wave model previously implemented in DWAVENT, and the dynamic wave model, which solves the full St. Venant equations. Because BEAMS uses an equilibrium sediment transport model, numerical instability may occur in cases of strongly non-equilibrium sediment transport (e.g., strong erosion and deposition). The new sediment transport model CCHE1DST solves this problem by adopting a non-equilibrium approach and a coupled procedure to calculate nonuniform sediment transport, bed change and bed material sorting. The CCHE1D model has more functionality, and is more general and reliable.

The CCHE2D version 2.0 was released to the public for  $\beta$ -testing in 2000. Since that, NCCHE has continued to develop and improve the CCHE1D channel network model, which resulted in the currently released version 3.0. A general cross-section definition method, which gives up the previous eight-nodes definition method and uses a variable number of nodes in each cross section, has been implemented in the CCHE1D version 3.0. A hybrid dynamic/diffusive wave model has been implemented to handle the transcritical flow problem. A new digitizing interface has been developed to help the user apply CCHE1D in more general situations. Also the CCHE1D version 3.0 has been tested in many more experimental and field cases.

## 1.2 Components and Capabilities of CCHE1D Model

The CCHE1D package integrates the flow model CCHE1DFL and the sediment transport model CCHE1DST with the landscape analysis tool TOPAZ (TOpographic PArameteriZation, Garbrecht and Martz, 1995) and the watershed models AGNPS (Agricultural Non-Point Source Pollution Model, Young et al., 1987; Bosch et al., 1998) and SWAT (Soil and Water Assessment Tool, Arnold et al, 1993) through a highly automated graphical user interface (GUI), shown in Fig. 1.1.

The CCHE1D flow model simulates unsteady flow in channel networks using either the diffusive wave model or the dynamic wave model, taking into account the difference between the flows in the main channel and flood plains of a compound channel, and the influence of hydraulic structures such as culverts, measuring flumes, bridge crossings and drop structures. For local supercritical and transcritical flows (without hydraulic jumps), the hybrid dynamic/diffusive wave is applied. The flow model can be used with or without sediment calculation.

The CCHE1D sediment transport model calculates nonuniform sediment transport in rivers and streams using the non-equilibrium transport model, and simulates bank erosion and channel widening process. In addition, multiple options for sediment-related parameters have been implemented. For example, sediment transport capacity can be calculated by four formulas: SEDTRA module (Garbrecht et al., 1995), Wu et al's formula (2000), the modified Ackers and White's 1973 formula (Proffitt and Sutherland, 1983), and the modified Engelund and Hansen's 1967 formula (with Wu et al's correction factor). The other parameters such as bed-material porosity, non-equilibrium adaptation length, wash-load size range and mixing layer thickness can also be calculated by existing formulas. The implementation of these multiple options allows the user to choose the most appropriate formulas for particular real-life problems, and allows the model to be widely used.

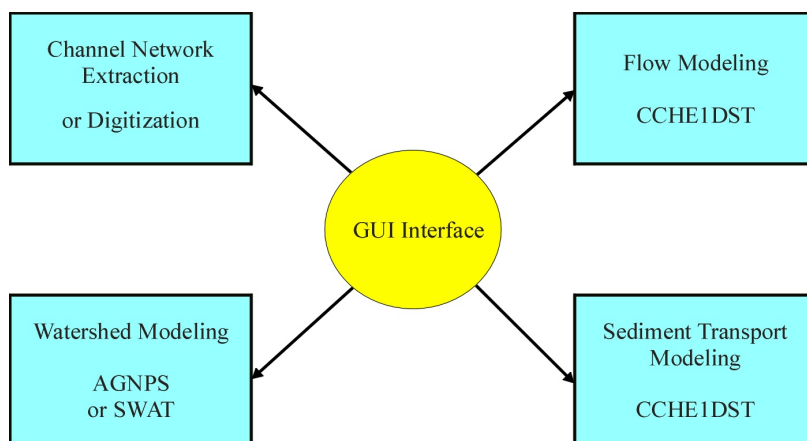


Fig. 1.1 Components of the CCHE1D Package

The landscape analysis model TOPAZ analyzes elevation data from a DEM (Digitized Elevation Model) to extract the channel network and its corresponding subcatchments. The watershed models AGNPS or SWAT calculate runoff and sediment yield for each subcatchment and provide inflow boundary conditions for the CCHE1D channel network model. The graphical user interface automatically performs most of the data operations such as conversions and transfers among the modeling components, consistency checks and storage.

### **1.3 Limitations of CCHE1D Model**

- (1). The CCHE1D flow model is currently preferred to simulate the subcritical flow in rivers and streams. It can also handle the local supercritical and transcritical flows without hydraulic jumps in isolated cross sections.
- (2). The CCHE1D model is currently limited to be applied to dendritic channel networks with single outlet only.
- (3). The CCHE1D model is a one-dimensional numerical model that should not be applied to situations where a truly two-dimensional or three-dimensional model is needed for detailed simulations of local conditions.
- (4). Application of the current version of CCHE1D model to river estuarine problems is not recommended.

### **1.4 Contents of This Manual**

This manual provides detailed technical information about the CCHE1D channel network model. The background of CCHE1D project, and the components, capabilities and limitations of the CCHE1D model are introduced in Chapter 1. Chapter 2 introduces the channel network delineation and cross section definition used in the CCHE1D model. Chapter 3 describes the hydrodynamic model, including governing equations, numerical method, solution algorithm, boundary conditions, the implementation of hydraulic structures, and supplemental treatments for flow calculation. Chapter 4 describes in detail the sediment transport model, including governing equations, numerical method, numerical stability analysis, bank erosion model, empirical formulas, and the multiple options for sediment calculation. Chapter 5 briefly introduces the software used in CCHE1D for landscape analysis and watershed modeling. Chapter 6 provides an overview of the basic data requirements of CCHE1D. Chapter 7 describes the verification and testing of the CCHE1D model. Chapter 8 introduces some applications of the CCHE1D model.

## Chapter 2 Channel Network Delineation and Cross Section Definition

### 2.1 Channel Network Delineation

Because of the presence of hydraulic structures, CCHE1D divides the channel network into several links, shown in Fig. 2.1. A link is either a hydraulic structure or a single channel consisting of several reaches. The reach is simply a stream segment between two cross sections (computational nodes). A channel link can start from a stream head, a hydraulic structure or a junction, and end at the watershed outlet, a hydraulic structure or a junction, but on its path there is no hydraulic structure or tributary to join in. The computational sequence of links is from tributaries to main streams, starting from the left lower side of the watershed, going counterclockwise through the entire watershed, and ending at the downstream main channel with watershed outlet. The computational nodes in one link are numbered from upstream to downstream. The hydraulic structure link contains three computational nodes: the last node of upstream link, a node for itself and the first node of downstream link. The arrangement of computational nodes at the junction of two channels is shown in Fig. 2.1. The reach between two cross sections is a computational element, in which the finite difference method is adopted for calculating flow and sediment transport. Flow discharge, velocity, depth, sediment transport rate, bed deformation and etc. are defined at cross sections rather than reaches.

An important issue related to the channel network is landscape analysis and watershed modeling. The landscape analysis software TOPAZ is used to divide the watershed into subwatersheds, and to extract the channel network from a DEM (Digital Elevation Model). This extraction process can be executed through the CCHE1D graphical user interface (GUI), which automatically defines the connectivity between the channel network and its corresponding subwatersheds. The reach lengths between cross sections are calculated by the TOPAZ according to the flow path. However, the accuracy of these reach lengths extracted by TOPAZ is limited by the resolution of DEM, which is usually around 30m. Therefore, the actually measured reach lengths can be provided by the user to enhance the quality of the geometric description of the channels. The runoff and sediment loads from subwatersheds can be simulated by the watershed models AGNPS or SWAT, and then distributed to the corresponding computational nodes as inflow for the channel network modeling.

CCHE1D can also be used to simulate the flow and sediment transport in a single channel, or in a general channel network independent of watershed modeling. In this case, the CCHE1D interface provides a digitizing tool to draw the channel network based on a reference photograph, GIS image, etc. The interface establishes the connectivity among channels and defines the main computational nodes. If the reference image is associated with a known coordinate system, CCHE1D can determine the channel reach lengths.

Otherwise, the user must provide the reach lengths. The inflow boundary conditions can be the measured data in this region, which the user should prepare.

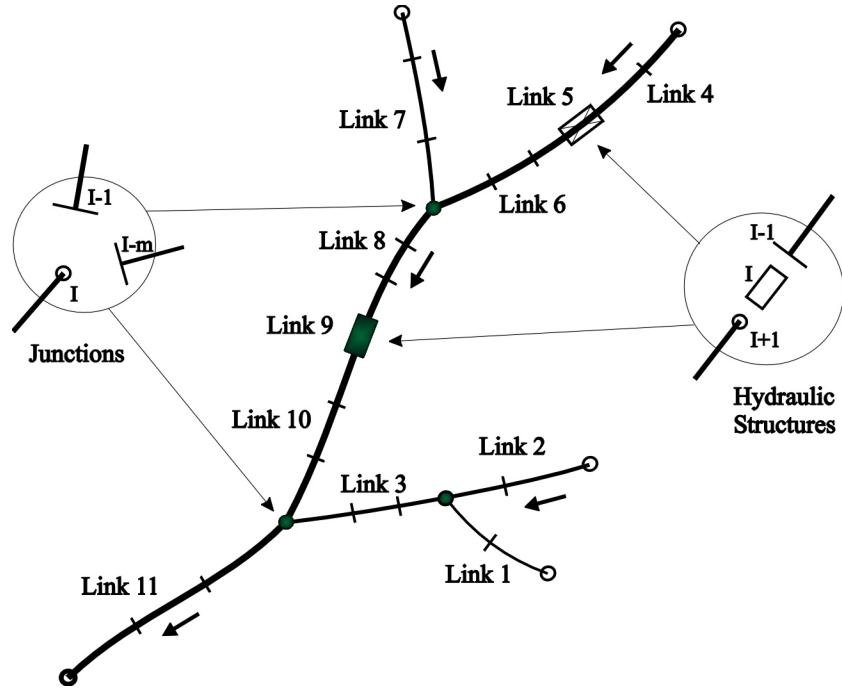


Fig. 2.1 Configuration of Channel Network

## 2.2 Cross Section Definition

In version 3.0 the cross-sectional profile is defined by a finite set of nodes (or stations), as shown in Fig. 2.2. The cross sections should be normal to the main flow direction. The number of nodes can be different in different cross sections, according to the complexity of the geometry. At each node, a pair of the bed elevation and the distance to the left bank is specified. At each segment between two nodes, a value of Manning's roughness coefficient is specified. The variation of roughness in channel bed, banks and flood plains can be accounted for through the variable Manning's coefficient. In addition, the dead water zones, such as the zones with recirculation flow around structures, can be excluded in the calculation by blocking these zones out. A variable is set for this purpose, assuming the value 1 for the unblocked zones, and 0 for the blocked dead water zones.

The hydraulic properties, (e.g. flow area, top width and conveyance), of the main channel and flood plains may be markedly different. Therefore, the CCHE1D model divides the

channel cross section into three subsections: a main channel and optional right and left overbank channel subsections (see Fig. 2.2). The hydraulic properties are determined for each individual subsection instead of the conventional approach using single, lumped hydraulic properties. The conveyance  $K$  for the entire cross section is determined as

$$K = \sum_{l=1}^3 \frac{1}{n_l} A_l R_l^{2/3} = \sum_{l=1}^3 \frac{1}{n_l} A_l^{5/3} P_l^{-2/3} \quad (2.1)$$

where  $A_l$  is the flow area of subsection  $l$ ;  $R_l$  is the hydraulic radius;  $P_l$  is the wetted perimeter; and  $n_l$  is the Manning's roughness coefficient.  $l$  is the index for subsections 1, 2 and 3 (left flood plain, main channel and right flood plain, respectively).

In order to distinguish the channel bed, banks and flood plains, the user should specify the locations of the left floodplain (LFP) edge, the left bank toe, the right bank toe and the right floodplain (RFP) edge. This should be specified in the cross-section geometry file.

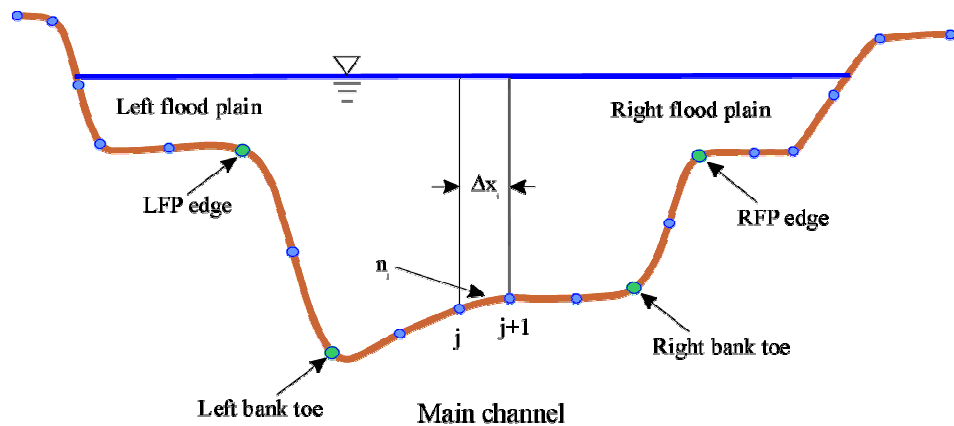


Fig. 2.2 Generalized Representation of Cross Section

## Chapter 3 1-D Hydrodynamic Model

### 3.1 Governing Equations for Open-Channel Flows

#### 3.1.1 Dynamic Wave Model

The governing equations of the dynamic wave model for open-channel flows are the St. Venant equations:

$$\frac{\partial A}{\partial t} + \frac{\partial Q}{\partial x} = q \quad (3.1)$$

$$\frac{\partial}{\partial t} \left( \frac{Q}{A} \right) + \frac{\partial}{\partial x} \left( \frac{\beta Q^2}{2A^2} \right) + g \frac{\partial h}{\partial x} + g(S_f - S_0) = 0 \quad (3.2)$$

where  $x$  and  $t$  are the spatial and temporal axes;  $A$  is the flow area;  $Q$  is the flow discharge;  $h$  is the flow depth;  $S_0$  is the bed slope;  $\beta$  is a correction coefficient for the momentum due to the nonuniformity of velocity distribution at the cross section;  $g$  is the gravitational acceleration; and  $q$  is the side discharge per unit channel length.  $S_f$  is the friction slope, defined as

$$S_f = Q|Q|/K^2 \quad (3.3)$$

where  $K$  is the conveyance, defined in Eq. (2.1).

#### 3.1.2 Diffusive Wave Model

Assuming the first two terms in Eq. (3.2) are negligible, the momentum equation for the diffusive wave model is written as

$$\frac{\partial h}{\partial x} + S_f - S_0 = 0 \quad (3.4)$$

This diffusive wave assumption is only applicable in cases where the inertia effects are not strong, for example, when the Froude number is less than 0.5, in general. However, in the case of nearly uniform flow, the diffusive wave model can be applied even when the Froude number is much larger than 0.5, because the first two terms in Eq. (3.2) become very small.

### 3.2 Discretization of Governing Equations

The implicit four-point finite difference scheme, first proposed by Preissmann (1961), is one of the most widely used in the numerical modeling of unsteady flows in open channels. This scheme replaces the continuous function  $f$  and its time and space derivatives by

$$f = \theta[\psi f_{j+1}^{n+1} + (1-\psi)f_j^{n+1}] + (1-\theta)[\psi f_{j+1}^n + (1-\psi)f_j^n] \quad (3.5)$$

$$\frac{\partial f}{\partial t} = \psi \frac{f_{j+1}^{n+1} - f_j^n}{\Delta t} + (1-\psi) \frac{f_j^{n+1} - f_j^n}{\Delta t} \quad (3.6)$$

$$\frac{\partial f}{\partial x} = \theta \frac{f_{j+1}^{n+1} - f_j^{n+1}}{\Delta x} + (1-\theta) \frac{f_{j+1}^n - f_j^n}{\Delta x} \quad (3.7)$$

where  $\theta$  and  $\psi$  are the temporal and spatial weighting coefficients in the Preissmann's scheme;  $n$  is the time step number;  $j$  is the spatial step number;  $\Delta t$  and  $\Delta x$  are the step lengths in time and space.

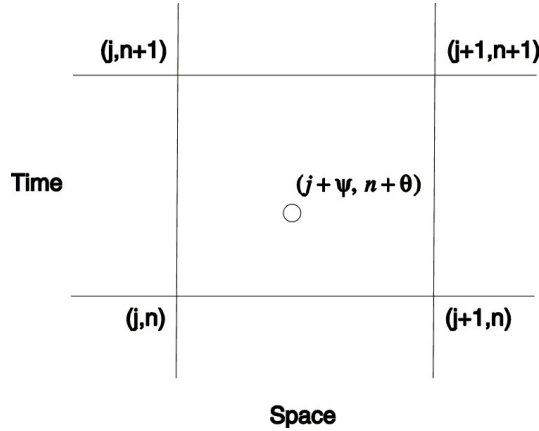


Fig. 3.1 Configuration of Computational Cell

Using the Preissmann's implicit scheme, the continuity equation (3.1) is discretized as

$$\begin{aligned} & \frac{\psi}{\Delta t} (A_{j+1}^{n+1} - A_j^n) + \frac{1-\psi}{\Delta t} (A_j^{n+1} - A_j^n) + \frac{\theta}{\Delta x} (Q_{j+1}^{n+1} - Q_j^{n+1}) + \frac{1-\theta}{\Delta x} (Q_{j+1}^n - Q_j^n) \\ & - \theta [\psi q_{j+1}^{n+1} + (1-\psi)q_j^{n+1}] - (1-\theta) [\psi q_{j+1}^n + (1-\psi)q_j^n] = 0 \end{aligned} \quad (3.8)$$

and the momentum equation (3.2) of the dynamic wave model is discretized as

$$\begin{aligned}
& \frac{\psi}{\Delta t} \left( \frac{Q_{j+1}^{n+1}}{A_{j+1}^{n+1}} - \frac{Q_j^n}{A_{j+1}^n} \right) + \frac{1-\psi}{\Delta t} \left( \frac{Q_j^{n+1}}{A_j^{n+1}} - \frac{Q_j^n}{A_j^n} \right) + \frac{\theta}{\Delta x} \left[ \frac{\beta_{j+1}^{n+1}}{2} \left( \frac{Q_{j+1}^{n+1}}{A_{j+1}^{n+1}} \right)^2 - \frac{\beta_j^{n+1}}{2} \left( \frac{Q_j^{n+1}}{A_j^{n+1}} \right)^2 \right] \\
& + \frac{1-\theta}{\Delta x} \left[ \frac{\beta_{j+1}^n}{2} \left( \frac{Q_{j+1}^n}{A_{j+1}^n} \right)^2 - \frac{\beta_j^n}{2} \left( \frac{Q_j^n}{A_j^n} \right)^2 \right] + \frac{\theta g}{\Delta x} (y_{j+1}^{n+1} - y_j^{n+1}) + \frac{(1-\theta)g}{\Delta x} (y_{j+1}^n - y_j^n) \\
& + \theta g [ \psi_R S_{f,j+1}^{n+1} + (1-\psi_R) S_{s,j}^{n+1} ] + (1-\theta) g [ \psi_R S_{f,j+1}^n + (1-\psi_R) S_{s,j}^n ] = 0
\end{aligned} \tag{3.9}$$

where  $y$  is the water surface elevation;  $\psi_R$  is the spatial coefficient for the friction slope in the case of small flow depth, and it may not be the same as  $\psi$  (see Section 3.6.4).

The discretized momentum equation for the diffusive wave model is Eq. (3.9) without the first four terms on the left-hand side.

Lyn and Goodwin (1987) investigated the numerical stability of the Preissmann's implicit scheme for St. Venant equations, and determined the necessary condition for numerical stability as

$$\left( \psi - \frac{1}{2} \right) / C_{ri} + \left( \theta - \frac{1}{2} \right) \geq 0 \tag{3.10}$$

where  $C_{ri}$  is the courant number,  $C_{ri} = \Delta t c_i / \Delta x$ ;  $c_i$  is a characteristic wave speed of St. Venant equations.

### 3.3 Iteration Scheme and Linearization

Because Eq. (3.9) is nonlinear, an iteration method is needed to solve the discretized continuity and momentum equations. Usually, two methods can be used to establish the iteration scheme. One method directly uses  $h$  and  $Q$  as dependent variables. The other method uses the increments  $\Delta h$  and  $\Delta Q$  as dependent variables. Both methods need linearization for the algebraic equations. The CCHE1D model adopts the second method. During the iteration process, it is desirable that accurate values are achieved within each iteration step. Therefore, the following relations are assumed,

$$A_j^{n+1} = A_j^* + \Delta A_j = A_j^* + B_j^* \Delta h_j \tag{3.11a}$$

$$Q_j^{n+1} = Q_j^* + \Delta Q_j \tag{3.11b}$$

where  $*$  denotes the variable values at the last iteration step;  $\Delta A$ ,  $\Delta h$  and  $\Delta Q$  are the increments of flow area, depth and discharge to be determined; and  $B$  is the channel width at water surface.

Substituting Eqs. (3.11a-b) into the discretized continuity equation, one can obtain the following iteration scheme:

$$\begin{aligned}
& \frac{\psi}{\Delta t} B_{j+1}^* \Delta h_{j+1} + \frac{1-\psi}{\Delta t} B_j^* \Delta h_j + \frac{\theta}{\Delta x} \Delta Q_{j+1} - \frac{\theta}{\Delta x} \Delta Q_j \\
& = -\frac{\psi}{\Delta t} (A_{j+1}^* - A_{j+1}^n) - \frac{1-\psi}{\Delta t} (A_j^* - A_j^n) - \frac{\theta}{\Delta x} (Q_{j+1}^* - Q_j^*) - \frac{1-\theta}{\Delta x} (Q_{j+1}^n - Q_j^n) \\
& \quad + \theta [\psi q_{j+1}^{n+1} + (1-\psi) q_j^{n+1}] + (1-\theta) [\psi q_{j+1}^n + (1-\psi) q_j^n]
\end{aligned} \tag{3.12}$$

The unknowns in Eq. (3.12) are  $\Delta h_j$ ,  $\Delta Q_j$ ,  $\Delta h_{j+1}$  and  $\Delta Q_{j+1}$ , so Eq. (3.12) can be re-written as

$$a_j \Delta h_j + b_j \Delta Q_j + c_j \Delta h_{j+1} + d_j \Delta Q_{j+1} = p_j \tag{3.13}$$

where

$$a_j = (1-\psi) B_j^* / \Delta t ;$$

$$b_j = -\theta / \Delta x ;$$

$$c_j = \psi B_{j+1}^* / \Delta t ;$$

$$d_j = \theta / \Delta x ;$$

$$\begin{aligned}
p_j = & -\frac{\psi}{\Delta t} (A_{j+1}^* - A_{j+1}^n) - \frac{1-\psi}{\Delta t} (A_j^* - A_j^n) - \frac{\theta}{\Delta x} (Q_{j+1}^* - Q_j^*) - \frac{1-\theta}{\Delta x} (Q_{j+1}^n - Q_j^n) \\
& + \theta [\psi q_{j+1}^{n+1} + (1-\psi) q_j^{n+1}] + (1-\theta) [\psi q_{j+1}^n + (1-\psi) q_j^n]
\end{aligned}$$

Similarly, to establish the iteration scheme for the discretized momentum equation, the following relations are used, some of them having been linearized:

$$y_j^{n+1} = y_j^* + \Delta h_j \tag{3.14a}$$

$$(Q_j^{n+1})^2 = (Q_j^*)^2 + 2Q_j^* \Delta Q_j \tag{3.14b}$$

$$\frac{1}{(K_j^{n+1})^2} = \frac{1}{(K_j^*)^2} - \frac{2}{(K_j^*)^3} \left( \frac{\partial K}{\partial h} \right)_j^* \Delta h_j \tag{3.14c}$$

$$S_{f,j}^{n+1} = S_{f,j}^* + \frac{2|Q_j^*|}{(K_j^*)^2} \Delta Q_j - \frac{2S_{f,j}^*}{K_j^*} \left( \frac{\partial K}{\partial h} \right)_j^* \Delta h_j \tag{3.14d}$$

$$\frac{Q_j^{n+1}}{A_j^{n+1}} = \frac{Q_j^*}{A_j^*} + \frac{1}{A_j^*} \Delta Q_j - \frac{Q_j^* B_j^*}{(A_j^*)^2} \Delta h_j \tag{3.14e}$$

$$\left( \frac{Q_j^{n+1}}{A_j^{n+1}} \right)^2 = \left( \frac{Q_j^*}{A_j^*} \right)^2 + \frac{2Q_j^*}{(A_j^*)^2} \Delta Q_j - \frac{2(Q_j^*)^2 B_j^*}{(A_j^*)^3} \Delta h_j \tag{3.14f}$$

$$\beta_j^{n+1} = \beta_j^* \quad (3.14g)$$

Substituting the equations (3.14) into Eq. (3.9) leads to the following iteration scheme for the discretized momentum equation of the dynamic wave model,

$$\begin{aligned}
& \left[ -\frac{1-\psi}{\Delta t} \frac{Q_j^* B_j^*}{(A_j^*)^2} + \frac{\theta}{\Delta x} \frac{\beta_j^* (Q_j^*)^2 B_j^*}{(A_j^*)^3} - \frac{\theta g}{\Delta x} - 2\theta(1-\psi_R)g \frac{S_{f,j}^*}{K_j^*} \left( \frac{\partial K}{\partial h} \right)_j^* \right] \Delta h_j \\
& + \left[ \frac{1-\psi}{\Delta t} \frac{1}{A_j^*} - \frac{\theta}{\Delta x} \frac{\beta_j^* Q_j^*}{(A_j^*)^2} + 2\theta(1-\psi_R)g \frac{|Q_j^*|}{(K_j^*)^2} \right] \Delta Q_j \\
& + \left[ -\frac{\psi}{\Delta t} \frac{Q_{j+1}^* B_{j+1}^*}{(A_{j+1}^*)^2} - \frac{\theta}{\Delta x} \frac{\beta_{j+1}^* (Q_{j+1}^*)^2 B_{j+1}^*}{(A_{j+1}^*)^3} + \frac{\theta g}{\Delta x} - 2\theta\psi_R g \frac{S_{f,j+1}^*}{K_{j+1}^*} \left( \frac{\partial K}{\partial h} \right)_{j+1}^* \right] \Delta h_{j+1} \\
& + \left[ \frac{\psi}{\Delta t} \frac{1}{A_{j+1}^*} + \frac{\theta}{\Delta x} \frac{\beta_{j+1}^* Q_{j+1}^*}{(A_{j+1}^*)^2} + 2\theta\psi_R g \frac{|Q_{j+1}^*|}{(K_{j+1}^*)^2} \right] \Delta Q_{j+1} \\
& = -\frac{\psi}{\Delta t} \left( \frac{Q_{j+1}^*}{A_{j+1}^*} - \frac{Q_{j+1}^n}{A_{j+1}^n} \right) - \frac{1-\psi}{\Delta t} \left( \frac{Q_j^*}{A_j^*} - \frac{Q_j^n}{A_j^n} \right) - \frac{\theta}{\Delta x} \left[ \frac{\beta_{j+1}^*}{2} \left( \frac{Q_{j+1}^*}{A_{j+1}^*} \right)^2 - \frac{\beta_j^*}{2} \left( \frac{Q_j^*}{A_j^*} \right)^2 \right] \\
& - \frac{1-\theta}{\Delta x} \left[ \frac{\beta_{j+1}^n}{2} \left( \frac{Q_{j+1}^n}{A_{j+1}^n} \right)^2 - \frac{\beta_j^n}{2} \left( \frac{Q_j^n}{A_j^n} \right)^2 \right] - \frac{\theta g}{\Delta x} (y_{j+1}^* - y_j^*) - \frac{(1-\theta)g}{\Delta x} (y_{j+1}^n - y_j^n) \\
& - \theta g [\psi_R S_{f,j+1}^* + (1-\psi_R)S_{s,j}^*] - (1-\theta)g [\psi_R S_{f,j+1}^n + (1-\psi_R)S_{s,j}^n] \quad (3.15)
\end{aligned}$$

Eq. (3.15) is rewritten as

$$e_j \Delta h_j + f_j \Delta Q_j + g_j \Delta h_{j+1} + w_j \Delta Q_{j+1} = r_j \quad (3.16)$$

where

$$\begin{aligned}
e_j &= -\frac{1-\psi}{\Delta t} \frac{Q_j^* B_j^*}{(A_j^*)^2} + \frac{\theta}{\Delta x} \frac{\beta_j^* (Q_j^*)^2 B_j^*}{(A_j^*)^3} - \frac{\theta g}{\Delta x} - 2\theta(1-\psi_R)g \frac{S_{f,j}^*}{K_j^*} \left( \frac{\partial K}{\partial h} \right)_j^*; \\
f_j &= \frac{1-\psi}{\Delta t} \frac{1}{A_j^*} - \frac{\theta}{\Delta x} \frac{\beta_j^* Q_j^*}{(A_j^*)^2} + 2\theta(1-\psi_R)g \frac{|Q_j^*|}{(K_j^*)^2}; \\
g_j &= -\frac{\psi}{\Delta t} \frac{Q_{j+1}^* B_{j+1}^*}{(A_{j+1}^*)^2} - \frac{\theta}{\Delta x} \frac{\beta_{j+1}^* (Q_{j+1}^*)^2 B_{j+1}^*}{(A_{j+1}^*)^3} + \frac{\theta g}{\Delta x} - 2\theta\psi_R g \frac{S_{f,j+1}^*}{K_{j+1}^*} \left( \frac{\partial K}{\partial h} \right)_{j+1}^*; \\
w_j &= \frac{\psi}{\Delta t} \frac{1}{A_{j+1}^*} + \frac{\theta}{\Delta x} \frac{\beta_{j+1}^* Q_{j+1}^*}{(A_{j+1}^*)^2} + 2\theta\psi_R g \frac{|Q_{j+1}^*|}{(K_{j+1}^*)^2};
\end{aligned}$$

$$\begin{aligned}
r_j = & -\frac{\psi}{\Delta t} \left( \frac{Q_{j+1}^*}{A_{j+1}^*} - \frac{Q_{j+1}^n}{A_{j+1}^n} \right) - \frac{1-\psi}{\Delta t} \left( \frac{Q_j^*}{A_j^*} - \frac{Q_j^n}{A_j^n} \right) - \frac{\theta}{\Delta x} \left[ \frac{\beta_{j+1}^*}{2} \left( \frac{Q_{j+1}^*}{A_{j+1}^*} \right)^2 - \frac{\beta_j^*}{2} \left( \frac{Q_j^*}{A_j^*} \right)^2 \right] \\
& - \frac{1-\theta}{\Delta x} \left[ \frac{\beta_{j+1}^n}{2} \left( \frac{Q_{j+1}^n}{A_{j+1}^n} \right)^2 - \frac{\beta_j^n}{2} \left( \frac{Q_j^n}{A_j^n} \right)^2 \right] - \frac{\theta g}{\Delta x} (y_{j+1}^* - y_j^*) - \frac{(1-\theta)g}{\Delta x} (y_{j+1}^n - y_j^n) \\
& - \theta g [\psi_R S_{f,j+1}^* + (1-\psi_R) S_{s,j}^*] - (1-\theta)g [\psi_R S_{f,j+1}^n + (1-\psi_R) S_{s,j}^n]
\end{aligned}$$

The iteration scheme for the discretized momentum equation of diffusive wave model is the same as Eq. (3.16) except that the coefficients are

$$\begin{aligned}
e_j &= -\frac{\theta g}{\Delta x} - 2\theta(1-\psi_R)g \frac{S_{f,j}^*}{K_j^*} \left( \frac{\partial K}{\partial h} \right)_j^*; \\
f_j &= 2\theta(1-\psi_R)g \frac{|Q_j^*|}{(K_j^*)^2}; \\
g_j &= \frac{\theta g}{\Delta x} - 2\theta\psi_R g \frac{S_{f,j+1}^*}{K_{j+1}^*} \left( \frac{\partial K}{\partial h} \right)_{j+1}^* \\
w_j &= 2\theta\psi_R g \frac{|Q_{j+1}^*|}{(K_{j+1}^*)^2}; \\
r_j &= -\frac{\theta g}{\Delta x} (y_{j+1}^* - y_j^*) - \frac{(1-\theta)g}{\Delta x} (y_{j+1}^n - y_j^n) - \theta g [\psi_R S_{f,j+1}^* + (1-\psi_R) S_{s,j}^*] \\
&\quad - (1-\theta)g [\psi_R S_{f,j+1}^n + (1-\psi_R) S_{s,j}^n]
\end{aligned}$$

### 3.4 Solution Algorithm

The pentadiagonal matrix consisting of iteration schemes (3.13) and (3.16) is solved with a double sweep algorithm.

A linear relationship between the unknowns  $\Delta h_j$  and  $\Delta Q_j$  is assumed to be of the type

$$\Delta Q_j = S_j \Delta h_j + T_j \quad (3.17)$$

Substituting Eq. (3.17) into Eqs. (3.13) and (3.16), and eliminating  $\Delta h_j$  yields

$$\Delta Q_{j+1} = S_{j+1} \Delta h_{j+1} + T_{j+1} \quad (3.18)$$

where

$$S_{j+1} = \frac{-(a_j + b_j S_j)g_j + (e_j + f_j S_j)c_j}{(a_j + b_j S_j)w_j - (e_j + f_j S_j)d_j} \quad (3.19)$$

$$T_{j+1} = \frac{(a_j + b_j S_j)(r_j - f_j T_j) - (e_j + f_j S_j)(p_j - b_j T_j)}{(a_j + b_j S_j)w_j - (e_j + f_j S_j)d_j} \quad (3.20)$$

In the first sweep, Eqs. (3.19) and (3.20) are applied recursively, with  $j$  varying from 1 to  $J-1$ , and  $S_1$  and  $T_1$  being specified by the upstream boundary conditions. Here  $J$  is the total number of computational nodes. In the second sweep,  $\Delta h_j$  can be calculated from

$$\Delta h_j = \frac{(p_j - b_j T_j) - (c_j \Delta h_{j+1} + d_j \Delta Q_{j+1})}{a_j + b_j S_j} \quad (3.21)$$

and  $\Delta Q_j$  from Eq. (3.17) by applying these equations recursively, with  $j$  from  $J-1$  to 1. The values of  $\Delta h_j$  and  $\Delta Q_j$  are specified by the downstream boundary conditions.

The iteration method performed at each time interval is stopped when the solutions of  $h$  and  $Q$  have converged ( $\Delta h \rightarrow 0$  and  $\Delta Q \rightarrow 0$ ).

### 3.5 Boundary Conditions

To solve the set of Eqs. (3.13) and (3.16) in case of subcritical flows, external boundary conditions have to be imposed at the upstream inlets and at the downstream outlet of the channel network, and internal boundary conditions are needed at confluences and at hydraulic structure locations.

#### 3.5.1 Inflow Boundary Conditions

A discharge hydrograph, which can be either a hypothetical hydrograph or a given time series of discharge, is needed at the upstream inflow boundary node of the channel network. The coefficients  $S_1$  and  $T_1$  in Eq. (3.17) are set as

$$S_1 = 0 \quad (3.22a)$$

$$T_1 = Q_1^{n+1} - Q_1^* \quad (3.22b)$$

#### 3.5.2 Outflow Boundary Conditions

At the downstream boundary node a stage-discharge curve or a time series of stage can be imposed. If the stage is specified, the discharge increment at the outflow boundary node can be readily calculated with

$$\Delta h_J = h_J^{n+1} - h_J^* \quad (3.23a)$$

$$\Delta Q_J = S_J \Delta h_J + T_J \quad (3.23b)$$

If a stage-discharge rating curve,  $Q = f(h)$ , is specified, a discretized equation for this curve reads

$$\Delta Q_J - \frac{df}{dh} \Delta h_J = f^* - Q_J^* \quad (3.24)$$

and then the flow depth increment at the outflow boundary can be derived from Eqs. (3.23b) and (3.24)

$$\Delta h_J = \frac{T_J + Q_J^* - f^*}{df/dh - S_J} \quad (3.25)$$

In case of multiple inlets and outlets, Eqs. (3.22), (3.23) or (3.25) should apply to each external boundary node correspondingly.

### 3.5.3 Confluences

A junction of two channels is shown in Fig. 3.2. For convenience, the three cross sections are located very close to each other. At the junction it is assumed that the water surface elevations of all three branches are equal, and the flow discharge of downstream branch is equal to the sum of the discharges of two upstream branches:

$$y_1^{n+1} = y_3^{n+1} \quad (3.26)$$

$$y_2^{n+1} = y_3^{n+1} \quad (3.27)$$

$$Q_3^{n+1} = Q_1^{n+1} + Q_2^{n+1} \quad (3.28)$$

Expanding the variables at time  $t^{n+1}$  yields

$$\Delta h_1 - \Delta h_3 = y_3^* - y_1^* \quad (3.29)$$

$$\Delta h_2 - \Delta h_3 = y_3^* - y_2^* \quad (3.30)$$

$$\Delta Q_3 - \Delta Q_1 - \Delta Q_2 = Q_1^* + Q_2^* - Q_3^* \quad (3.31)$$

From the forward sweeps along branches 1 and 2, one has

$$\Delta Q_1 = S_1 \Delta h_1 + T_1; \quad \Delta Q_2 = S_2 \Delta h_2 + T_2 \quad (3.32)$$

where the coefficients  $S_1$ ,  $T_1$ ,  $S_2$  and  $T_2$  are known.

Substituting the equations in (3.32) into Eq. (3.31), and then using the expressions for  $\Delta h_1$  and  $\Delta h_2$  in Eqs. (3.29) and (3.30), one can obtain

$$\Delta Q_3 = S_3 \Delta h_3 + T_3 \quad (3.33)$$

where

$$S_3 = S_1 + S_2; \quad T_3 = Q_1^* + Q_2^* - Q_3^* + S_1(y_3^* - y_1^*) + S_2(y_3^* - y_2^*) + T_1 + T_2 \quad (3.34)$$

Now, the forward sweep along branch 3 can be continued. In the return sweep the depth increments  $\Delta h_1$  and  $\Delta h_2$  can be determined with Eqs. (3.29) and (3.30) using the  $\Delta h_3$  calculated previously at the end of the return sweep along branch 3 back to the junction. Equations (3.32) then yield the discharge increments  $\Delta Q_1$  and  $\Delta Q_2$ .

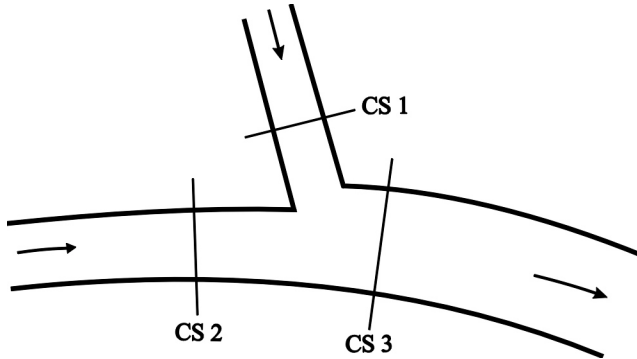


Fig. 3.2 Configuration of Confluence

### 3.5.4 Hydraulic Structures

#### *General Consideration*

Because the flows through the hydraulic structures are very complicated, it is extremely difficult to simulate the detailed flow patterns around the structures using 1-D hydrodynamic model. Simplifications have to be made to solve this problem. By neglecting the storage effect in the hydraulic structure, the same flow discharge is imposed in the upstream and downstream of the structure. The following continuity equation is then derived,

$$Q_{up} = Q_{down} \quad (3.35)$$

where the subscripts “*up*” and “*down*” denote the computational nodes upstream and downstream of the structure. An iteration scheme for Eq. (3.35) can be derived by performing a Taylor series expansion up to the first order as below,

$$\Delta Q_{up} - \Delta Q_{down} = Q_{down}^* - Q_{up}^* \quad (3.36)$$

In order to determine the water elevation in the hydraulic structure, a stage-discharge relation is usually used. For hydraulic structures such as culverts, bridge crossings, drop structures and measuring flumes, the flows are distinguished as inlet control flow (or free overfall flow) and downstream control flow. Inlet control flow is assumed to be critical,

while downstream control flow is treated as an orifice-like flow. For the critical flow in case of inlet control, the stage-discharge relation can be written as

$$Q = f(y_{up}) \quad (3.37)$$

and an iteration scheme similar to Eq. (3.24) can be derived

$$\Delta Q - \frac{\partial f}{\partial y_{up}} \Delta h_{up} = f^* - Q^* \quad (3.38)$$

For the orifice-like flow, the following empirical relation is usually used

$$Q = A \sqrt{\frac{2g(y_{up} - y_{down})}{K_L}} \quad (3.39)$$

where  $K_L$  is the coefficient of energy loss through the hydraulic structure.

Because it can not handle the situation of  $y_{up} \leq y_{down}$ , Eq. (3.39) is reformulated as

$$y_{up} - y_{down} = \frac{K_L}{2g} \frac{Q|Q|}{A^2} \quad (3.39')$$

An iteration scheme for Eq. (3.39') is then obtained as

$$\Delta h_{up} - \Delta h_{down} = -y_{up}^* + y_{down}^* + \frac{K_L}{2g} \frac{Q^*|Q^*|}{A^{*2}} \quad (3.40)$$

Eq. (3.36) can be written as the compact form of Eq. (3.13), with the coefficients being  $a_j = 0$ ,  $b_j = 1$ ,  $c_j = 0$ ,  $d_j = -1$ , and  $p_j = Q_{up}^* - Q_{down}^*$ . Eqs. (3.38) and (3.40) can be written as Eq. (3.16), with the coefficients being  $e_j = -\partial f / \partial y_{up}$ ,  $f_j = 1$ ,  $g_j = 0$ ,  $w_j = 0$ ,  $r_j = f^* - Q^*$ , and  $e_j = 1$ ,  $f_j = 0$ ,  $g_j = -1$ ,  $w_j = 0$ ,  $r_j = -y_{up}^* + y_{down}^* + K_L Q^* |Q^*| / (2g A^{*2})$ , respectively. With being written as the forms of Eqs. (3.13) and (3.16), the equations (3.36), (3.38) and (3.40) can be easily incorporated in the solution algorithm as an intrinsic part.

The implementations of culverts, bridge crossing, drop structures and measuring flumes are introduced in more detail as follows.

### Culverts

Three flow states are distinguished for culverts: inlet control (unsubmerged or submerged), outlet control and normal flow. Inlet control flow occurs when the flow capacity of the culvert entrance is less than the flow capacity of the culvert barrel. Outlet control flow occurs when the culvert capacity is limited by downstream conditions or by the flow capacity of the culvert barrel. The inlet control flow is switched to outlet control flow when the difference in energy head between upstream and downstream ends of the culvert is smaller than a certain limit. Normal flow is adopted when the flow discharge in the culvert is negligible.

Inlet Control Flow. For inlet control conditions, the flow capacity of the culvert is limited by the capacity of the culvert opening, and hence the flow in the culvert entrance can be assumed to be critical. The dynamic equation for the inlet control flow reads

$$Q = A_c \sqrt{g \frac{A_c}{B_c}} \quad (3.41)$$

where  $A_c$  and  $B_c$  are the flow area and the top width of the flow in the culvert opening, respectively, both being functions of the flow depth  $h_c$  in the culvert opening.

To set Eq. (3.41) in the required form (3.37), a relation has to be established between  $h_c$  and  $y_{up}$ . This is done through the nomographs of the Federal Highway Administration (FHWA, 1985), which give the inlet control headwater for a given discharge. The FHWA nomographs are considered to be accurate to within  $\pm 10\%$  in determining the required inlet control headwater.

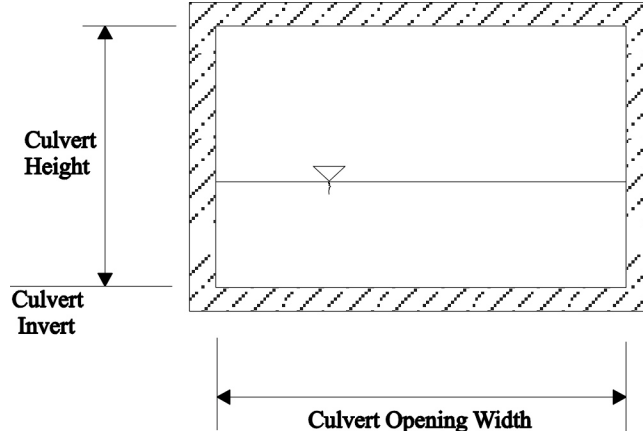


Fig. 3.3 Configuration of Box Culvert

The FHWA nomographs are available for both box (Fig. 3.3) and pipe culverts and both submerged and unsubmerged culvert openings. The headwater upstream of the unsubmerged culvert is

$$H = h_c + v_c + D(C_{cl} \tilde{Q}^{C_{c2}} - C_{c3} S_c) \quad (3.42)$$

and the headwater upstream of the submerged culvert is

$$H = D(C_{c4} \tilde{Q}^2 + C_{c5} - C_{c3} S_c) \quad (3.43)$$

where  $v_c$  is the velocity head in the culvert opening;  $D$  is the height of culvert opening;  $S_c$  is the culvert slope;  $C_{c1,\dots,5}$  are coefficients that are functions of the FHWA chart and scale numbers; and  $\tilde{Q}$  is a dimensionless discharge,  $\tilde{Q} = Q/A_{cvl}\sqrt{D}$ , with  $A_{cvl}$  being the area of culvert opening.

The transition from unsubmerged to submerged inlet control flow occurs for  $\tilde{Q} = 3.5$ .

The derivative  $\partial f/\partial y_{up}$  is then approximated as

$$\frac{\partial f}{\partial y_{up}} = \frac{\partial f}{\partial h_c} \frac{\partial h_c}{\partial y_{up}} \quad (3.44)$$

where  $\partial f/\partial h_c$  is determined with Eq. (3.41), and  $\partial h_c/\partial y_{up}$  is determined with Eqs. (3.42) and (3.43).

Since determining  $\partial f/\partial h_c$  and  $\partial h_c/\partial y_{up}$  is tedious, a more robust method is usually adopted:

$$\frac{\partial f}{\partial y_{up}} = \frac{2\Delta Q}{y_{up}(Q + \Delta Q) - y_{up}(Q - \Delta Q)} \quad (3.45a)$$

or

$$\frac{\partial f}{\partial y_{up}} = \frac{Q(y_{up} + \Delta y_{up}) - Q(y_{up} - \Delta y_{up})}{2\Delta y_{up}} \quad (3.45b)$$

Outlet Control Flow. The outlet control flow is assumed to be an orifice-like flow, which can be described by Eq. (3.39), with  $K_L$  being  $K_L = K_i + K_f + K_p + K_o$ . Here  $K_i$  is the entrance loss coefficient,  $K_f$  is the friction loss coefficient,  $K_p$  is the pier loss coefficient to account for the head loss due to the dividing walls between multiple culverts, and  $K_o$  is the outlet loss coefficient.

Normal Flow. For low flow conditions, in which the flow discharge in the culvert is negligible, the flow through the culvert is assumed to be normal flow. The dynamic equation is

$$Q = f(y_{up}) = \frac{1}{n} A_c R_c^{2/3} S_c^{1/2} \quad (3.46)$$

where  $R_c$  is the hydraulic radius of the culvert. The derivative  $\partial f/\partial y_{up}$  is calculated by Eq. (3.38).

Table 3.1 FHWA Chart and Scale Numbers for Pipe and Box Culverts (1985)

Description	Chart Number	Scale Number
<b>Concrete pipe culvert</b>		
square edged entrance with headwall	1	1
groove end entrance with headwall	1	2
groove end entrance, pipe projecting from fill	1	3
<b>Corrugated metal pipe culvert</b>		
Headwall	2	1
mitered to conform to slope	2	2
pipe projecting from fill	2	3
<b>Concrete pipe culvert, beveled ring entrance</b>		
small bevel	3	1
large bevel	3	2
<b>Box culvert with flared wingwalls</b>		
wingwalls flared 30° to 75°	8	1
wingwalls flared 90° to 15°	8	2
wingwalls not flared	8	3
<b>Box culvert with flared wingwalls and inlet top edge</b>		
wingwalls flared 45°, inlet top edge bevel =0.43D	9	1
wingwalls flared 18° to 33.7°, inlet top edge bevel =0.083D	9	2
<b>Box culvert, 90° headwall, chamfered or beveled inlet edge</b>		
inlet edge chamfered ¾ inch	10	1
inlet edges beveled 1/2 in/ft at 45°	10	2
inlet edges beveled 1 in/ft at 33.7°	10	3
<b>Box culvert, skewed headwall, chamfered or beveled inlet edge</b>		
headwall skewed 45°, inlet edges chamfered 3/4 inch	11	1
headwall skewed 30°, inlet edges chamfered 3/4 inch	11	2
headwall skewed 15°, inlet edges chamfered 3/4 inch	11	3
headwall skewed 15° to 45°, inlet edges beveled	11	4
<b>Box culvert, non-offset flared wingwalls, 3/4 inch chamfer at top of inlet</b>		
wingwalls flared 45°, inlet not skewed	12	1
wingwalls flared 18.4°, inlet not skewed	12	2
wingwalls flared 18.4°, inlet skewed 30°	12	3
<b>Box culvert, offset flared wingwalls, beveled at top of inlet</b>		
wingwalls flared 45°, inlet top edge bevel = 0.042D	13	1
wingwalls flared 33.7°, inlet top edge bevel = 0.083D	13	2
wingwalls flared 18.4°, inlet top edge bevel = 0.083D	13	3

### ***Bridge Crossings***

Two flow states are distinguished for bridge crossings (see Henderson, 1966): Class A flow is the subcritical flow through the bridge opening, whereas Class B or ‘choked’ flow is the critical flow in the bridge opening. The criterion to distinguish Class A and Class B flows is a function of the contraction ratio  $\sigma$ , which is the ratio of the bridge opening area to the total area of the bridge crossing. Henderson (1966) presented two formulations for the limiting value of  $\sigma$ . The first formulation is based on equating the energy heads upstream of the bridge crossing and in the bridge crossing:

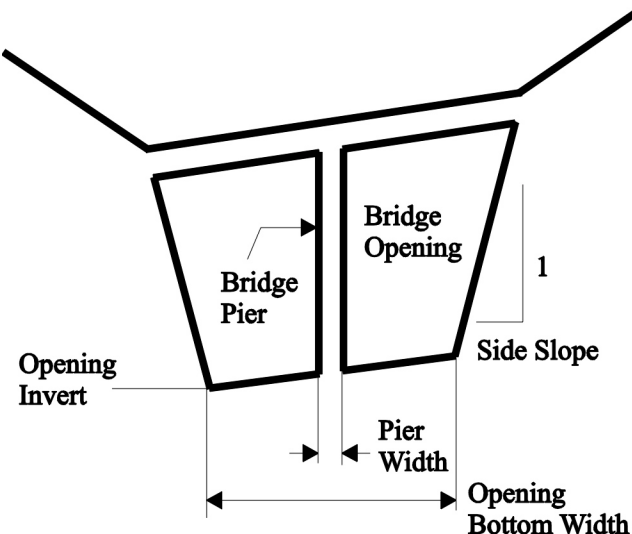


Fig. 3.4 Configuration of Bridge Crossing

$$\sigma^2 = \frac{27Fr_{up}^2}{(2 + Fr_{up}^2)^3} \quad (3.47)$$

where  $Fr$  is the Froude number.

The second formulation is based on equating the momentum functions in the bridge crossing and downstream of the bridge crossing:

$$\sigma = \frac{(2 + 1/\sigma)^3 Fr_{down}^4}{(1 + 2Fr_{down}^2)^3} \quad (3.48)$$

*Class A flow.* From experiments of Yarnell (1934), the following relation between the water elevation change through the bridge and the downstream Froude number can be obtained:

$$\frac{y_{up} - y_{down}}{h_{down}} = KFr_{down}^2 (K + 5Fr_{down}^2 - 0.6)(\alpha + 15\alpha^4) \quad (3.49)$$

where  $K$  is the pier shape coefficient, and  $\alpha = 1 - \sigma$ .

The iteration scheme similar to Eq. (3.40) is obtained as

$$\Delta h_{up} - \Delta h_{down} = -y_{up}^* + y_{down}^* + K(K + 5Fr_{down}^{*2} - 0.6)(\alpha + 15\alpha^4) \frac{Q_{down}^* |Q_{down}^*|}{gA_{down}^{*2}} \quad (3.50)$$

***Class B flow.*** Class B flow is similar to the inlet control culvert flow. Eq. (3.41) is used to describe the critical flow in the culvert, and (3.45) is used to derive the coefficients of the set of algebraic equations. However, Eqs. (3.42) and (3.43) are replaced by

$$H = h_b + v_b + K_E \frac{1}{2g} \left( \frac{Q}{A} \right)_{down}^2 \quad (3.51)$$

where  $K_E$  is an energy loss coefficient depending on the pier shape.

### ***Drop Structures***

Three flow states are distinguished for drop structures: free overfall, downstream control (submerged drop structure), and normal flows. A free overfall occurs when the flow is critical at the brink of the drop structure. The drop structure then acts as a control. If the flow capacity of the drop structure is limited by the downstream flow conditions, the drop structure is considered to be submerged, and the flow discharge depends on both upstream and downstream flow conditions. The free overfall flow is switched to the downstream control flow if the difference in energy head between upstream and downstream ends of the drop structure is smaller than a certain limit.

***Free overfall flow.*** The free overfall flow at the drop structure is assumed to be critical, and hence it is similar to inlet control culvert flow and Class B flow at bridge crossings. Consequently, Eq. (3.41) is used with Eq. (3.51), in which  $K_E$  now denotes the energy loss due to the geometry of drop structure entrance.

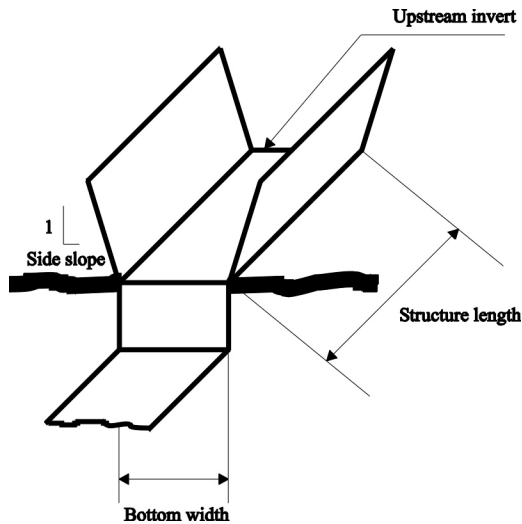


Fig. 3.5 Configuration of Drop Structure

Downstream control flow. For downstream control conditions, the discharge at the drop structure is limited by the downstream conditions, and the flow is assumed to be an orifice-like flow. The dynamic equation is given by Eq. (3.39'). The energy loss coefficient  $K_L$  is determined by  $K_L = K_i + K_f + K_o$ .

Normal flow. When the flow discharge at the drop structure is negligible, the flow at the drop structure is assumed to be normal flow. The dynamic equation is given by Eq. (3.46). The procedure used to derive the coefficients of the discretized equations for normal flow in a culvert is employed here.

### Measuring Flumes

For measuring flumes shown in Fig. 3.6, the calibrated stage-discharge rating curve,  $Q = f(h)$ , is very handy to be imposed. The relation between  $h_f$  and  $y_{up}$  is given by Eq. (3.51) in which  $K_L$  is the energy loss due to the geometry of flume entrance.

When the downstream water elevation rises to a certain level, the measuring flume becomes submerged or is controlled by the downstream flow conditions, and the stage-discharge rating curve may not be valid. Eq. (3.39) is used to describe the flow in this situation. The iteration scheme similar to Eq. (3.40) is then obtained.



Fig. 3.6 Measuring Flume in Goodwin Creek Watershed

### 3.6 Supplemental Treatments for Flow Calculations

#### 3.6.1 Friction Slope Formulation

The friction slope in Eqs. (3.2) and (3.4) can be represented in various ways depending on the reach-averaged representation of  $Q$  and  $K$ . French (1985) listed four methods: conveyance mean, arithmetic mean, geometric mean and harmonic mean, which were used in HEC-2 model (USACE, 1982). Langendoen (1996) studied the performance of these four methods implemented in DWAVENT, and found that the conveyance mean method can provide more accurate solution of hydraulic variables at a channel control and the arithmetic mean method performs best for the case of impoundment. The CCHE1D flow model adopts these two methods to represent the friction slope. The arithmetic mean method has been introduced in Eq. (3.9). The conveyance mean friction slope is given as

$$S_f = \left\{ \frac{\theta[\psi Q_{j+1}^{n+1} + (1-\psi)Q_j^{n+1}] + (1-\theta)[\psi Q_j^n + (1-\psi)Q_{j+1}^n]}{\theta[\psi_R K_{j+1}^{n+1} + (1-\psi_R)K_j^{n+1}] + (1-\theta)[\psi_R K_{j+1}^n + (1-\psi_R)K_j^n]} \right\}^2 \quad (3.52)$$

and its linearized form is

$$\begin{aligned} S_f = & \left[ \frac{\theta \bar{Q}^* + (1-\theta) \bar{Q}^n}{\theta \bar{K}^* + (1-\theta) \bar{K}^n} \right]^2 - 2\theta(1-\psi_R) \frac{\bar{S}_f^*}{\bar{K}^*} \left( \frac{\partial K}{\partial h} \right)_j^* \Delta h_j + 2\theta(1-\psi) \frac{\bar{Q}^*}{\bar{K}^{*2}} \Delta Q_j \\ & - 2\theta\psi_R \frac{\bar{S}_f^*}{\bar{K}^*} \left( \frac{\partial K}{\partial h} \right)_{j+1}^* \Delta h_{j+1} + 2\theta\psi \frac{\bar{Q}^*}{\bar{K}^{*2}} \Delta Q_{j+1} \end{aligned} \quad (3.53)$$

where  $\bar{S}_f = \bar{Q}^2 / \bar{K}^2$ ,  $\bar{Q} = \psi Q_{j+1} + (1-\psi)Q_j$  and  $\bar{K} = \psi_R \bar{Q}_{j+1} + (1-\psi_R) \bar{Q}_j$ .

### 3.6.2 Manning's Roughness Coefficient $n$

Determination of Manning's roughness coefficient  $n$  is very essential to the accuracy of the flow calculation. The value of Manning's  $n$  is highly variable and depends on a number of factors including channel size, shape, irregularity and alignment; channel meandering and curvature; bed form and surface roughnesses; obstructions; sediment transport; vegetation; temperature; and seasonal change. Due to this fact, it is suggested that Manning's  $n$  values should be calibrated if gauged water surface profiles and high water marks are available. If gauged data are not available, the  $n$  values for similar stream conditions should be used as guidance. Several references (Chow, 1959; Fasken, 1963; Barnes, 1967; Hicks and Mason, 1991) can help in the selection of  $n$  values.

### 3.6.3 Momentum Correction Factor $\beta$

Since the CCHE1D model divides the entire cross section of a compound channel into three subsections (left flood plain, main channel and right flood plain), the momentum for entire cross section is set as follows,

$$\beta Q U = \sum_{l=1}^3 Q_l U_l \quad (3.54)$$

where  $U$  and  $Q$  are the velocity and discharge of entire cross section;  $U_l$  and  $Q_l$  are the velocity and discharge of subsection  $l$  ( $l=1,2,3$ ).

Therefore the momentum correction factor  $\beta$  is calculated as

$$\beta = \frac{1}{Q U} \sum_{l=1}^3 Q_l U_l = \frac{A}{K^2} \sum_{l=1}^3 \frac{K_l^2}{A_l} \quad (3.55)$$

where  $K_l$  is the conveyance of subsection  $l$ .

### 3.6.4 Handling of Small Flow Depth

Computational difficulties arise when the flow depth becomes small. This was explained well by Cunge et al (1980). Because the conveyance and flow discharge go to zero as the flow depth goes to zero, the friction slope is indeterminate. Meselhe and Holly (1993) showed that the characteristic curves are vertical and do not intersect when the flow depth is zero. Consequently, a solution does not exist.

The approach proposed by Cunge et al (1980) and developed further by Meselhe and Holly (1993) is selected to handle the dry-bed problem in CCHE1D model. The weighting of the friction slope is switched from central ( $\psi_R = 0.5$ , highest accuracy) to upstream ( $0 \leq \psi_R \leq 0.5$ ). Langendoen (1996) established the empirical function

$$\psi_R = \min(0.5, ah^b) \quad (3.56)$$

where the coefficient  $a \approx 0.7$  and the exponent  $b \approx 0.35$ .

However, Eq. (3.56) is only an empirical function that was calibrated for diffusive wave model in certain cases. In current CCHE1D model, another option  $\psi_R = 0.05$  is also adopted, which is found to be more effective.

### 3.6.5 Simulation of Transcritical Flow

In practice, it may be encountered that supercritical or critical flows exist only in one or two isolated cross-sections of natural rivers. From the scientific point of view, the most appropriate solution for this problem would be establishing a fully dynamic wave model for both supercritical and subcritical flows, but this would need new numerical methods, significantly change the existing program, and tremendously increase computation time. CCHE1D adopts a hybrid dynamic/diffusive wave model, which uses the dynamic wave model when the Froude number is less than 0.9, and uses the diffusive wave model for higher Froude numbers. This hybrid dynamic/diffusive wave model can effectively avoid the numerical instability of the dynamic wave model in the transitional flow region, and is very easily implemented within the existing numerical framework of CCHE1D, such as the Preissmann implicit scheme and the double sweep iteration method. Certainly, the substitution of the dynamic wave model by the diffusive wave model leads to accuracy loss. However, if the flow is approximately uniform, the error due to this substitution in a few isolated locations of a channel network is small and negligible. When the channel geometry changes rapidly, this error can be significant, but if there is no hydraulic jump, this error can be compensated somehow by re-calibrating the Manning's roughness coefficient.

## Chapter 4 1-D Sediment Transport Model

### 4.1 Sediment Transport in Channels

#### 4.1.1 Governing Equations for Sediment Transport

The governing equation for the non-equilibrium transport of nonuniform sediment is

$$\frac{\partial(AC_{tk})}{\partial t} + \frac{\partial Q_{lk}}{\partial x} + \frac{1}{L_s}(Q_{lk} - Q_{t^*k}) = q_{lk} \quad (4.1)$$

where  $C_{tk}$  is the section-averaged sediment concentration of size class  $k$ ;  $Q_{lk}$  is the actual sediment transport rate of size class  $k$ ;  $Q_{t^*k}$  is the sediment transport capacity or the so-called equilibrium transport rate of size class  $k$ ;  $L_s$  is the adaptation length of non-equilibrium sediment transport; and  $q_{lk}$  is the side inflow or outflow sediment discharge from bank boundaries or tributary streams per unit channel length.

Eq. (4.1) is a generalized governing equation that can be applied to bed load, suspended load and wash load separately, or applied to total load, depending on how the sediment transport rate and the adaptation length are defined. Because the CCHE1D model does not distinguish bed load from suspended load but instead treats them together as bed-material load, Eq. (4.1) is applied to bed-material load and wash load. For bed-material load, its transport rate  $Q_{lk}$  is equal to the sum of bed load and suspended load transport rates. For wash load, the adaptation length  $L_s$  is assumed to be infinitely large and then the exchange term in the left-hand side is zero.

The bed-material load transport capacity can be written as a general form

$$Q_{t^*k} = p_{bk}Q_{lk}^* \quad (4.2)$$

where  $p_{bk}$  is the availability factor of sediment, which is defined as the bed-material gradation here;  $Q_{lk}^*$  is the potential bed-material load transport capacity for size class  $k$ , which can be determined with existing formulas.

The bed deformation due to size class  $k$  is determined with

$$(1 - p')\frac{\partial A_{bk}}{\partial t} = \frac{1}{L_s}(Q_{lk} - Q_{t^*k}) \quad (4.3)$$

or with the sediment continuity equation

$$(1 - p')\frac{\partial A_{bk}}{\partial t} + \frac{\partial(AC_{tk})}{\partial t} + \frac{\partial Q_{lk}}{\partial x} = q_{lk} \quad (4.4)$$

where  $p'$  is the porosity of bed material;  $\partial A_{bk}/\partial t$  is the bed deformation rate of size class  $k$ .

The bed material is divided into several layers (Fig. 4.1). The variation of bed-material gradation at the mixing layer (surface layer) is described as (Wu and Li, 1992a and b)

$$\frac{\partial(A_m p_{bk})}{\partial t} = \frac{\partial A_{bk}}{\partial t} + p_{bk}^* \left( \frac{\partial A_m}{\partial t} - \frac{\partial A_b}{\partial t} \right) \quad (4.5)$$

where  $p_{bk}$  is the percentage of the  $k$ th size class of bed material at the mixing layer;  $A_m$  is the area of bed-material mixing layer at a cross section;  $\partial A_b / \partial t$  is the total bed deformation rate, which is expressed as  $\partial A_b / \partial t = \sum_{k=1}^N \partial A_{bk} / \partial t$ ;  $N$  is the total number of size classes;  $p_{bk}^*$  is  $p_{bk}$  when  $\partial A_m / \partial t - \partial A_b / \partial t \leq 0$ , and  $p_{bk}^*$  is the percentage of the  $k$ th size class of bed material in subsurface layer (under the mixing layer) when  $\partial A_m / \partial t - \partial A_b / \partial t > 0$ .

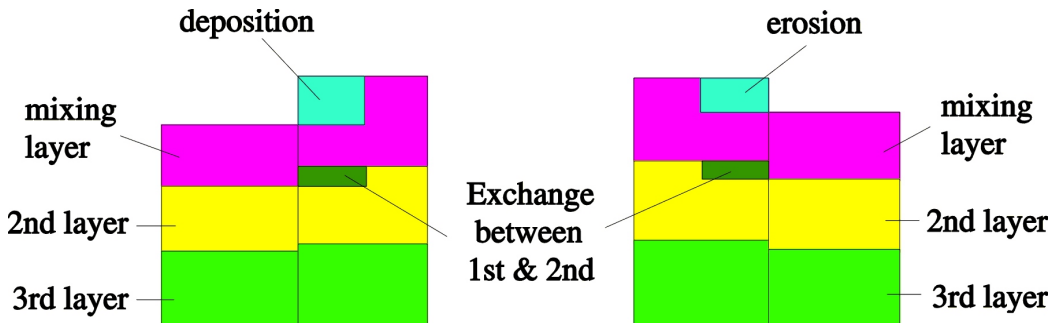


Fig. 4.1 Bed Material Sorting Mode

#### 4.1.2 Discretization of Governing Equations

Substituting  $C_{tk} = Q_{tk} / (A \beta_t U_{tk})$  into Eq. (4.1), one can obtain the following sediment transport equation

$$\frac{\partial}{\partial t} \left( \frac{Q_{tk}}{\beta_t U_{tk}} \right) + \frac{\partial Q_{tk}}{\partial x} + \frac{1}{L_s} (Q_{tk} - Q_{t*k}) = q_{lk} \quad (4.6)$$

where  $U_{tk}$  is the section-averaged velocity of sediment, and it is approximated as the section-averaged flow velocity  $U$  in this study;  $\beta_t$  is the correction coefficient that is approximated as 1.

Discretizing Eq. (4.6) with the Preissmann's scheme yields

$$\begin{aligned}
& \psi \frac{Q_{tk,j+1}^{n+1}/U_{j+1}^{n+1} - Q_{tk,j+1}^n/U_{j+1}^n}{\Delta t} + (1-\psi) \frac{Q_{tk,j}^{n+1}/U_j^{n+1} - Q_{tk,j}^n/U_j^n}{\Delta t} \\
& + \theta \frac{Q_{tk,j+1}^{n+1} - Q_{tk,j}^{n+1}}{\Delta x} + (1-\theta) \frac{Q_{tk,j+1}^n - Q_{tk,j}^n}{\Delta x} \\
& + \theta \left[ \psi \frac{1}{L_{s,j+1}^{n+1}} (Q_{tk,j+1}^{n+1} - Q_{t*k,j+1}^{n+1}) + (1-\psi) \frac{1}{L_{s,j}^{n+1}} (Q_{tk,1}^{n+1} - Q_{t*k,j}^{n+1}) \right] \\
& + (1-\theta) \left[ \psi \frac{1}{L_{s,j+1}^n} (Q_{tk,j+1}^n - Q_{t*k,j+1}^n) + (1-\psi) \frac{1}{L_{s,j}^n} (Q_{tk,1}^n - Q_{t*k,j}^n) \right] \\
& = \theta [\psi q_{lk,j+1}^{n+1} + (1-\psi) q_{lk,j}^{n+1}] + (1-\theta) [\psi q_{lk,j+1}^n + (1-\psi) q_{lk,j}^n]
\end{aligned} \tag{4.7}$$

Equation (4.7) can be written as

$$c_1 Q_{tk,j+1}^{n+1} = c_2 Q_{tk,j}^{n+1} + c_3 Q_{tk,j+1}^n + c_4 Q_{tk,j}^n + c_{0k} \tag{4.8}$$

where

$$c_1 = \frac{\psi}{U_{j+1}^{n+1} \Delta t} + \frac{\theta}{\Delta x} + \frac{\theta \psi}{L_{s,j+1}^{n+1}} \tag{4.9}$$

$$c_2 = -\frac{1-\psi}{U_j^{n+1} \Delta t} + \frac{\theta}{\Delta x} - \frac{\theta(1-\psi)}{L_{s,j}^{n+1}} \tag{4.10}$$

$$c_3 = \frac{\psi}{U_{j+1}^n \Delta t} - \frac{1-\theta}{\Delta x} - \frac{(1-\theta)\psi}{L_{s,j+1}^n} \tag{4.11}$$

$$c_4 = \frac{1-\psi}{U_j^n \Delta t} + \frac{1-\theta}{\Delta x} - \frac{(1-\theta)(1-\psi)}{L_{s,j}^n} \tag{4.12}$$

$$\begin{aligned}
c_{0k} &= \theta \psi \frac{Q_{t*k,j+1}^{n+1}}{L_{s,j+1}^{n+1}} + \theta(1-\psi) \frac{Q_{t*k,j}^{n+1}}{L_{s,j}^{n+1}} + (1-\theta)\psi \frac{Q_{t*k,j+1}^n}{L_{s,j+1}^n} + (1-\theta)(1-\psi) \frac{Q_{t*k,j}^n}{L_{s,j}^n} \\
& + \theta \psi q_{lk,j+1}^{n+1} + \theta(1-\psi) q_{lk,j}^{n+1} + (1-\theta)\psi q_{lk,j+1}^n + (1-\theta)(1-\psi) q_{lk,j}^n
\end{aligned} \tag{4.13}$$

For the convenience of the analysis to be developed in the next section, Eq. (4.7) is also written as

$$Q_{tk,j+1}^{n+1} = e_k Q_{t*k,j+1}^{n+1} + e_{0k} \tag{4.14}$$

where  $e_k = \theta \psi / (c_1 L_{s,j+1}^{n+1})$ ;  $e_{0k} = (c_1 Q_{tk,j}^{n+1} + c_2 Q_{tk,j+1}^n + c_3 Q_{tk,j}^n + c_{0k} - \theta \psi Q_{t*k,j+1}^{n+1} / L_{s,j+1}^{n+1}) / c_1$ .

The bed deformation can be described by Eq. (4.3) or (4.4). When using Eq. (4.4) the sediment continuity can be easily satisfied in the calculation, but Eq. (4.4) is more complex and discretizing it may need a different control volume. Therefore, Eq. (4.3) is used to calculate the bed deformation. In order to satisfy the sediment continuity, the right-hand side

of Eq. (4.3) is discretized with the same scheme as the exchange term in Eq. (4.7), as expressed below:

$$(1-p')\frac{\Delta A_{bk,j+1}}{\Delta t} = \theta \frac{Q_{tk,j+1}^{n+1} - Q_{t^*k,j+1}^{n+1}}{L_{t,j+1}^{n+1}} + (1-\theta) \frac{Q_{tk,j+1}^n - Q_{t^*k,j+1}^n}{L_{t,j+1}^n} \quad (4.15)$$

Eq. (4.15) can be written as

$$\Delta A_{bk,j+1} = f_1 Q_{tk,j+1}^{n+1} - f_2 Q_{t^*k,j+1}^{n+1} + f_{0k} \quad (4.16)$$

$$\text{where } f_1 = f_2 = \frac{\theta \Delta t}{(1-p') L_{s,j+1}^{n+1}}; \quad f_{0k} = \frac{(1-\theta) \Delta t}{(1-p') L_{s,j+1}^n} (Q_{tk,j+1}^n - Q_{t^*k,j+1}^n)$$

Eq. (4.2) is treated with an implicit scheme,

$$Q_{t^*k,j+1} = p_{bk,j+1}^{n+1} Q_{tk,j+1}^* \quad (4.17)$$

The bed material sorting is modeled as illustrated in Fig. 4.1. The equation for bed material sorting in the mixing layer, Eq. (4.5), is discretized as

$$p_{bk,j+1}^{n+1} = \frac{\Delta A_{bk,j+1} + A_{m,j+1}^n p_{bk,j+1}^n + p_{bk,j+1}^{*n} (A_{m,j+1}^{n+1} - A_{m,j+1}^n - \Delta A_{b,j+1})}{A_{m,j+1}^{n+1}} \quad (4.18)$$

where  $\Delta A_{bk,j+1}$  is the bed deformation corresponding to size class  $k$  at the time step  $\Delta t$ ;  $\Delta A_{b,j+1}$  is the total bed deformation, expressed as

$$\Delta A_{b,j+1} = \sum_{k=1}^N \Delta A_{bk,j+1} \quad (4.19)$$

The parameter  $p_{bk,j+1}^{*n}$  is  $p_{bk,j+1}^n$ , the bed material gradation in the mixing layer, if  $\Delta A_{b,j+1} + A_{m,j+1}^n \geq A_{m,j+1}^{n+1}$ ; and  $p_{bk,j+1}^{*n}$  is the bed material gradation of subsurface layer, if  $\Delta A_{b,j+1} + A_{m,j+1}^n < A_{m,j+1}^{n+1}$ .

The bed-material gradation under the mixing layer is calculated according to mass conservation.

#### 4.1.3 Solution of Algebraic Equations

The algebraic equations (4.14) and (4.16)-(4.19) are assembled according to the following sequence,

$$Q_{t^*k,j+1} = p_{bk,j+1}^{n+1} Q_{tk,j+1}^* \quad (4.20)$$

$$Q_{tk,j+1}^{n+1} = e_k Q_{t^*k,j+1}^{n+1} + e_{0k} \quad (4.21)$$

$$\Delta A_{bk,j+1} = f_1 Q_{tk,j+1}^{n+1} - f_2 Q_{t^*k,j+1}^{n+1} + f_{0k} \quad (4.22)$$

$$\Delta A_{b,j+1} = \sum_{k=1}^N \Delta A_{bk,j+1} \quad (4.23)$$

$$p_{bk,j+1}^{n+1} = \frac{\Delta A_{bk,j+1} + A_{m,j+1}^n p_{bk,j+1}^n + p_{bk,j+1}^{*n} (A_{m,j+1}^{n+1} - A_{m,j+1}^n - \Delta A_{b,j+1})}{A_{m,j+1}^{n+1}} \quad (4.24)$$

If  $p_{bk,j+1}^{n+1}$  in Eq. (4.20) is replaced by  $p_{bk,j+1}^n$  to form an explicit expression, Eqs. (4.20)-(4.24) can be solved in a decoupled way with a consequence from Eq. (4.20) to (4.24). The decoupled method is very simple, but numerical oscillation may occur and the calculated bed-material gradation may be negative. Now  $p_{bk,j+1}^{n+1}$  in Eq. (4.20) is an implicit treatment, and a coupled calculation procedure is established by solving the set of algebraic equations (4.20)-(4.24) simultaneously using the direct method proposed by Wu and Li (1992a). This kind of coupled method for nonuniform sediment transport, bed deformation and bed material sorting is more stable and can more easily eliminate numerical oscillation and the occurrence of negative bed-material gradation.

Inserting Eqs. (4.20) and (4.21) into Eq. (4.22), one can obtain

$$\Delta A_{bk,j+1} = (f_1 e_k - f_2) p_{bk,j+1}^{n+1} Q_{tk,j+1}^{*n+1} + (f_1 e_{0k} + f_{0k}) \quad (4.25)$$

and then inserting Eq. (4.24) into Eq. (4.25) yields

$$\begin{aligned} \Delta A_{bk,j+1} &= \Delta A_{b,j+1} \frac{(f_2 - f_1 e_k) Q_{tk,j+1}^{*n+1} p_{bk,j+1}^{*n}}{A_{m,j+1}^{n+1} + (f_2 - f_1 e_k) Q_{tk,j+1}^{*n+1}} + \frac{(f_1 e_{0k} + f_{0k}) A_{m,j+1}^{n+1}}{A_{m,j+1}^{n+1} + (f_2 - f_1 e_k) Q_{tk,j+1}^{*n+1}} \\ &\quad - \frac{(f_2 - f_1 e_k) Q_{tk,j+1}^{*n+1} [p_{bk,j+1}^n A_{m,j+1}^n + p_{bk,j+1}^{*n} (A_{m,j+1}^{n+1} - A_{m,j+1}^n)]}{A_{m,j+1}^{n+1} + (f_2 - f_1 e_k) Q_{tk,j+1}^{*n+1}} \end{aligned} \quad (4.26)$$

Summing the above equation (4.26) over all size classes and using Eq. (4.23), one can obtain the following equation to directly calculate the total bed deformation,

$$\begin{aligned} \Delta A_{b,j+1} &= \left\{ - \sum_{k=1}^N \frac{(f_2 - f_1 e_k) Q_{tk,j+1}^{*n+1} [p_{bk,j+1}^n A_{m,j+1}^n + p_{bk,j+1}^{*n} (A_{m,j+1}^{n+1} - A_{m,j+1}^n) ]}{A_{m,j+1}^{n+1} + (f_2 - f_1 e_k) Q_{tk,j+1}^{*n+1}} + \sum_{k=1}^N \frac{(f_1 e_{0k} + f_{0k}) A_{m,j+1}^{n+1}}{A_{m,j+1}^{n+1} + (f_2 - f_1 e_k) Q_{tk,j+1}^{*n+1}} \right\} \\ &\quad \sqrt{\left[ 1 - \sum_{k=1}^N \frac{(f_2 - f_1 e_k) Q_{tk,j+1}^{*n+1} p_{bk,j+1}^{*n}}{A_{m,j+1}^{n+1} + (f_2 - f_1 e_k) Q_{tk,j+1}^{*n+1}} \right]} \end{aligned} \quad (4.27)$$

After  $\Delta A_{b,j+1}$  is calculated by Eq. (4.27), the fractional bed deformation  $\Delta A_{bk,j+1}$  can be determined by Eq. (4.26),  $p_{bk,j+1}^{n+1}$  by Eq. (4.24),  $Q_{tk,j+1}^{n+1}$  by Eq. (4.20), and then  $Q_{tk,j+1}^{n+1}$  by Eq. (4.21) consequentially. This procedure is a direct method of solution.

#### 4.1.4 Boundary Conditions

For the sediment transport calculation, inflow sediment discharges for all the size classes must be given at upstream inlet nodes and at the nodes having lateral inflow. If the channel

model is used in conjunction with a watershed model, the upland water runoff and sediment loads simulated by the watershed model are transferred as inflow water and sediment discharges at the computational nodes for the channel simulation by the CCHE1D's graphical user interface.

At channel confluences (Fig. 3.2), the sediment discharge at the downstream branch is equal to the sum of the sediment discharges at the two upstream branches.

At hydraulic structures with nonerodible beds, such as culverts, drop structures and measuring flumes, the deposition is assumed to be negligible, and hence the bed is fixed and the sediment discharges in the upstream and downstream of the hydraulic structures are set to be the same. For bridge crossings, the bed may change due to channel contraction and local flow features. Currently, the bed change upstream of bridge crossings is simulated but the local bed change in the bridge crossings is not. Methods to simulate the local bed change due to channel contraction and even local flow features around bridge crossings will be implemented in the future.

#### 4.1.5 Properties of the Numerical Method

##### *Stability of the Preissmann's Scheme for Sediment Transport Equation*

Neglecting the influence of the source term in Eq. (4.8), the error equation of the actual sediment transport rate corresponding to Eq. (4.8) is

$$c_1\delta_{j+1}^{n+1} = c_2\delta_j^{n+1} + c_3\delta_{j+1}^n + c_4\delta_j^n \quad (4.28)$$

where  $\delta_j^n$  is the Fourier component defined as  $\delta_j^n = V^n e^{i\sigma x_j}$ , in which  $V^n$  and  $\sigma$  are the amplitude and wave number of the Fourier component.

From Eq. (4.28), one can obtain

$$c_1 V^{n+1} e^{i\sigma(x_j + \Delta x)} = c_2 V^{n+1} e^{i\sigma x_j} + c_3 V^n e^{i\sigma(x_j + \Delta x)} + c_4 V^n e^{i\sigma x_j} \quad (4.29)$$

and then the growth factor

$$G = \frac{V^{n+1}}{V^n} = \frac{c_3 e^{i\sigma \Delta x} + c_4}{c_1 e^{i\sigma \Delta x} - c_2} \quad (4.30)$$

Eqs. (4.9)-(4.13) show that  $c_1 \geq 0$  and  $c_2 + c_3 + c_4 \leq c_1$ . Following Patankar's (1980) suggestion, the sufficient condition for the numerical stability of scheme (4.8) is that  $c_2$ ,  $c_3$ , and  $c_4 \geq 0$ . Enforcing these constraints for the coefficients  $c_1$ ,  $c_2$ ,  $c_3$  and  $c_4$  leads to

$$|G| = \left| \frac{c_3 e^{i\sigma \Delta x} + c_4}{c_1 e^{i\sigma \Delta x} - c_2} \right| = \left| \frac{c_3 + c_4 e^{-i\sigma \Delta x}}{c_1 - c_2 e^{-i\sigma \Delta x}} \right| \leq \frac{c_3 + c_4}{c_1 - c_2} \leq 1 \quad (4.31)$$

which means that the von Neumann condition is satisfied and the scheme is numerically stable.

For a homogeneous case, in which  $U$  and  $L_s$  are constant in the element ( $j \rightarrow j+1$ ,  $n \rightarrow n+1$ ), the constraints  $c_2$ ,  $c_3$ , and  $c_4 \geq 0$  are:

$$-(1-\psi) + \theta C_r - \theta(1-\psi)D_r \geq 0 \quad (4.32)$$

$$\psi - (1-\theta)C_r - (1-\theta)\psi D_r \geq 0 \quad (4.33)$$

$$(1-\psi) + (1-\theta)C_r - (1-\theta)(1-\psi)D_r \geq 0 \quad (4.34)$$

where  $C_r$  is the Courant number,  $C_r = U\Delta t/\Delta x$ ;  $D_r$  is a scale factor to account for the non-equilibrium transport of sediment,  $D_r = U\Delta t/L_s$ .

The inequality (4.33) implies

$$\theta \geq 1 - \frac{\psi}{C_r + \psi D_r} \quad (4.35)$$

The inequality (4.32) can be re-written as

$$\theta[C_r - (1-\psi)D_r] \geq 1 - \psi \quad (4.36)$$

Since  $0 \leq \theta \leq 1$  and  $0 \leq \psi \leq 1$ , the inequality (4.36) requires  $C_r - (1-\psi)D_r \geq 0$ , which means  $\psi \geq 1 - C_r/D_r$ , and

$$\theta \geq \frac{1-\psi}{C_r - (1-\psi)D_r} \quad (4.37)$$

The inequality (4.34) is equal to  $\theta \leq 1 + \frac{1-\psi}{C_r - (1-\psi)D_r}$ , which is satisfied automatically because  $0 \leq \theta \leq 1$ ,  $0 \leq \psi \leq 1$  and  $C_r - (1-\psi)D_r \geq 0$ .

Summarizing the above analysis, the sufficient condition for the numerical stability of scheme (4.8) is

$$\max \left\{ 1 - \frac{\psi}{C_r + \psi D_r}, \frac{1-\psi}{C_r - (1-\psi)D_r} \right\} \leq \theta \leq 1 \quad (4.38)$$

$$\text{with } \max \left\{ 0, 1 - \frac{C_r}{D_r} \right\} \leq \psi \leq 1.$$

Because  $C_r/D_r = L_s/\Delta x$ , if  $L_s \ll \Delta x$ , then  $\psi$  and  $\theta$  should be given values close to 1.

### ***Stability of the Implicit and Explicit Methods for Bed-Material Gradation***

$p_{bk,j+1}^{n+1}$  in Eq. (4.20) is a completely implicit treatment for bed-material gradation. Its numerical stability is analyzed by comparing with the explicit treatment. For the convenience of this comparative analysis, Eq. (4.20) is replaced by

$$Q_{t^*, j+1}^{n+1} = [\theta_p p_{bk, j+1}^{n+1} + (1-\theta_p) p_{bk, j+1}^n] Q_{tk, j+1}^{*n+1} \quad (4.39)$$

where  $\theta_p$  is the temporal factor for bed-material gradation.  $\theta_p = 1$  for the implicit method, and  $\theta_p = 0$  for the explicit method.

Inserting Eqs. (4.21), (4.22) and (4.39) into Eq. (4.24), one can obtain the equation for bed-material gradation as follows

$$\begin{aligned} p_{bk, j+1}^{n+1} = & \frac{\left(A_{m, j+1}^{n+1} - A_{m, j+1}^n - \Delta A_{b, j+1}\right)p_{bk, j+1}^n}{A_{m, j+1}^{n+1} + (f_2 - f_1 e_k)\theta_p Q_{tk, j+1}^{*n+1}} + \frac{\left[A_{m, j+1}^n - (f_2 - f_1 e_k)(1-\theta_p)Q_{tk, j+1}^{*n+1}\right]p_{bk, j+1}^n}{A_{m, j+1}^{n+1} + (f_2 - f_1 e_k)\theta_p Q_{tk, j+1}^{*n+1}} \\ & + \frac{f_1 e_{0k} + f_{0k}}{A_{m, j+1}^{n+1} + (f_2 - f_1 e_k)\theta_p Q_{tk, j+1}^{*n+1}} \end{aligned} \quad (4.40)$$

If  $\Delta A_{b, j+1} + A_{m, j+1}^n \geq A_{m, j+1}^{n+1}$ , then  $p_{bk, j+1}^{n+1} = p_{bk, j+1}^n$ , and the error equation for bed-material gradation is

$$\delta^{n+1} = \delta^n \frac{A_{m, j+1}^{n+1} - \Delta A_{b, j+1} - (f_2 - f_1 e_k)(1-\theta_p)Q_{tk, j+1}^{*n+1}}{A_{m, j+1}^{n+1} + (f_2 - f_1 e_k)\theta_p Q_{tk, j+1}^{*n+1}} \quad (4.41)$$

where  $\delta$  is the Fourier component.

The numerical stability requires that  $r = |\delta^{n+1}/\delta^n| \leq 1$ , which implies

$$\max \left\{ -\Delta A_{b, j+1}, -\frac{2A_{m, j+1}^{n+1} - \Delta A_{b, j+1}}{2\theta_p - 1} \right\} \leq \frac{\theta(1-e_k)Q_{tk, j+1}^{*n+1}\Delta t}{(1-p')L_{s, j+1}^{n+1}}, \text{ when } \theta_p > 0.5 \quad (4.42)$$

and

$$-\Delta A_{b, j+1} \leq \frac{\theta(1-e_k)Q_{tk, j+1}^{*n+1}\Delta t}{(1-p')L_{s, j+1}^{n+1}} \leq \frac{2A_{m, j+1}^{n+1} - \Delta A_{b, j+1}}{1-2\theta_p}, \text{ when } \theta_p < 0.5 \quad (4.43)$$

If  $\Delta A_{b, j+1} + A_{m, j+1}^n < A_{m, j+1}^{n+1}$ , then  $p_{bk, j+1}^{n+1}$  is the bed-material gradation of subsurface layer. Its influence on the numerical stability of bed-material gradation at the mixing layer is assumed to be negligible. The error equation for the bed-material gradation is

$$\delta^{n+1} = \delta^n \frac{A_{m, j+1}^{n+1} - (f_2 - f_1 e_k)(1-\theta_p)Q_{tk, j+1}^{*n+1}}{A_{m, j+1}^{n+1} + (f_2 - f_1 e_k)\theta_p Q_{tk, j+1}^{*n+1}} \quad (4.44)$$

and then the numerical stability condition is

$$A_{m, j+1}^n - A_{m, j+1}^{n+1} \leq \frac{\theta(1-e_k)Q_{tk, j+1}^{*n+1}\Delta t}{(1-p')L_{s, j+1}^{n+1}}, \text{ when } \theta_p > 0.5 \quad (4.45)$$

and

$$A_{m,j+1}^n - A_{m,j+1}^{n+1} \leq \frac{\theta(1-e_k)Q_{tk,j+1}^{*n+1}\Delta t}{(1-p)L_{s,j+1}^{n+1}} \leq \frac{A_{m,j+1}^n + A_{m,j+1}^{n+1}}{1-2\theta_p}, \text{ when } \theta_p < 0.5 \quad (4.46)$$

Because  $e_k < 1$ , numerical stability conditions (4.42) and (4.45) require that the time step  $\Delta t$  in the implicit method have only a lower bound limit. However numerical stability conditions (4.43) and (4.46) for the explicit method require both lower and upper bound limits. It is obvious that the implicit method is much more stable than the explicit method.

The lower limit for the implicit method can be very easily satisfied. In a practical calculation, the total bed deformation  $\Delta A_b$  is usually limited to the range of the mixing layer, i.e.,  $|\Delta A_b| \leq A_m^{n+1}$  or  $A_m^n$ . In case of deposition ( $\Delta A_b > 0$ ), we usually have that  $\Delta A_b + A_m^n \geq A_m^{n+1}$ , which means the numerical stability is controlled by inequality (4.42). The left-hand side of inequality (4.42) is negative and the right-hand side is positive, hence the numerical stability condition is automatically satisfied. In case of erosion ( $\Delta A_b < 0$ ), we usually have that  $\Delta A_b + A_m^n < A_m^{n+1}$ , so the numerical stability is controlled by inequality (4.45). If we set  $A_m^{n+1} \approx A_m^n$ , inequality (4.45) can also be easily satisfied. Therefore, the implicit method has a large advantage over the explicit method with respect to numerical stability.

### **Requirement of Non-negative Bed-Material Gradation**

During the calculation of bed-material gradation, negative values can occur under certain conditions. This is a non-physical phenomenon, and it should be eliminated.

The condition  $p_{bk,j+1}^{n+1} \geq 0$  for Eq. (4.40) implies that

$$f_1 e_{0k} + f_{0k} + [A_{m,j+1}^n - (f_2 - f_1 e_k)(1-\theta_p)Q_{tk,j+1}^{*n+1}] p_{bk,j+1}^n + (A_{m,j+1}^{n+1} - A_{m,j+1}^n - \Delta A_{b,j+1}) p_{bk,j+1}^{*n} \geq 0 \quad (4.47)$$

and then

$$\Delta A_{b,j+1} \leq A_{m,j+1}^{n+1} + \frac{f_1 e_{0k} + f_{0k} + A_{m,j+1}^n (p_{bk,j+1}^n - p_{bk,j+1}^{*n})}{p_{bk,j+1}^{*n}} - \frac{\theta(1-e_k)(1-\theta_p)Q_{tk,j+1}^{*n+1}\Delta t}{(1-p)L_{s,j+1}^{n+1}} \frac{p_{bk,j+1}^n}{p_{bk,j+1}^{*n}} \quad (4.48)$$

Because the last term in the right-hand side of inequity (4.48) is negative but disappears when  $\theta_p = 1$ , the implicit method can more easily satisfy the requirement of non-negative bed-material gradation than the explicit method. Inequity (4.48) requires that the time step in the explicit method be smaller than that in implicit method.

After considering the numerical stability condition of the Preissmann's scheme for sediment transport equation, constraint (4.48) for the implicit method can be easily satisfied. One of the safest treatments is to impose  $\theta = 1$ ,  $|\Delta A_b| \leq A_m^{n+1}$ , and  $A_m^{n+1} \approx A_m^n$ .

#### 4.1.6 Comments on Sediment Calculation

The coupled calculation procedure for nonuniform sediment transport does not significantly increase the computation time in each time step because of the direct method of Wu and Li (1992a) being used to solve the algebraic equations. Compared to the decoupled procedure, the only increase in computation time is the evaluation of Eq. (4.27), which is used to directly calculate the total bed deformation  $\Delta A_b$ . However, because the coupled procedure is much more stable, a larger time step  $\Delta t$  can be used for sediment calculation, and the overall computation time can be reduced significantly.

The above coupled calculation procedure for nonuniform sediment transport is still decoupled from the flow calculation. The actual time step  $\Delta t$  for both flow and sediment calculations is also influenced by the numerical stability of the flow model and the decoupling procedure. However, coupling flow and sediment calculations would be very time-consuming because of the need for an iterative procedure, which would eliminate the advantages of the adopted direct solution method for nonuniform sediment transport. Up till now, this kind of semi-coupled model, which couples nonuniform sediment transport, bed deformation and bed-material sorting while keeping sediment calculation decoupled from the solution of the flow equations, appears to be the most efficient way in the numerical modeling of nonuniform sediment transport.

### 4.2 Bank Erosion and Mass Failure

Channel bed degradation increases bank heights, and lateral erosion near bank toes makes banks steeper. Both processes cause river banks to become unstable. Once the stability criterion is exceeded, a bank mass failure event occurs, and the bank top retreats. The failed bank material deposits first on the bed near the bank toes and then is eroded away by the flow. These bank erosion and channel widening processes can significantly affect the sediment balance of a channel system, and should be modeled for the proper prediction of sediment yield and channel morphology evolution.

#### 4.2.1 Bank Toe Erosion

Bank toe erosion is modeled using the empirical relationship of Arulanandan et al (1980), which was also used by Darby and Thorne (1996),

$$\frac{dW}{dt} = \frac{r}{\gamma_s} \left( \frac{\tau - \tau_c}{\tau_c} \right) \quad (4.49)$$

where  $dW/dt$  is the lateral erosion rate near the bank toe (m/min);  $\tau$  is the flow shear stress (dynes/cm<sup>2</sup>) applied on the bank toe,  $\tau = \gamma RS$ ;  $\tau_c$  is the critical shear stress (dynes/cm<sup>2</sup>) for

bank toe erosion, which is related to the sodium adsorption ratio, pore fluid salt concentration and dielectric dispersion, etc., but here it is set up as an adjustable variable specified by the user because of its complexity and uncertainty;  $\gamma_s$  is the unit weight of the soil ( $\text{kN/m}^3$ );  $r$  is the initial rate of soil erosion ( $\text{g cm}^{-2}\text{min}^{-1}$ ), and is given by

$$r = 0.0223\tau_c \exp(-0.13\tau_c) \quad (4.50)$$

In the time step  $\Delta t$ , the lateral erosion distance is determined with

$$\Delta W_j = \left[ \theta \left( \frac{dW}{dt} \right)_j^{n+1} + (1-\theta) \left( \frac{dW}{dt} \right)_j^n \right] \Delta t \quad (4.51)$$

and the volume of the eroded material is

$$V_e = \frac{1}{2} \Delta W_j \left( 2 - \frac{\min[h_t, H]}{h_t} \right) \min[h_t, H] \quad (4.52)$$

where  $h_t$  is the flow depth from bank toe to water surface, and  $H$  is the bank height.

The eroded bank material is treated directly as side inflow in the sediment transport equation (4.1).

#### 4.2.2 Bank Mass Failure

Planar failure is assumed as the mode of bank failure, shown in Fig. 4.2. The factor of safety is defined as

$$f_s = \frac{F_r}{F_d} \quad (4.53)$$

where  $F_r$  and  $F_d$  are the resistance and driving forces for bank failure, respectively,

$$F_d = W_t \sin \beta = \frac{\gamma_s}{2} \left( \frac{H^2 - y_d^2}{\tan \beta} - \frac{H'^2}{\tan \alpha} \right) \sin \beta \quad (4.54)$$

$$F_r = \frac{(H - y_d)C}{\sin \beta} + \frac{\gamma_s}{2} \left( \frac{H^2 - y_d^2}{\tan \beta} - \frac{H'^2}{\tan \alpha} \right) \cos \beta \tan \phi \quad (4.55)$$

where  $W_t$  is the weight of failure block;  $C$  is the soil cohesion ( $\text{kPa}$ );  $\phi$  is the soil friction angle (degrees);  $\alpha$  is the angle of bank slope;  $y_d$  is the depth of the tension crack (m); and  $\beta$  is the angle of failure plane, which is determined by

$$\beta = \frac{1}{2} \left\{ \tan^{-1} \left[ \frac{H}{H'} (1 - K^2) \tan \alpha \right] + \phi \right\} \quad (4.56)$$

with  $K$  being the tension crack index, the ratio of observed tension crack depth to bank height.

Usually, the failed material deposits first on the bed near the bank toe and then is disaggregated and eroded away by the flow if the flow is strong enough. For large rivers, the failed material depositing near the bank toe does not strongly disturb the flow, but for small rivers and streams, this influence may disturb the flow calculation. In the current version of the CCHE1D model, the failed bank material is stored in a virtual tank and then released gradually in the subsequent time steps to avoid difficulties in the computations due to substantial changes of the channel geometry.

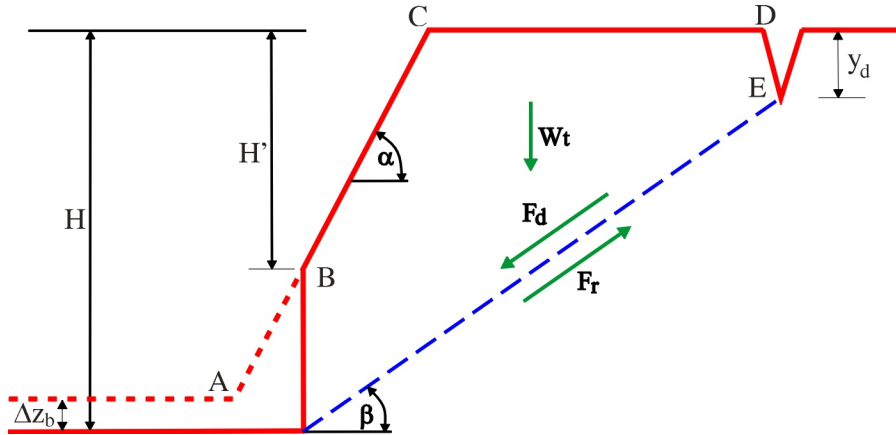


Fig. 4.2 Mode of Bank Mass Failure (after Osman and Thorne, 1988)

### 4.3 Empirical Formulas for Sediment Transport

#### 4.3.1 Sediment Transport Capacity Formulas

Four sediment transport capacity formulas have been implemented in the CCHE1D model: SEDTRA module (Garbrecht et al., 1995), Wu et al's (2000) formula the modified Ackers and White's 1973 formula (Proffitt and Sutherland, 1983), and the modified Engelund and Hansen's 1967 formula (with Wu et al's correction factor, 2000).

##### ***SEDTRA module (Garbrecht, Kuhnle and Alonso, 1995)***

SEDTRA module (Garbrecht et al. 1995) uses three different established transport relations to calculate the transport rate for different size classes. The transport relations are: Laursen's (1958) formula for size classes from 0.010 mm to 0.25mm, Yang's (1973) formula for size classes from 0.25mm to 2.0mm, and Meyer-Peter and Mueller's (1948) formula for size classes from 2.0mm to 50.0mm. Total discharge of sediment is calculated as

$$C_{*t} = \sum_k p_k C_{*k} \quad (4.57)$$

where  $C_{*t}$  is the total sediment capacity in parts per million by weight (ppmw);  $C_{*k}$  is the sediment transport capacity for the  $k$ -th size class in ppmw; and  $p_k$  is the percentage of  $k$ -th size class of sediment, which is set as the bed material gradation usually.

In order to account for the hiding and exposure effects of nonuniform sediment mixtures, the sediment sizes used to calculate the critical flow strength for each size class are adjusted using the following equation (Kuhnle, 1993; Wilcock, 1993; Garbrecht et al., 1995; Kuhnle et al., 1996):

$$d_{ek} = d_k \left( \frac{d_k}{d_m} \right)^{-x} \quad (4.58)$$

where  $d_k$  is the mean size of  $k$ -th size class;  $d_{ek}$  is the sediment size used to calculate the critical flow strength for the  $k$ -th size class;  $d_m$  is the mean diameter of bed material; and  $x$  is an empirical parameter, which is given by  $x=1.7/B$ .  $B$  is a bimodality parameter defined as (Wilcock, 1993)

$$B = \left( \frac{d_c}{d_f} \right)^{1/2} \sum p_m \quad (4.59)$$

where  $d_c$  and  $d_f$  are the diameters of the coarse and fine modes, respectively; and  $p_m$  is the portion of the sediment mixture contained in the coarse and fine modes.

When  $B$  is less than 1.7,  $x=1$ , and for high values of  $B$ ,  $x$  approaches zero. In practice, it is difficult to implement Eq. (4.59). In the current CCHE1D model,  $x$  in Eq. (4.58) is set up as a user-specified parameter, which should be given if the SEDTRA module is chosen to calculate sediment transport capacity. Table 4.1 provides some values of  $x$  recommended by Kuhnle et al (1996).

Table 4.1 Values of  $x$  Recommended by Kuhnle et al. (1996)

Mixture Name	Reference	$d_m$ (mm)	Mixture Type	$B$	$X$
SG10 (laboratory)	Kuhnle (1993a)	0.616	Bimodal	2.49	0.7
SG25 (laboratory)	Kuhnle (1993a)	0.927	Bimodal	2.60	0.7
SG45 (laboratory)	Kuhnle (1993a)	1.454	Bimodal	2.73	0.6
$1/2\psi$ (laboratory)	Wilcock&Southard (1988)	1.82	Unimodal	0.67	1.0
$\psi$ (laboratory)	Wilcock&Southard (1988)	1.85	Unimodal	0.37	1.0
Goodwin Creek (field)	Kuhnle (1993b)	1.189	Bimodal	3.10	0.5

Note: The mixture names for the laboratory data (Kuhnle, 1993a) refer to the percentage of gravel in the bed material: SG10 - 10% gravel, 90% sand; SG25 - 25% gravel, 75% sand; SG45 - 45% gravel, 55% sand; The mixture names of Wilcock and Southard (1988) refer to the standard deviation of the bed material.

### **Wu, Wang and Jia's (2000) Formula**

The formulas for determining fractional bed-load and suspended-load transport capacities proposed by Wu et al.(2000) are

$$\frac{q_{bk}}{p_{bk} \sqrt{(\gamma_s / \gamma - 1) g d_k^3}} = 0.0053 \left[ \left( \frac{n'}{n} \right)^{3/2} \frac{\tau_b}{\tau_{ck}} - 1 \right]^{2.2} \quad (4.60)$$

$$\frac{q_{sk}}{p_{bk} \sqrt{(\gamma_s / \gamma - 1) g d_k^3}} = 0.0000262 \left[ \left( \frac{\tau}{\tau_{ck}} - 1 \right) \frac{U}{\omega_{sk}} \right]^{1.74} \quad (4.61)$$

where  $q_{bk}$  and  $q_{sk}$  are the transport capacities of the  $k$ th size class of bed load and suspended load per unit channel width ( $\text{m}^2/\text{s}$ );  $p_{bk}$  is the percentage of the  $k$ th size class of bed material;  $n$  is the Manning's roughness coefficient for the bed, and  $n'$  is the Manning's coefficient due to the grain roughness of the bed, as given with  $n' = d_{50}^{1/6}/20$ ;  $\tau$  is the total shear stress on the channel (including bed and banks),  $\tau = \gamma R S$ , and  $\tau_b$  is the shear stress on the bed,  $\tau_b = \gamma R_b S$ ;  $R$  is the hydraulic radius of channel, and  $R_b$  is the hydraulic radius for the channel bed determined as  $R_b = (n U)^{3/2} / S^{3/4}$ ;  $S$  is the energy slope;  $U$  is the average flow velocity;  $\omega_{si}$  is the settling velocity of the  $k$ th size class of sediment, which is calculated with the Zhang's formula, Eq. (4.77).

$\tau_{ck}$  is the critical shear stress for the incipient motion of the  $k$ th size class of bed material. The critical shear stress of nonuniform sediment is different from that of uniform sediment. After considering the hiding and exposure mechanism of nonuniform bed material,  $\tau_{ck}$  is given with

$$\tau_{ck} = 0.03 \left( \frac{p_{hk}}{p_{ek}} \right)^{0.6} (\gamma_s - \gamma) d_k \quad (4.62)$$

where  $p_{hk}$  and  $p_{ek}$  are the hiding and exposure possibilities for the  $k$ -th size class of bed material, defined as  $p_{hk} = \sum_{j=1}^N p_{bj} d_j / (d_k + d_j)$  and  $p_{ek} = \sum_{j=1}^N p_{bj} d_k / (d_k + d_j)$ .

Eq. (4.60) was verified using four sets of laboratory data for nonuniform bed load measured by Samaga et al. (1986a), Liu (1986), Kuhnle (1993) and Wilcock and McArdell (1993), as well as field data from five natural rivers (see Williams and Rosgen, 1989). Because the field measurement of bed load is hard to accomplish and may present substantial errors and inaccuracies, data used in verification tests must be carefully selected. First, the flow and sediment parameters must be measured at the same time. These parameters should include flow discharge, velocity, depth, surface slope, bed-load transport rate, bed-load gradation and bed-material gradation. Secondly, because bed load may move as strips and at stages, most of the selected bed load data sets are those averaged from at

least 16 samples across the same cross-section and during a long enough measurement period. Thirdly, bed-material gradation data are also averaged from several simultaneous measurement points along the same cross-section to enhance reliability. These data sets cover a wide range of flow and sediment conditions, as shown in Table 4.2. The relationship of Eq. (4.60) is graphically presented in Fig. 4.3.

Eq. (4.61) was verified using the laboratory data of nonuniform suspended load measured by Samaga et al. (1986b) and two sets of field data from the Yampa River and the Yellow River. The flow and sediment parameters of these data are listed in Table 4.3. The relationship of Eq. (4.61) is graphically shown in Fig. 4.4.

It should be noted that Wu et al's (2000) sediment transport capacity formula (4.60) requires the differentiation of Manning's  $n$  between channel bed and channel banks. Several tests and applications showed that a more realistic representation of Manning's  $n$  over the cross section could provide better results.

Table 4.2 Parameters of Bed-Load Data Used by Wu et al. (2000)

Data Source	$Q$ ( $\text{m}^3/\text{s}$ )	$U$ ( $\text{m/s}$ )	$H$ ( $\text{m}$ )	$S$ ( $10^{-3}$ )	$D_i$ ( $\text{mm}$ )	$q_b$ ( $10^{-3}\text{m}^2/\text{s}$ )
Samaga (1986a)	0.006-0.015	0.49-0.78	0.06-0.11	4.49-6.93	0.073-2.366	0.04-0.22
Kuhnle (1993)	0.01-0.03	0.28-0.81	0.101-0.107	0.47-2.22	0.2-10	1.5E-6-0.064
Wilcock (1993)	0.017-0.057	0.26-1.08	0.088-0.12	0.59-16.2	0.21-64	8.7E-7-0.22
Liu (1986)	0.0035-0.023	0.14-0.67	0.03-0.083	1.5-4	0.31-30	4.9E-5-6.4E-4
Susitna River	799-2800	1.8-2.1	2.4-4.4	1.4-2.4	0.062-128	0.028-0.11
Chulitna River	261-348	1.5-1.8	1.7-1.9	0.64-0.74	0.062-128	0.11-0.23
Black River	20-256	0.44-1.0	0.55-1.9	0.11-0.29	0.062-16	0.0048-0.016
Toutle River	9.3-248	1.3-2.8	0.39-1.5	1.9-5.5	0.062-32	0.11-0.95
Yampa River	26.3-447	0.59-1.3	0.65-3.9	0.40-0.87	0.062-32	0.003-0.054

Table 4.3 Parameters of Suspended-Load Data Used by Wu et al. (2000)

Data Source	Discharge ( $\text{m}^3/\text{s}$ )	Velocity ( $\text{m/s}$ )	Depth ( $\text{m}$ )	En. Slope ( $10^{-3}$ )	$d_i$ ( $\text{mm}$ )	Concent. ( $\text{kg/m}^3$ )
Samaga(1986b)	0.006-0.015	0.49-0.78	0.06-0.11	4.49-6.93	0.073-2.366	0.14-2.62
Yampa River	26.3-447	0.59-1.3	0.65-3.9	0.40-0.87	0.062-1	0.58-2.9
Yellow River	578-5340	0.58-2.38	0.72-4.02	0.18-0.30	0.01-1	7.35-102

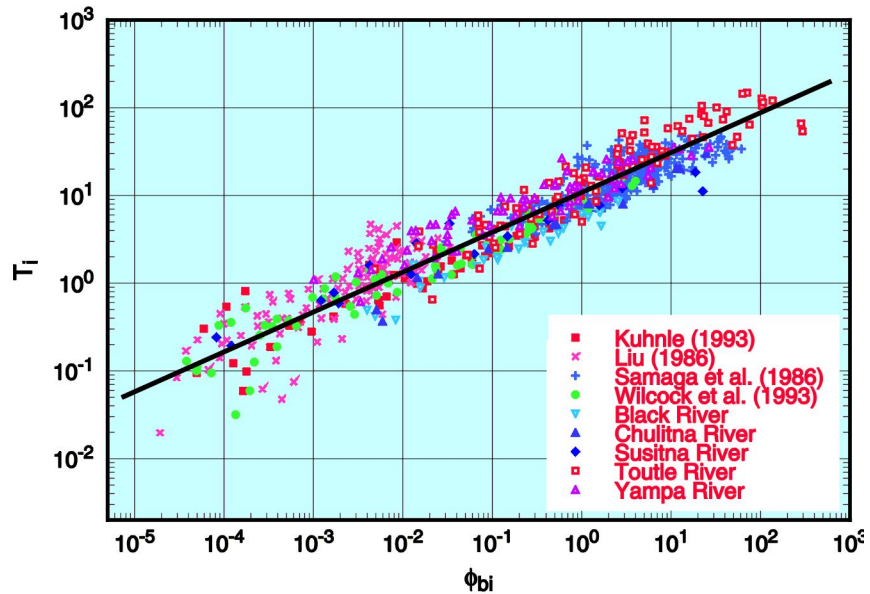


Fig. 4.3 Relation of Fractional Bed-Load Discharge (Wu et al., 2000)

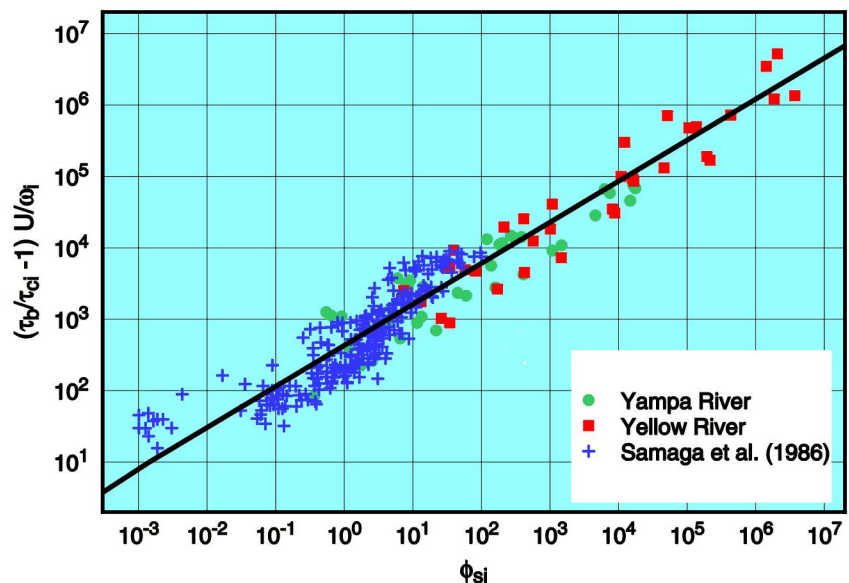


Fig. 4.4 Relation of Fractional Suspended-Load Discharge (Wu et al., 2000)

### **Modified Ackers and White's Formula (Proffitt and Sutherland, 1983)**

Based on Bagnold's stream power concept, Ackers and White (1973) proposed a formula for the total transport capacity of uniform or nonuniform bed-material load. Proffitt and Sutherland (1983) modified it to calculate the fractional transport capacity for each size class of nonuniform bed-material load,

$$G_{gr,k} = C \left( \frac{F_{gr,k}}{A} - 1 \right)^m \quad (4.63)$$

with

$$F_{gr,k} = \varepsilon_k \frac{U_*^n}{[(\gamma_s/\gamma - 1)gd_k]^{1/2}} \left[ \frac{V}{\sqrt{32} \log(10h/d_k)} \right]^{1-n}$$

$$G_{gr,k} = \frac{C_k h}{p_{bk} d_k \gamma_s / \gamma} \left( \frac{U_*}{V} \right)^n$$

Here  $U_*$  is the shear stress  $U_* = \sqrt{ghS}$ .  $A$ ,  $C$ ,  $m$  and  $n$  are coefficients. Because the original Ackers and White's (1973) formula overpredicts the transport rates for fine sediment (smaller than 0.2mm) and for relatively coarse sediments, HR Wallingford (1990) revised these coefficients to correct this tendency. Both versions of these coefficients are listed in Table 4.4.

Table 4.4 Coefficients of Ackers and White Formula (1973, 1990)

	1973 version	1990 version
$d_{gr} \geq 60$	$n = 0.0$ $A = 0.17$ $m = 1.50$ $C = 0.025$	$n = 0.0$ $A = 0.17$ $m = 1.78$ $C = 0.025$
$1 < d_{gr} < 60$	$n = 1.00 - 0.56 \log d_{gr}$ $A = 0.23d_{gr}^{-1/2} + 0.14$ $m = 9.66d_{gr}^{-1} + 1.34$ $\log C = -3.53 + 2.86 \log d_{gr} - (\log d_{gr})^2$	$n = 1.00 - 0.56 \log d_{gr}$ $A = 0.23d_{gr}^{-1/2} + 0.14$ $m = 6.83d_{gr}^{-1} + 1.67$ $\log C = -3.46 + 2.79 \log d_{gr} - 0.98(\log d_{gr})^2$

$\varepsilon_k$  is the correction factor, as verified as

$$\varepsilon_k = \begin{cases} 1.30, & d_k/d_u > 3.7 \\ 0.53 \log(d_k/d_u) + 1.0, & 0.075 < d_k/d_u \leq 3.7 \\ 0.40, & d_k/d_u \leq 0.075 \end{cases} \quad (4.64)$$

where  $d_k$  is the mean diameter of the  $k$ th size class;  $d_u$  is the reference diameter.

According to Proffit and Sutherland's test, their method can provide reasonable prediction for experimental cases but it is less accurate for field data.

### ***Modified Engelund and Hansen's 1967 Formula (with Wu et al's correction factor, 2000)***

Engelund and Hansen (1967) used Bagnold's stream power concept and the similarity principle to obtain their sediment transport formula. For implementation within CCHE1D, the original formula is modified to calculate the fractional transport capacity for nonuniform bed-material load. The modified formula is

$$f'\phi_k = 0.1(\varepsilon_k \tau_{*k})^{5/2} \quad (4.65)$$

where  $f'$  is the friction factor,  $f' = 2gRS/U^2$ ;  $\phi_k$  is the dimensionless sediment transport rate,  $\phi_k = q_{t*k}/[p_{bk}\sqrt{(\gamma_s/\gamma-1)gd_k^3}]$ ;  $q_{t*k}$  is the bed-material load transport rate in  $\text{m}^2/\text{s}$ ;  $\tau_{*k}$  is the dimensionless bed shear stress,  $\tau_{*k} = \tau_0/[(\gamma_s - \gamma)d_k]$ ;  $d_k$  is the diameter of  $k$ -th size class of bed material;  $U$  is the average flow velocity;  $R$  is the hydraulic radius of channel;  $S$  is the energy slope;  $\varepsilon_k$  is a correction factor to take into account the hiding and exposure mechanism of nonuniform sediment transport, which is determined with Wu et al.'s (2000) method

$$\varepsilon_k = \left( \frac{P_{ek}}{P_{hk}} \right)^m \quad (4.66)$$

where  $p_{hk}$  and  $p_{ek}$  are the hiding and exposure possibilities for the  $k$ -th size class of bed material, defined as  $p_{hk} = \sum_{j=1}^N p_{bj} d_j / (d_k + d_j)$  and  $p_{ek} = \sum_{j=1}^N p_{bj} d_k / (d_k + d_j)$ ;  $m$  is a power index, which is given a value of 0.45.

### **4.3.2 Bed-Material Porosity**

#### ***Komura and Simmons' (1967) Method***

Komura and Simmons (1967) proposed an empirical formula for bed-material porosity,

$$p' = 0.245 + \frac{0.0864}{(0.1d_{50})^{0.21}} \quad (4.67)$$

where  $d_{50}$  is the median diameter of bed material, in millimeters (mm).

#### ***Han et al's (1981) Method***

Han et al. (1981) proposed a semi-empirical formula to calculate the initial porosity of uniform bed material,

$$p' = \begin{cases} 1 - 0.525 \left( \frac{d}{d + 4\delta_1} \right)^3 & d < 1\text{mm} \\ 0.3 + 0.175e^{-0.095(d-d_0)/d_0} & d \geq 1\text{mm} \end{cases} \quad (4.68)$$

where  $d$  is the size of bed material, in millimeters (mm);  $d_0$  is a reference size (set as 1mm);  $\delta_1$  is the thickness of the water layer attaching to sediment particles, for which a value of 0.0004mm is assumed.

In the situation of nonuniform bed material, Han et al. studied the probable filling of vacancy among coarse particles by fine particles, and established semi-empirical formulas for the porosity of nonuniform bed material. However, these formulas are very complicated and very difficult to be implemented. If the overall size range of bed material is narrow, or if the fine particles are finer than 0.05mm, then the filling phenomenon is negligible, and the overall porosity of nonuniform bed material can be calculated with B. R. Colby's (1963) method,

$$\frac{1}{1-p'} = \sum_{k=1}^N \frac{p_{bk}}{1-p'_k} \quad (4.69)$$

where  $p_{bk}$  is the percentage of the  $k$ th size class of bed material;  $p'_k$  is the porosity of size class  $k$ , which is calculated with Eq. (4.68) by substituting  $d$  with  $d_k$ .

### 4.3.3 Non-equilibrium Adaptation Length $L_s$

The non-equilibrium adaptation length  $L_s$  characterizes the distance for sediment to adjust from a non-equilibrium state to an equilibrium state. It is a very important parameter in the present model. Unfortunately, it has to be prescribed empirically, and considerable uncertainty exists about its prescription, as rather different values have been adopted by different researchers. Bell and Sutherland (1981) found that  $L_s$  equals to time  $t$  (which is in hours) in an experimental case of bed degradation downstream of a dam due to clear water. Wang (1999) performed the same kind of experiments in a flume 10m long and found that  $L_s$  has average values of 2m-10m. In numerical modeling, Phillips and Sutherland (1989), Tran Thuc (1991) and Wu, Rodi and Wenka (2000) adopted  $L_s$  as the average saltation step length of sand on the bed, which is around  $100d_{50}$  or less, while Rahuel et al. (1989) gave  $L_s$  much larger values such as two times the numerical grid length. The reason may be that  $L_s$  is closely related to the dimensions of the studied sediment movements, bed forms and channel geometries, which are usually markedly different. In laboratory experiments the sediment transport processes are mainly on small scales such as sand saltation, ripples and dunes, while natural sediment transport processes occur usually at larger scales in longer periods. On the other hand,  $L_s$  is also an important parameter for numerical stability, as

shown in Section 4.1.5 and also in Wu, Rodi and Wenka (2000). Small  $L_s$  values require small grid sizes and time steps. In order to save computation time, large mesh sizes and time steps are necessary for the calculation in natural situations. Therefore, it is understandable that different values of  $L_s$  have been adopted in the literature. In the CCHE1D model, different values of  $L_s$  are given for bed load, suspended load and wash load.

### **For bed load**

As mentioned above, the non-equilibrium adaptation length, especially for bed load, is related to the dimensions of sediment movements, bed forms and channel geometries. It is desirable that  $L_s$  take the value relating to the dominant bed form or channel geometry. For example, if there are only sand ripples on the bed, which usually occur in experimental cases, the non-equilibrium adaptation length for bed load may take the average saltation step length of sand, or the length of sand ripples, as it was adopted by Phillips and Sutherland (1989), Tran Thuc (1991) and Wu, Rodi and Wenka (2000). If sand dunes are the dominant bed form,  $L_s$  may take the length of sand dune, which is about 7.3 times the flow depth (van Rijn, 1984),

$$L_{s,b} = 7.3c_l \bar{h} \quad (4.70)$$

where  $L_{s,b}$  is the  $L_s$  for bed load;  $c_l$  is an empirical coefficient, and is set to 1;  $\bar{h}$  is the average flow depth in a channel. Because the flow depths in channels of different order may be significantly different,  $\bar{h}$  takes the average over one channel (link) only.

If alternate bars are the dominant bed form,  $L_{s,b}$  may take the length of alternate bars, which is about 6.3 times the channel width (Yalin, 1972),

$$L_{s,b} = 6.3c_l \bar{B} \quad (4.71)$$

where  $\bar{B}$  is the average width of a channel (link). The coefficient  $c_l$  is set to 1.

The length of sand ripples is very small and therefore it is not recommended as a choice for  $L_s$  in the CCHE1D model, which is designed for the long-term simulation of flow and sediment transport in channel networks. Eqs. (4.70), (4.71), and Rahuel et al's (1989) treatment,  $L_s = 2\Delta x$ , have been implemented to the code. Here,  $\Delta x$  is the computational grid length. In addition, for the convenience of users, an option to give a constant  $L_s$  is also available in the interface. In order to make the right choice, the user should make a judgment of what kind of bed forms or channel geometries are dominant in the case under study. Usually, Eq. (4.70) is more suitable for experimental cases, while Eq. (4.71) is more adequate for natural rivers. Rahuel et al's treatment may provide grid-dependent results.

### **For suspended load**

The non-equilibrium adaptation length for suspended load is given with

$$L_{s,s} = \frac{uh}{\alpha \omega_{sk}} \quad (4.72)$$

where  $L_{s,s}$  is the  $L_s$  for suspended load;  $\alpha$  is the non-equilibrium adaptation coefficient, which can be calculated with Armanini and de Silvio's (1988) method,

$$\frac{1}{\alpha} = \frac{a}{h} + \left(1 - \frac{a}{h}\right) \exp\left[-1.5\left(\frac{a}{h}\right)^{-1/6} \frac{\omega_{sk}}{u_*}\right] \quad (4.73)$$

where  $a$  is the thickness of bottom layer, calculated by their method;  $h$  is flow depth; and  $u_*$  is bed shear velocity.

Values of  $\alpha$  calculated by Eq. (4.73) are usually larger than 1. However, in practice,  $\alpha$  has been given dramatically different values, mostly less than 1, by many researchers. Han et al. (1980) and Wu and Li (1992a, 1992b) suggested  $\alpha=1$  for the case of strong scour,  $\alpha=0.25$  for strong deposition, and  $\alpha=0.5$  for weak scour and deposition. These values have been confirmed by calculations of sedimentation in many reservoirs and rivers. However,  $\alpha$  was given very small values such as 0.001 in the Yellow River (Wei, 1999) and the Rio Grande River (Yang et al., 1998), in which sediment concentration is higher, and rapid erosion and deposition occur often. Therefore,  $\alpha$  is a user-specified parameter in the CCHE1D model. Fortunately, the sensitivity studies reported in Chapters 7 and 8 show that the calculation results of the CCHE1D model are not very sensitive to the adaptation length  $L_s$  and the adaptation coefficient  $\alpha$  in most cases.

Because bed load and suspended load are combined together as bed-material load as described in Eq. (4.1), the non-equilibrium adaptation length for bed-material load in Eq. (4.1) is given as the maximum of  $L_{s,s}$  and  $L_{s,b}$ .

### **For wash load**

Because the net exchange between wash load and channel bed is usually negligible, the non-equilibrium adaptation length for wash load,  $L_{s,w}$ , is set as infinitely large, i.e.,

$$\frac{1}{L_{s,w}} = 0 \quad (4.74)$$

### **4.3.4 Division between Wash Load and Bed-Material Load**

The size range of wash load is determined by  $\omega_{sk}/\kappa u_* \leq 0.06$ . However, for convenience, it can be specified by the user and such an option is provided in the interface.

### 4.3.5 Mixing Layer Thickness

The mixing layer thickness is related to sand dune height as

$$\delta_m = \max[0.5\Delta, 2d_{50}] \quad (4.75)$$

where  $\Delta$  is the sand dune height calculated with van Rijn's (1984) method:

$$\frac{\Delta}{h} = 0.11 \left( \frac{d_{50}}{h} \right)^{0.3} \left( 1 - e^{-0.5T} \right) (25 - T) \quad (4.76)$$

where  $h$  is the flow depth;  $T$  is the non-dimensional excess bed shear stress,  $T = (U^*)^2 / (U_{*cr})^2 - 1$ ;  $U^*$  is the effective bed shear velocity relating to grain roughness,  $U^* = Ug^{0.5} / [18 \log(4h/d_{90})]$ ;  $U_{*cr}$  is the critical bed shear velocity for sediment motion given by Shields diagram;  $d_{50}$  and  $d_{90}$  are particle diameters of bed material.

The mixing layer thickness is given a small lower limiting value, which can be specified by the user, and is set to a default value of 0.05m for natural rivers.

### 4.3.6 Settling Velocity of Sediment Particles

The settling velocity of sediment particles is calculated in different ways, depending on the sediment transport formula used. When Wu et al's sediment transport capacity formula is used, Zhang's formula (see Zhang et al., 1989) is employed to calculate the settling velocity:

$$\omega_s = \sqrt{\left( 13.95 \frac{\nu}{d} \right)^2 + 1.09 \left( \frac{\rho_s}{\rho} - 1 \right) gd} - 13.95 \frac{\nu}{d} \quad (4.77)$$

where  $\omega_s$  is the settling velocity of sediment particles, in m/s;  $d$  is the particle diameter, in m;  $\gamma_s$  and  $\gamma$  are the unit weights of sediment and water;  $\nu$  is the kinematic viscosity of water, which is calculated with  $\nu = 1.792 \times 10^{-6} / (1.0 + 0.03368T + 0.000221T^2)$ , with temperature  $T$  in Celsius degrees and  $\nu$  in  $m^2/s$ . Zhang's formula was calibrated with the measurement data in the range of  $d=0.01mm \sim 10mm$ , but it can be used beyond this range.

When the other sediment transport formulas are used, the settling velocity is determined according to the recommendation of the U.S. Interagency Committee on Water Resources Subcommittee on Sedimentation (1957). The CCHE1D model uses a value for the Corey shape factor of  $SF=0.7$ , where  $SF = c / \sqrt{ab}$ , with  $a$ ,  $b$  and  $c$  being lengths of the longest, the intermediate and the shortest mutually perpendicular axes of the particle, respectively.

## 4.4 Summary of the Options for Sediment Calculation

As introduced in Section 4.3, each of the sediment-related parameters such as sediment transport capacity, bed-material porosity, non-equilibrium adaptation length and mixing layer thickness can be determined by several empirical formulas in the CCHE1D model. The purpose of implementing these multiple options is to broaden the applicability of CCHE1D. Users experienced with this model can choose appropriate formulas for each particular case. Beginners may encounter difficulties in making appropriate choices, but they can start with the default values, which were tested successfully in many cases.

### ***Bank Erosion Model:***

- (1). Enable bank erosion modeling
- (2). Disable bank erosion modeling

### ***Sediment Transport Capacity:***

- (1). SEDTRA module (Garbrecht et al., 1995)
 

If selected, a value for the power index  $x$  must be given.
- (2). Wu et al's (2000) sediment transport capacity formula (***default choice***)
- (3). Modified Ackers and White's 1973 formula (Proffitt and Sutherland, 1983)
- (4). Modified Engelund and Hansen's 1967 formula (with Wu et al's correction factor)

***Recommendation:*** According to model tests and applications, Wu et al's formula can provide reliable results in many cases. The modified Ackers and White's formula may not be applicable to fine sediment transport. The SEDTRA module does not work well when the sediment is close to incipient motion. However, it is a good idea to use sufficient measurement data to test all the four formulas and select the most appropriate formula for the specific case under study.

### ***Bed-Material Porosity:***

- (1). Komura and Simmons' formula (1967) (***default choice***)
- (2). Han et al's formula (1981)
- (3). User specification

### ***Non-equilibrium Adaptation Length:***

- (1). For bed load,
  - (a). Sand dune length
  - (b). Alternate bar length (***default choice***)
  - (c). Twice the grid length
  - (d). User specification

(2). For suspended load,  $\alpha$  in Eq. (4.72) can be determined with

- (a). Armanini and de Silvio's formula (1988)
- (b). User specification (**default value is 0.5**)

(3). For wash load,

- (a).  $1/L_{s,w} = 0$  (**default choice**)
- (b). User specification

*Recommendation:* The evaluation of non-equilibrium adaptation length is very important, but unfortunately it has to be determined on the basis of case by case. Besides the above default choices, the user can refer the values used in the model tests and applications in Chapters 7 and 8.

#### ***Wash-Load Size Range:***

- (1).  $\omega_{sk}/\kappa u_* \leq 0.06$  (**default choice**)
- (2). User specification

*Recommendation:* The wash load size range is dependent on the flow and sediment conditions of the case under study. Usually, for sediment transport in natural rivers, option (1) is applicable; for the sedimentation in reservoirs, the number of wash load size range is suggested to be set as 0, which means no wash load is excluded from the simulation of total load.

#### ***Mixing Layer Thickness:***

- (1). Half the sand dune height, by Eq. (4.75) (**default choice**)
- (2). Twice the median size of bed material
- (3). Related to flow depth,  $0.05h$
- (4). User specification

*Recommendation:* The mixing layer thickness is a very important parameter for the calculation of bed material sorting, which in turn influences the whole calculation. The option (1) is suggested as default choice. However, in case of bed armoring, a value of one or two times of bed material size  $d_{50}$  is suggested.

## Chapter 5 Landscape Analysis and Watershed Modeling

### 5.1 Landscape Analysis

The software TOPAZ (TOpographic PArameteriZation, Garbrecht and Martz, 1995) is a digital landscape analysis tool that provides comprehensive processing of raster Digital Elevation Models (DEMs) to segment watersheds, define drainage divides, identify drainage networks, and parameterize subcatchments automatically. It adopts the D8 (Deterministic Eight-neighbor) method to define landscape properties for each individual raster cell. The relative slope to each adjacent raster cell is calculated, and the flow is assigned toward the direction of the steepest slope. Once flow directions are established, upslope drainage areas are determined for each cell. Channels are then defined as those cells with upstream drainage area greater than a user-defined critical source area (CSA) value. This critical source area represents the drainage area necessary to produce enough runoff to form a permanent channel. By using a specified CSA to define the beginning of channels, it is possible that a few very short exterior (source) links are generated. TOPAZ provides an option to remove these spurious channels by allowing the user to define a minimum source channel length (MSCL). Once the channels are defined, the user must provide the location of the watershed outlet. TOPAZ then defines the watershed boundary, and the subcatchments draining into source nodes and into the left and right banks of each channel link. Once the channel network has been defined, it is further processed to determine the Strahler order of each channel link and to assign an identification number to each network node and channel link. The subcatchments for each channel link and each source node, as well as the corresponding divides, are determined from the previously defined drainage pattern and channel network. TOPAZ defines the connectivity of the channel network and subcatchments, which will be used in the flow and sediment routing through the channel network. TOPAZ deduces a variety of properties and parameters of the derived channel network, channel links and subcatchments.

The output from TOPAZ consists of report files, analysis log files, tables and raster data. The CCHE1D graphical user interface provides the input data for TOPAZ, reads TOPAZ output files and tables, visualizes the results, and converts the output into formats required by the watershed and channel network models.

### 5.2 Watershed Modeling

The Agricultural Non-Point Source (AGNPS, Young et al., 1987; Bosch et al., 1998) model simulates runoff water quality to evaluate potential pollution problems for agricultural watersheds, and to assess the effects of applying alternative management practices.

AGNPS is a continuous simulation model which uses geographic data cells of 1 to 40 acres to represent land surface conditions. Within the framework of the cells, runoff characteristics and transport processes for sediment, nutrients and chemical oxygen demand (COD) are simulated for each cell. Flows and pollutants are routed through the channel system to the basin outlet. Point source inputs (such as nutrient COD from animal feedlots) can also be simulated and combined with the non-point-source contributions.

Basic model components in AGNPS include hydrology, erosion, sediment transport and chemical transport. In hydrology component, runoff volume is calculated by the SCS (US Soil Conservation Service) curve number procedure. Peak flow rate is estimated by using an empirical equation, which takes into account drainage area, channel slope, runoff volume, and watershed length-width ratio. In each cell of the watershed, erosion is calculated from the Revised Universal Soil Loss Equation (RUSLE). Sediment routing is based on the effective transport capacity of the stream channels. Eroded soil and sediment yield are subdivided into particle size classes. In chemical transport component, the transport of nitrogen, phosphorus, and COD is calculated throughout the watershed. Chemical transport calculations are divided into soluble and sediment-absorbed phases. COD is assumed to be soluble and to accumulate without losses.

The AGNPS input consists of watershed data (area, number of cells, precipitation) and cell parameter data. The cell parameters include: SCS curve number, average land slope, slope shape factor, field slope length, channel data (slope, length, side slope and roughness), universal soil-loss equation data (erodibility, cropping and practice factors), soil texture, fertilization level, point-source indicator, gully source parameters, chemical oxygen demand factor, and a channel indicator for the presence of a defined channel in a cell.

The output of AGNPS, which consists of daily water runoff and sediment loads for each cell (subwatershed), is transferred to the CCHE1D channel network model as inflow boundary conditions.

## Chapter 6 Basic Data Requirements

### 6.1 Geometric Data

The geometry of the channel network is represented by cross sections, reach lengths and channel roughness.

#### 6.1.1 Cross Section Data

A cross section is specified by a set of node coordinates (transverse distance and bed elevation), with distances starting from an arbitrary point and extending from the left to the right bank. Cross section data should be provided by the user from the measured topography, at least for all source and junction nodes of the channel network. If cross section data for other nodes are missing, the CCHE1D interface will complement them using linear interpolation.

#### 6.1.2 Reach Length Data

The reach lengths between cross sections should consider the flows in main channel, and over the left and right flood plains. The main channel reach lengths are typically measured along the thalweg, and the overbank reach lengths are measured along the anticipated paths of the overbank flow. Usually, the values of these three reach lengths are close. However, they may be significantly different in cases of river bends or meandering main channels with straight overbanks. An average value among these three lengths should be used, since CCHE1D does not differentiate lengths along the main channel and flood plains.

For ungauged watersheds, the reach lengths extracted from DEM by TOPAZ can be directly used in the calculation of flow and sediment transport in channels. However, the resolution of DEMs is commonly in the order of 30m by 30m, which may not be accurate enough to produce data expected by numerical models in river hydraulics and morphology. If the measured lengths for the channel network are available, it is suggested that the measured lengths be used in the calculation.

#### 6.1.3 Channel Roughness Data

The Manning's roughness coefficient  $n$  is needed. The channel cross section is represented by a finite set of nodes or stations in CCHE1D, and the Manning's  $n$  is set at each segment between two nodes or stations, as shown in Fig. 2.2. Therefore, a value of the Manning's  $n$  should be given at each segment. The Manning's  $n$  may be variable to reflect the different hydraulic properties in channel bed, banks and flood plains.

### **6.1.4 Channel Junctions**

The definition of cross sections at a channel junction is shown in Fig. 3.2. Because the water elevations in the cross sections at the junction are set to be the same in Eqs. (3.26) and (3.27), these cross sections should be placed as close together as possible. The thalweg elevations of the tributary and mainstream cross sections should be close, to avoid the difficulty in imposing the same water surface elevations at three cross sections in low flow situations. The reach lengths from cross section 3 to cross sections 1 and 2 are not needed in the calculation, but other geometric data in these three cross sections should be provided.

## **6.2 Flow Data**

### **6.2.1 Inflow Discharge Conditions**

Inflow discharges at all source nodes and side discharges at internal nodes should be specified in the form of triangular hydrographs or as time series of discharge. The specification of inflow boundary conditions can be either subwatershed-oriented or node-oriented. The subwatershed-oriented approach is useful if a watershed model such as the AGNPS or SWAT is used to generate the runoff and sediment loads for each subwatershed. CCHE1D interface can automatically assign the outflow of subwatersheds to the corresponding nodes of the channel network. If the CCHE1D channel network model is used without integration with a watershed model, the node-oriented format should be used, where inflow data are directly referenced to nodes of the network.

### **6.2.2 Outlet Boundary Conditions**

CCHE1D requires that a value of water surface elevation (stage) be given at the downstream end of the channel network (watershed outlet). CCHE1D can handle the downstream boundary by specifying a non-reflective condition (i.e. open boundary condition). If a measuring flume is placed at the watershed outlet, CCHE1D will utilize its characteristics to determine the stage as a function of the discharge. However, in cases where the stage at the outlet is known, CCHE1D can import a data file containing a time series of stage. The user can also provide a stage-discharge rating curve.

## **6.3 Sediment Data**

### **6.3.1 Sediment Properties**

The grain sizes, specific gravity and grain shape factor of sediment are needed. The grain size classification is defined by the user according to the case under study. The number of size classes can vary for different cases. The median diameters, upper and lower bounds for all size classes should be provided. The default values of specific gravity and shape factor are 2.65 and 0.7, respectively.

### **6.3.2 Inflow Sediment Data**

Inflow sediment loads are given by triangular hydrographs or time series of sediment discharge at the upstream boundaries of main streams and tributaries, and at local inflow points. The time series of sediment discharge can be subwatershed-oriented or node-oriented. The inflow sediment gradation is needed for nonuniform sediment transport calculations.

### **6.3.3 Bed Material Data**

The initial bed-material gradation must be given for a realistic computation of stream behavior, particularly for the determination of scour and stability conditions. Information on bed-material gradation under the bed surface layer is also needed, if available. If only deposition is expected, like sedimentation in reservoirs, the initial bed-material gradation is less important.

The porosity of the bed material is also needed. Measured values should be used if available; otherwise the user can choose one of the empirical formulas to calculate it.

### **6.3.4 Bank Material Data**

The bank-material gradation and porosity must be given if bank erosion and mass failure are considered. If the bank material is cohesive, measured cohesion and friction angle of the bank material are needed. The critical shear stress for bank toe erosion is also needed. If the measured critical shear stress is not available, the user can adjust it through the interface.

## **6.4 Hydraulic Structure Data**

### **6.4.1 Bridge Crossings**

To define the geometric and hydraulic properties of bridge crossings shown in Fig. 3.4, the following data are required: upstream invert elevation, opening side slopes, opening bottom width, pier width, pier loss coefficient, and pier shape coefficient.

### **6.4.2 Culverts**

The CCHE1D model supports both pipe and box culverts. To define the geometric and hydraulic properties of pipe or box culvert shown in Fig. 3.3, the following data are required: number of culverts in a cross section, length, diameter or rise, span, upstream and downstream invert elevations, upstream and downstream superelevations, surface roughness (Manning's n), entrance loss coefficient, chart number and scale number (Table 3.1).

#### **6.4.3 Drop Structures**

To define the geometric and hydraulic properties of drop structures shown in Fig. 3.5, the following data are required: bottom width, length, side slopes, upstream invert elevation, and energy loss coefficient.

#### **6.4.4 Measuring Flumes**

To define the geometric and hydraulic properties of measuring flumes, the following data are required: length, compound cross section, upstream invert elevation, measuring section elevation, upstream and downstream superelevations, surface roughness (Manning's n). At each measuring flume, the rating curve is divided into up to four segments, and at each segment the curve is represented by an exponential function of  $Q = ch^m$ . Therefore, the user should provide the number of segments in the rating curve, and the depth at break point, coefficient c and exponent m for each segment.

### **6.5 Watershed Data**

Watershed modeling requires a wealth of information, such as ground elevation (DEM), land use, land cover, soil type, temperature, rain fall, agricultural operations, etc. Watershed models should use the definition of subwatersheds created by TOPAZ within CCHE1D so that data integration with the channel model is possible.

## Chapter 7 Model Verification and Testing

### 7.1 Comparison of Diffusive and Dynamic Wave Models

#### 7.1.1 Steady Backwater Profile due to Impoundment

Both diffusive and dynamic wave models were used to calculate the steady backwater profile due to impoundment. The study channel was 300m wide, with a rectangular cross section. The Manning's roughness coefficient was 0.04. Bed slopes were 0.2% and 0.5%, and for each bed slope the flow discharges used were 2000m<sup>3</sup>/s, 4000m<sup>3</sup>/s and 6000m<sup>3</sup>/s. The flow depth at the outlet was 25m. For the purpose of comparison, all the numerical parameters in the two models were the same except the diffusive wave assumption.

Fig. 7.1 shows the water surface profiles calculated with both flow models for the case of bed slope 0.5% and flow discharge 6000m<sup>3</sup>/s. The water surface calculated from the diffusive wave model is higher than that from the dynamic wave model in the transition region, while both models provide nearly identical results for the normal flow in the upstream approach reach and the flow in the downstream backwater region. Table 7.1 shows the differences between water surface elevations calculated by the two models for all the cases. Also shown in Fig. 7.2 is the relative difference in water elevation as function of the Froude number in the upstream approach reach. Here, the relative difference in water elevations is based on the local flow depth calculated by the dynamic wave model. The maximum absolute difference has a value of 0.996m and the maximum relative difference is 27.8% when the Froude number in the upstream approach reach is 0.96. When the Froude number is less than 0.5, the relative difference is less than 5%.

Table 7.1 also shows the difference between backwater region lengths calculated with the two models. Here, the backwater region length is defined as the distance from the downstream outlet to the location where the backwater surface elevation is 1% higher than the normal water surface elevation. The relative difference is 18.8% when the Froude number in the upstream approach reach is 0.96. The relative difference is larger if the flow discharge is larger or if the bed slope is steeper. Furthermore, in case of steeper bed slopes (e.g. 1% and 0.5%), the backwater region length calculated with the diffusive wave model increases as the flow discharge increases, which is qualitatively opposite to the results from the dynamic wave model. Therefore, caution should be given when the diffusive wave model is applied to the impoundment case in steep channels.

The influence of computational grid lengths was also studied. Two different grid lengths were used in each case of bed slopes 0.005 and 0.002, shown in Table 7.1. However the calculated results are very close. Larger grid lengths have also been tested, but it is found that if the grid length is too large, the difference in backwater region lengths calculated by diffusive and dynamic wave models can not be well established.

Table 7.1 Comparison between Diffusive and Dynamic Wave Models  
in the Case of Impoundment

$S_0$ (%)	$Q$ (m <sup>3</sup> /s)	$h_0$ (m)	$Fr_0$	$\Delta x$ (m)	$\Delta y_m$ (m)	$r_{ym}$ (%)	$L_{dif}$ (m)	$L_{dyn}$ (m)	$\Delta L$ (m)	$r_{\Delta L}$ (%)
1.0	6000	3.534	0.961	50	0.996	27.8	2587.02	2177.71	409.32	18.8
	4000	2.760	0.928	50	0.679	24.5	2548.40	2247.11	301.29	13.4
	2000	1.809	0.875	50	0.367	20.1	2518.53	2407.79	110.74	4.60
0.5	6000	4.362	0.701	50	0.502	10.2	5273.93	4683.75	590.18	12.6
				100	0.501	10.2	5272.99	4681.77	591.22	12.6
	4000	3.409	0.676	50	0.368	9.58	5162.02	4748.35	413.67	8.71
				100	0.366	9.50	5162.68	4752.28	410.39	8.64
0.2	2000	2.235	0.637	50	0.215	8.47	5060.96	4836.75	224.22	4.64
				100	0.213	8.31	5063.22	4839.97	223.26	4.61
	6000	5.769	0.461	100	0.252	3.73	13766.53	12881.01	885.52	6.87
				250	0.252	3.73	13683.64	12810.64	873.00	6.81
0.08	4000	4.506	0.445	100	0.189	3.56	13254.87	12633.30	621.57	4.92
				250	0.189	3.56	13218.85	12608.31	610.53	4.84
	2000	2.954	0.419	100	0.113	3.24	12794.34	12460.53	333.81	2.68
				250	0.112	3.20	12789.95	12456.82	333.13	2.67
0.08	6000	7.629	0.303	250	0.131	1.45	36696.34	35460.39	1235.95	3.49
	4000	5.958	0.293	250	0.101	1.42	34600.34	33681.63	918.71	2.73
	2000	3.905	0.276	250	0.062	1.32	32633.97	32129.65	504.32	1.57

Note:  $S_0$  = bed slope;  $Q$  = flow discharge;  $h_0$ ,  $Fr_0$  = flow depth and Froude number in the upstream approach reach;  $\Delta x$  = grid length;  $\Delta y_m$  = maximum water elevation difference calculated by the two models;  $r_{ym}$  = maximum relative water elevation difference by the two models;  $L_{dif}$ ,  $L_{dyn}$  = backwater region lengths calculated by the diffusive wave model and the dynamic wave model, respectively;  $\Delta L$  = difference between  $L_{dif}$  and  $L_{dyn}$ ;  $r_{\Delta L}$  = relative difference with respect to  $L_{dyn}$ .

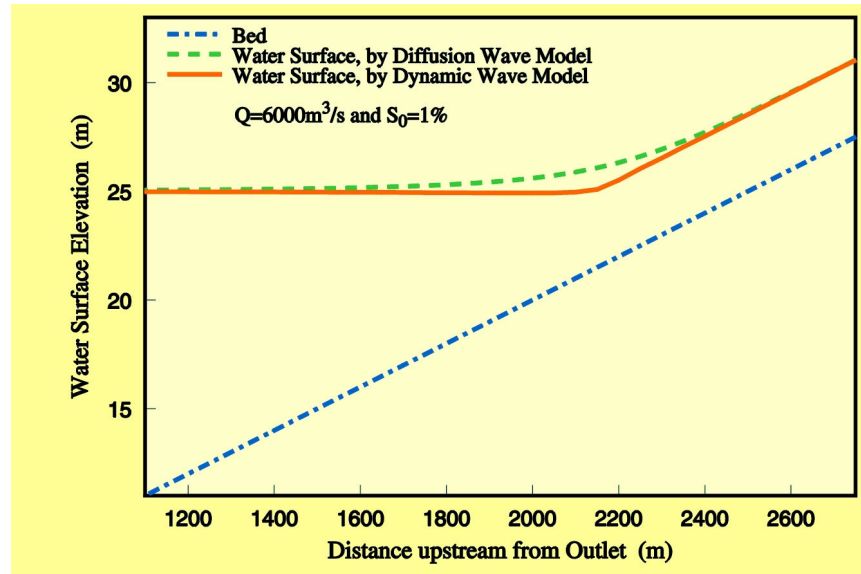


Fig. 7.1 Backwater Surface Profile due to Impoundment

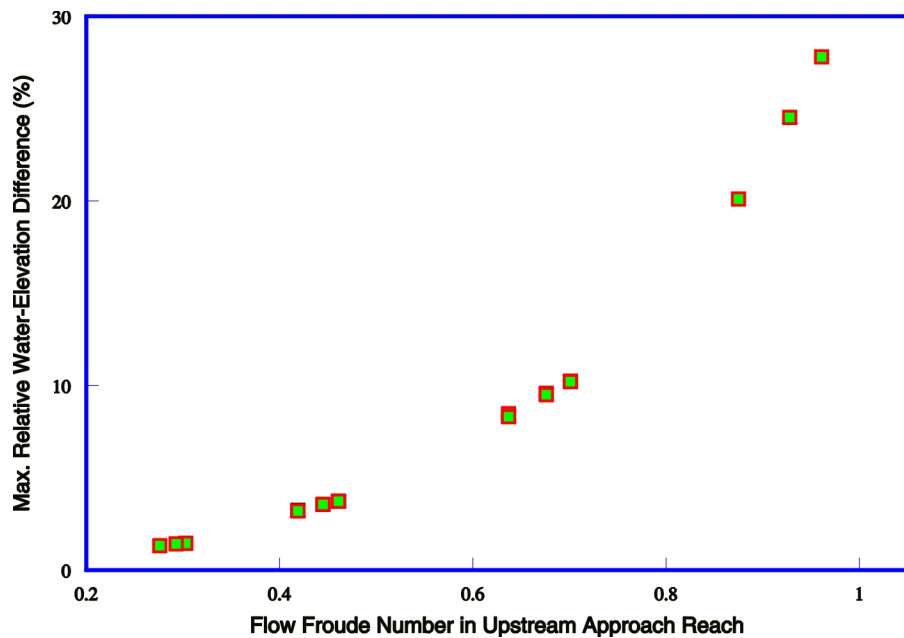


Fig. 7.2 Maximum Water Elevation Difference vs. Upstream Froude Number in the Case of Impoundment

### 7.1.2 Steady Flow through a Channel Contraction

The dynamic and diffusive wave models were compared in case of channel contraction. Fig. 7.3 shows the configuration of the study channel. The cross section was rectangular. The channel width varied from 300m to 100m through a 500m-long transition reach. Two approaching reaches with uniform widths of 300m and 100m were situated upstream and downstream of the contraction so that uniform flow was achieved in both parts. Bed slope was constant along the whole channel, but various values of 0.2%, 0.5% and 1.0% were used in order to study the influence of bed slope, and to achieve a wide range of Froude numbers. The flow discharges used were 2000m<sup>3</sup>/s, 4000m<sup>3</sup>/s, 6000m<sup>3</sup>/s and 8000m<sup>3</sup>/s. The Manning's roughness coefficient  $n$  was 0.04. The computational grids were uniform, with a grid length of 100m.

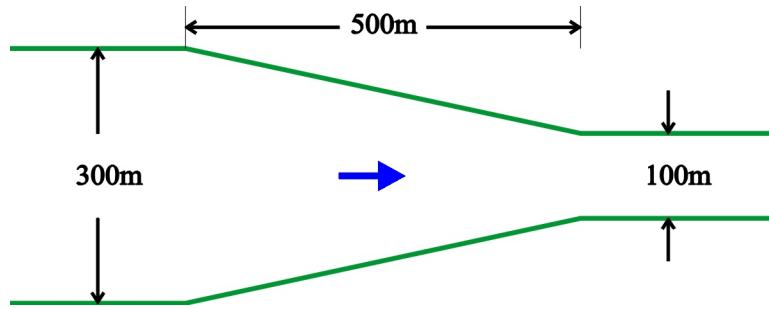


Fig. 7.3 Configuration of Channel Contraction

Fig. 7.4 shows the water surface profiles calculated with both diffusive and dynamic wave models for the case of bed slope 0.5% and flow discharge 8000m<sup>3</sup>/s. The water surface calculated from the diffusive wave model is lower than that from the dynamic wave model in the transition region, while identical results in the upstream and downstream normal flow regions are obtained with two models. Table 7.2 shows the maximum differences between water surface elevations calculated by the two models for 12 cases. Here, the relative difference in water surfaces is based on the local flow depth calculated by the dynamic wave model. The maximum relative water elevation difference is proportional to the flow discharge and Froude number. This maximum relative difference is up to 29.5% when the upstream approach Froude number is 0.986. When the approach Froude number is less than 0.5, this relative difference is less than 10%.

From the above comparison of diffusive and dynamic wave models in steady flow cases of impoundment and channel contraction, it has been observed that two models show significant differences in the transition regions due to the channel geometry change. This difference is related to the flow discharge, Froude number, channel geometry, etc. Under uniform flow condition, both models provide identical results, even though the Froude

number is larger than 0.5. The reason is that in the case of uniform flow the gradient of velocity along the longitudinal direction is zero and the diffusive wave assumption is valid.

Table 7.2 Comparison of Diffusive and Dynamic Wave Models  
in the Case of Steady Flow through a Contraction

$S_0$ (%)	$Q$ ( $\text{m}^3/\text{s}$ )	$h_{dw}$ (m)	$h_{up}$ (m)	$Fr_{up}$	$\Delta y_m$ (m)	$r_{ym}$ (%)
1.0	8000	8.912	4.208	0.986	-2.750	-29.47
	6000	7.397	3.534	0.961	-2.096	-26.20
	4000	5.689	2.760	0.928	-1.372	-22.03
	2000	3.631	1.809	0.875	-0.693	-16.92
0.5	8000	11.184	5.196	0.719	-2.078	--18.44
	6000	9.277	4.362	0.701	-1.623	--17.77
	4000	7.129	3.409	0.676	-1.121	-16.72
	2000	4.545	2.235	0.637	-0.570	-13.72
0.2	8000	15.077	6.924	0.467	-1.244	-8.38
	6000	12.505	5.769	0.461	-1.006	-8.20
	4000	9.607	4.506	0.445	-0.743	-7.94
	2000	6.122	2.954	0.419	-0.433	-7.44

Note:  $S_0$  = bed slope;  $Q$  = flow discharge;  $h_{dw}$  = flow depth in the downstream reach;  $h_{up}, Fr_{up}$  = flow depth and Froude number in the upstream approach reach;  $\Delta y_m$  = maximum water elevation difference by diffusive and dynamic wave models;  $r_{ym}$  = maximum relative water elevation difference by two models.

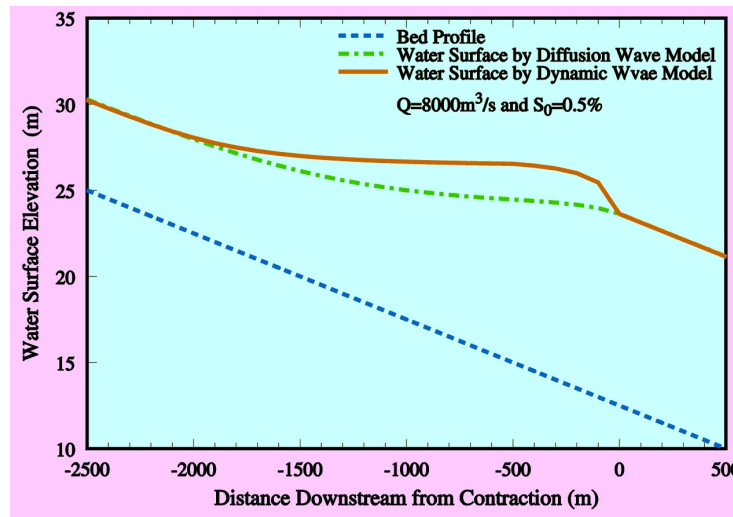


Fig. 7.4 Water Surface Profile through a Channel Contraction

### 7.1.3 Unsteady Flow in a Rectangular Straight Channel

The unsteady flow in an open channel with a rectangular cross section was calculated with both the diffusive and dynamic wave models. The channel was 300m wide and the Manning's  $n$  was 0.04. Bed slopes were 0.008 and 0.002. The inflow hydrograph was generated with a gamma function. The base flow discharge was 1000m<sup>3</sup>/s, and the time to peak was 48 minutes. The flow discharges calculated with both flow models were compared. Shown in Table 7.3, the peak flow discharges and the times to peak at the outlet calculated by two models are very close. The relative difference is less than 1%.

Table 7.3 Comparison of Diffusive and Dynamic Wave Models in the Case of Unsteady Flow in a Rectangular Straight Channel

$S_0$ (%)	$Q_b$ (m <sup>3</sup> /s)	$Q_{p,in}$ (m <sup>3</sup> /s)	$t_{p,in}$ (min)	$Q_{p,out,dif}$ (m <sup>3</sup> /s)	$t_{p,out,dif}$ (min)	$Q_{p,out,dyn}$ (m <sup>3</sup> /s)	$t_{p,out,dyn}$ (min)	$\Delta Q$ (%)	$\Delta t$ (%)
0.008	1000	8000	48	7663.01	94	7701.28	94	-0.50	0.0
	1000	6000	48	5737.31	100	5763.96	100	-0.46	0.0
	1000	4000	48	3822.87	108	3839.38	108	-0.43	0.0
	1000	2000	48	1930.43	126	1935.36	126	-0.25	0.0
0.002	1000	8000	48	6210.46	130	6251.96	129	-0.66	+0.78
	1000	6000	48	4688.79	139	4720.52	138	-0.67	+0.72
	1000	4000	48	3194.04	152	3214.42	151	-0.63	+0.66
	1000	2000	48	1726.97	176	1734.45	175	-0.43	+0.57

### 7.1.4 Unsteady Flow in a Natural Channel Network

The diffusive and dynamic wave models were compared in the simulation of unsteady flow in the channel network of the Goodwin Greek watershed. The detailed information on this watershed is introduced in Section 8.1 of this manual. The computational channel network was extracted from a DEM by TOPAZ. Ten in-stream measuring flumes and 4 culverts were considered. The inflow hydrographs from upland areas for all the storms were generated by SWAT. 1192 storm events between 1978 and 1995 were calculated. The discharge hydrographs at the watershed outlet calculated with both models were compared. Fig. 7.5 shows the difference between the peak discharges calculated by both models. The relative differences in peak discharges in most of the cases are less than 1%. The lower the flow discharge, the larger the relative difference. This is due to the fact that in the low flow season the influence of hydraulic structures, bed forms and channel geometry on the flow is stronger than in the flood season. Fig. 7.6 shows the difference between the times to peak discharge calculated by both models. The relative difference is less than 4% for most storms.

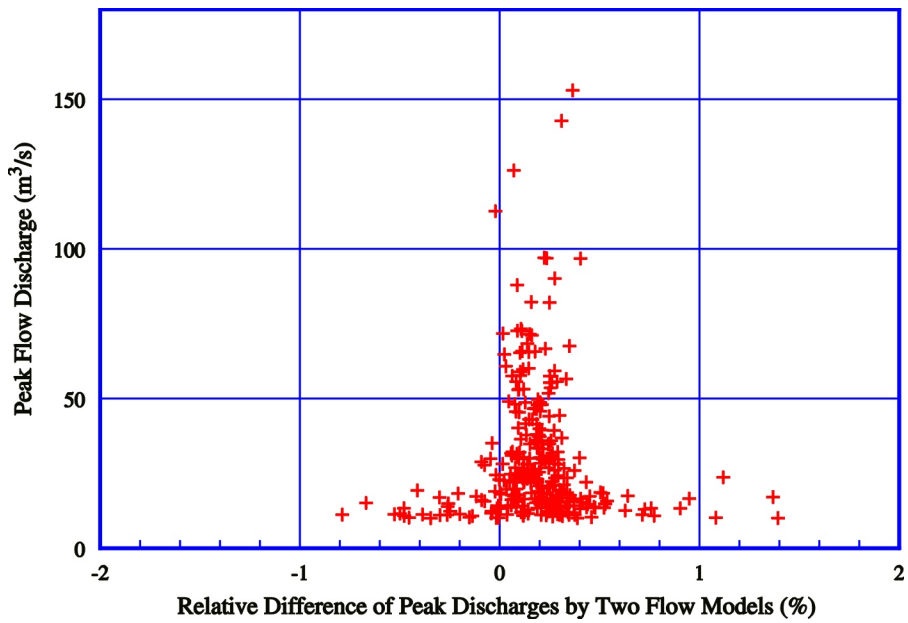


Fig. 7.5 Difference between the Peak Discharges in Goodwin Creek Outlet Calculated by Diffusive and Dynamic Wave Models

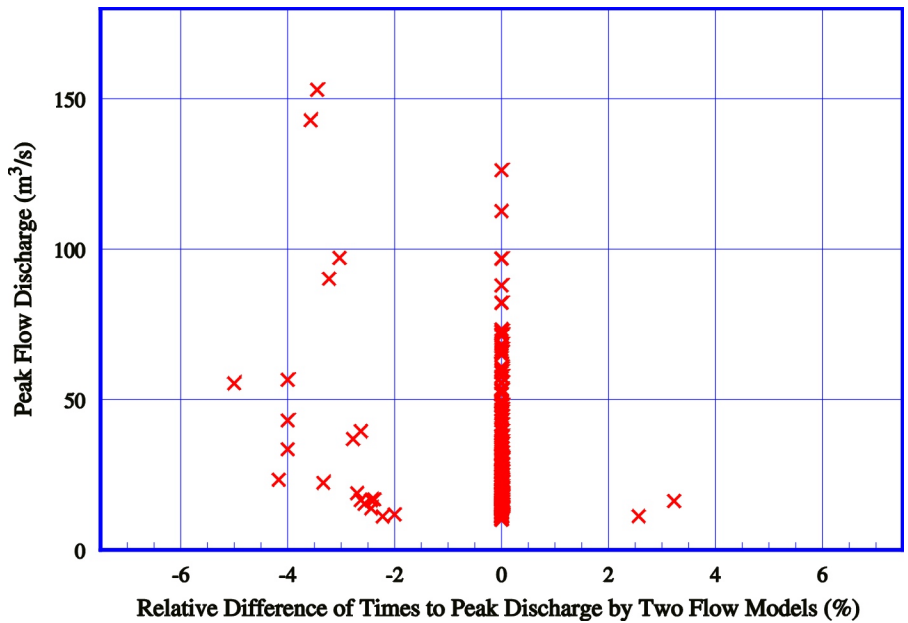


Fig. 7.6 Difference between the Times to Peak Discharge in Goodwin Creek Outlet Calculated by Diffusive and Dynamic Wave Models

## 7.2 Test of Sediment Transport Capacity Formulas

The four non-cohesive sediment transport capacity formulas implemented in CCHE1D were tested against 1859 sets of uniform bed-material load data chosen from Brownlie's (1981) data collection by limiting the standard deviation of bed material  $\sigma < 1.2$  and the Shields parameter  $\theta > 0.055$ . These data had been observed in several decades by many investigators, which cover the flow discharges of  $0.00094\sim297\text{m}^3/\text{s}$ , the flow depths of  $0.01\sim2.56\text{m}$ , the flow velocities of  $0.086\sim2.88\text{m/s}$ , the surface slopes of  $0.0000735\sim0.0367$ , and the sediment sizes of  $0.088\sim28.7\text{mm}$ . The comparison of the calculated and measured transport rates is shown in Table 7.4. One can see from Table 7.4 that all the implemented formulas provide very good results for uniform sediment transport capacity. Almost 80% of the predictions are in the error range between 0.5 and 2. Similar test using the same data set was also conducted on Yang's (1973, 1984) bed-material load transport formula, which also provide good prediction. Because Yang's formula is adopted in the SEDTRA module, it is not implemented individually in the CCHE1D model.

In addition, Wu et al.'s (2000) bed load formula (4.62) was separately tested against 1345 sets of uniform bed load data selected from the previous 1859 sets of Brownlie's uniform bed-material load data by limiting the Rouse number  $\omega / \kappa u_* > 2.5$ . A comparison was also conducted with four widely adopted bed-load transport formulas of Meyer-Peter and Mueller (1948), Bagnold (1966), Engelund and Fredsøe (1976) and van Rijn (1984a). As shown in Table 7.5, Wu et al.'s bed load formula (4.6) provides the best results. Van Rijn's formula's results are not very good, because the used data exceed its applicability size range of  $0.2\sim2\text{mm}$  suggested by van Rijn (1984a).

The four non-cohesive sediment formulas were also tested against the nonuniform sediment data collected by Toffaleti (1968), including the experimental data observed by three groups of investigators: Nomicos, Einstein-Chien and Vanoni-Brooks, and the field data in the Rio Grande River, the Middle Loup River, the Niobrara River and the Mississippi River. The total number of fractional transport rate data is 539. In order to avoid the deficiency in the measurement of suspended load close to river bed, the used field data were chosen by limiting the lowest measurement point on the depth to be lower than  $0.2\text{m}$  (lower than  $0.4\text{m}$  in a few of the Mississippi River Data). These data cover flow discharges up to  $21,600\text{m}^3/\text{s}$ , flow depths up to  $17.5\text{m}$ , and sediment sizes from  $0.062\text{mm}$  to  $1\text{mm}$ . Table 7.6 shows the comparison between the calculated and measured fractional transport rates of nonuniform bed-material load. It is found that the Ackers and White's formula modified by Proffit and Sutherland systematically over-predicts for these data and provides the worst results. The reason may be the used data exceeded the applicability range of the modified Ackers and White's formula, which can not be applied to very fine sediment. Wu et al.'s formula and SEDTRA module predict nonuniform bed-material load transport better than other two formulas.

The same tests were also conducted for the modified Zhang's formula (Wu and Li, 1992b) and Karim's (1998) formula. The modified Zhang's formula is only for the fractional transport rate of suspended load, and it is combined here with Wu et al.'s bed load formula (4.60) to obtain the fractional bed-material load transport rate. The modified Zhang's formula and the Karim's formula provide reasonably good predictions. Because the modified Zhang's formula does not explicitly have a correction factor for the hiding and exposure effect in nonuniform sediment transport and Karim's correction factor can be used only in a very narrow range, these two formulas are not implemented in the CCHE1D model.

Table 7.4 Comparison of Calculated versus Measured Transport Rates of Uniform Bed-Material Load using Brownlie's Data

Error Ranges	Percentages (%) of Calculated Transport Rates in Error Ranges				
	Ackers & White	Yang	Engelund & Hansen	SEDTRA	Wu et al.
$0.8 \leq r \leq 1.25$	37.3	33.4	33.6	36.6	40.4
$0.667 \leq r \leq 1.5$	57.9	56.6	55.4	59.1	62.7
$0.5 \leq r \leq 2$	82.4	76.6	77.0	78.1	81.3

Note:  $r = \text{calculation} / \text{measurement}$ .

Table 7.5 Comparison of Calculated versus Measured Transport Rates of Uniform Bed Load using Brownlie's Data

Error Ranges	Percentages (%) of Calculated Transport Rates in Error Ranges				
	Van Rijn	Engelund & Fredøe	Bagnold	Meyer-Peter & Mueller	Wu et al
$0.8 \leq r \leq 1.25$	14.8	21.4	21.4	21.3	38.7
$0.667 \leq r \leq 1.5$	25.3	37.4	38.9	39.4	59.3
$0.5 \leq r \leq 2$	44.0	54.1	57.2	66.2	80.1

Table 7.6 Comparison of Calculated versus Measured Fractional Transport Rates of Nonuniform Bed-Material Load using Toffaleti's Data

Error Ranges	Percentages (%) of Calculated Transport Rates in Error Ranges					
	Modified Ackers & W.	Modified Engelund&H.	Karim	Modified Zhang	SEDTRA	Wu et al
$0.5 \leq r \leq 2$	5.6	27.8	42.7	48.1	56.9	57.9
$0.333 \leq r \leq 3$	11.1	40.3	63.5	67.9	73.1	76.1
$0.25 \leq r \leq 4$	20.8	49.0	73.3	80.7	80.9	85.2

## 7.3 Model Test against Experimental Data

### 7.3.1 Degradation of Channel Bed with Uniform Sediment

Newton (1951) performed experiments of channel degradation in a straight flume 9.14m long, 0.3048m wide and 0.61m deep. Sediment was fed at the upstream inlet of the flume by a motor-driven elevator, and was trapped in a bucket at the downstream end of the flume (see Fig. 7.7). Standard 20-30 Ottawa sand was used, which was remarkably consistent in size and shape, with mean size of 0.690mm, specific gravity of 2.65 and porosity between 0.34 and 0.42.

For each experiment, an equilibrium condition for the selected flow and sediment discharges was first established. Equilibrium state was considered to have reached when the average sediment rates at the inlet and outlet became equal, and when the water and bed surfaces reached essentially constant slope and elevation. In this state the bed forms were fully developed. Thereafter, the inflow sediment was cut off while the constant flow discharge and adequate flow depth were maintained during the test. The bed started to degrade until a new equilibrium state was reached.

The bed degradation processes in experiment runs 1 and 3 were calculated with the CCHE1D model. The calculation domain was the experimental reach upstream of the bucket, and consisted of 40 subreaches with a uniform grid length of 0.2285m. The time step length was 0.5 minute. Table 7.7 lists the flow and sediment conditions. For both runs, the measured Manning's roughness coefficient  $n$  for the flume bed was used, which was represented by a regressive function from the measured data with an initial value of about 0.016 and a value of about 0.012 at the final (or equilibrium) stage. The Manning's coefficient of 0.009 was used for the flume walls, which were believed to be very smooth. The Manning's coefficient for the entire cross section was calculated with the Einstein's method,  $n^{3/2}\chi = n_b^{3/2}\chi_b + n_w^{3/2}\chi_w$ . Here  $\chi_b$ ,  $\chi_w$  and  $\chi$  are the wetted perimeters for bed, walls and entire cross section, and  $n_b$ ,  $n_w$  and  $n$  are the Manning's coefficients for bed, walls and entire cross section. The open boundary condition for the flow was imposed on the outlet boundary, because the outlet water elevation measured was not constant and the distance from the bucket to the downstream weir was omitted in the calculation. The dynamic wave model was used to simulate the flow.

The non-equilibrium transport model was used to simulate sediment transport. Following Bell and Sutherland (1983), the adaptation length for non-equilibrium sediment transport was chosen as a function of time  $t$ . Many functions were tried, but  $L_s = 1 + 0.5t$  provides the best result among all the trials. This function was also used by Choudhury (1996) in his calculation for the same case using the CCHE2D model. The bed-material porosity calculated with Eq. (4.69) was 0.396, which was in the range of measured values 0.34-0.42 and was therefore used in the calculation.

The four sediment transport formulas implemented in the code were used to determine the sediment transport capacity. Because the sediment was uniform, the hiding and exposure correction factors used in these four formulas should be 1. This is satisfied automatically in SEDTRA module (Garbrecht et al., 1995), Wu et al's (2000) formula and the modified Engelund and Hansen's formula. The correction factor in the modified Ackers and White's formula proposed by Proffitt and Sutherland (1983) is not 1 in this case, but it is set to 1 in order to return to the original Ackers and White's 1973 formula. Wu et al's formula and Ackers and White's formula provide good results for the degradation process, but SEDTRA module and Engelund and Hansen's formula underpredict the scouring process. Shown in Figs. 7.8 and 7.9, the patterns of channel degradation are well reproduced by the numerical model with the sediment transport capacity being calculated with Wu et al's formula and Ackers and White's formula. Fig. 7.10 shows the comparison of the measured and calculated sediment discharges at the outlet for run 1. The error is less than 20% for using both Ackers and White's formula and Wu et al's formula. The agreements are generally good.

Fig. 7.11 shows the bed scour depths of run 3 calculated with the CCHE1D model using Wu et al's sediment transport capacity formula. Two functions  $L_s = 1 + 0.5t$  and  $L_s = t$  were tested. It is found that  $L_s = 1 + 0.5t$  provides better results than  $L_s = t$ . The difference between the results from these two functions is very small at the beginning, and is larger but still not significant at the final stage. This means that the calculated bed scouring process is insensitive to the adaptation length  $L_s$ . This behavior of the CCHE1D sediment transport model increases the level of confidence in the application of this model to situations where  $L_s$  has to be specified empirically.

Table 7.7 Flow and Sediment Conditions in Newton's (1951) Experiments

Exp.	Flow Discharge (m <sup>3</sup> /s)	Sediment Size (mm)	Initial Bed Slope (m/m)	Initial $n_b$	Final $n_b$	Duration (hour)
Run 1	0.00566	0.69	0.0046	0.016	0.012	24
Run 3	0.00566	0.69	0.0061	0.016	0.012	27

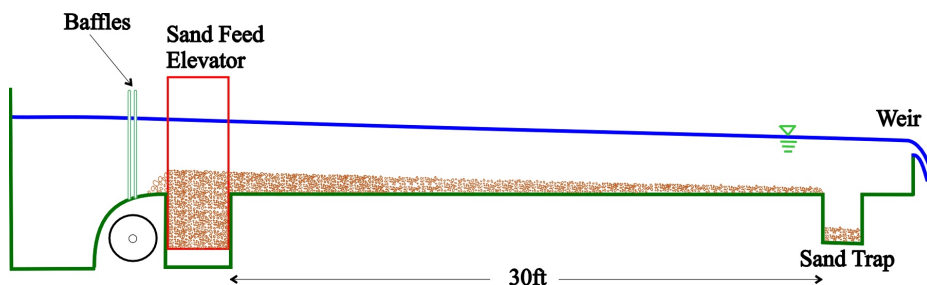


Fig. 7.7 Configuration of Newton's (1951) Experiment

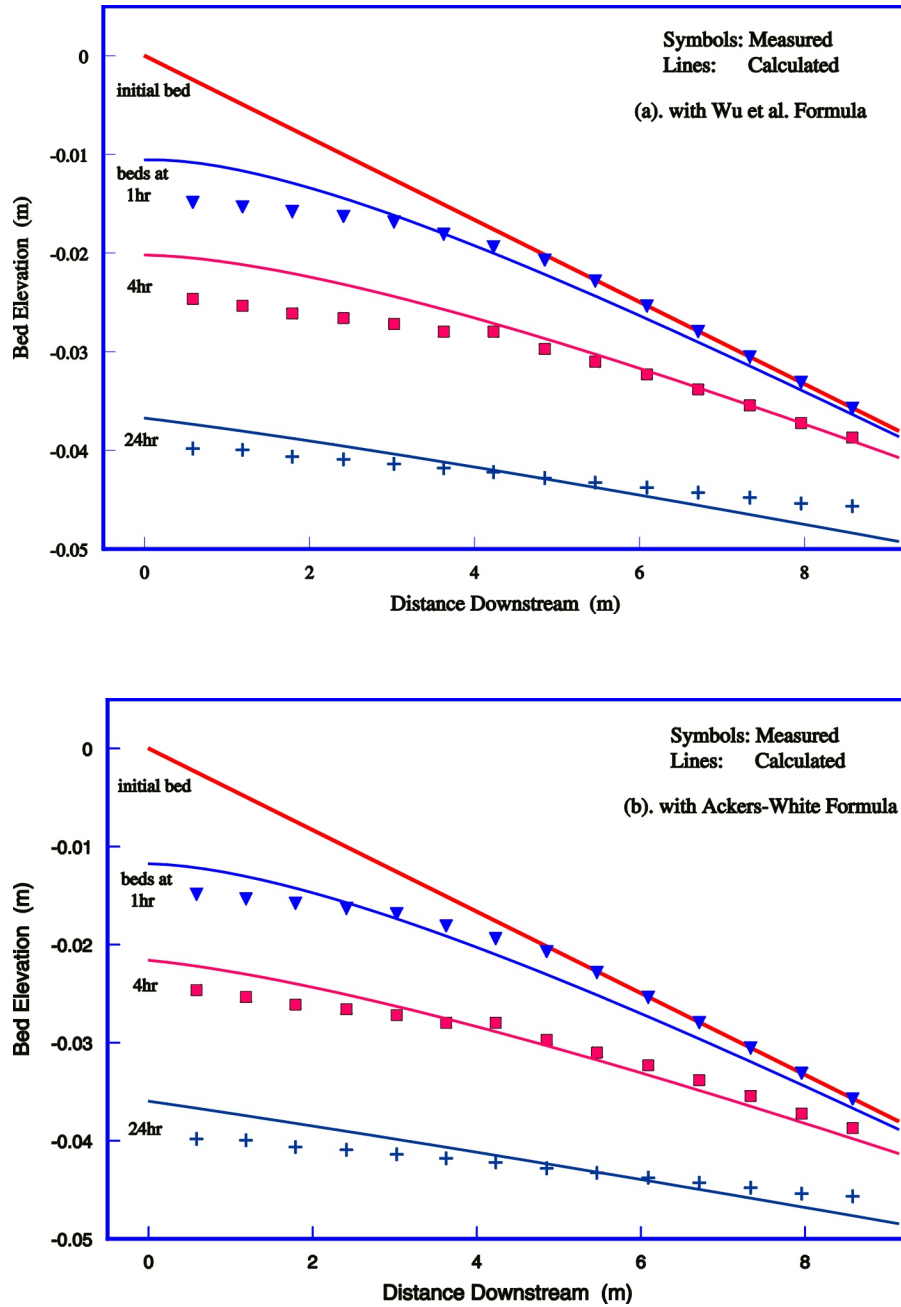


Fig. 7.8 Calculated vs. Measured Bed Profiles for Newton's Exp. Run 1

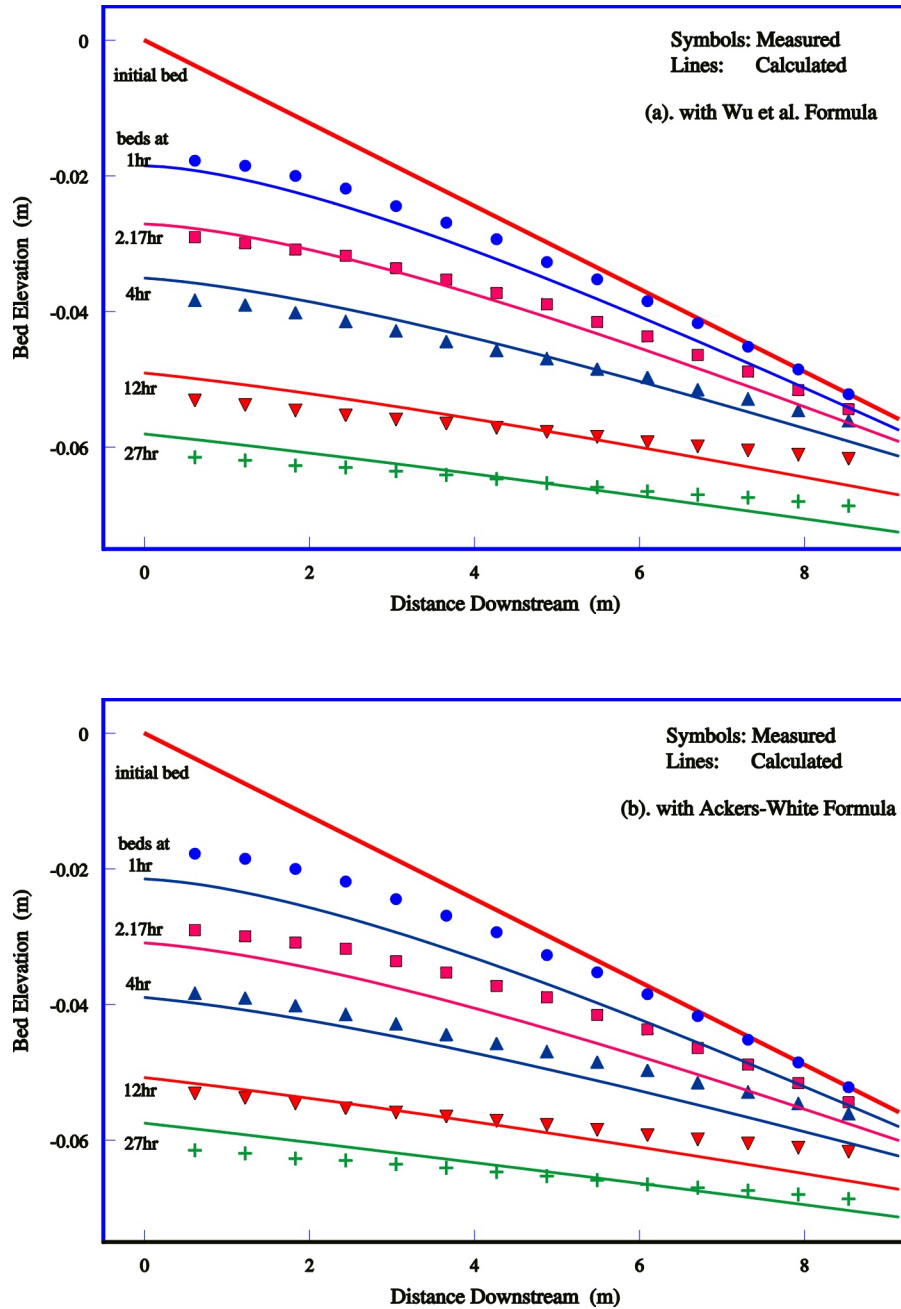


Fig. 7.9 Calculated vs. Measured Bed Profiles for Newton's Exp. Run 3

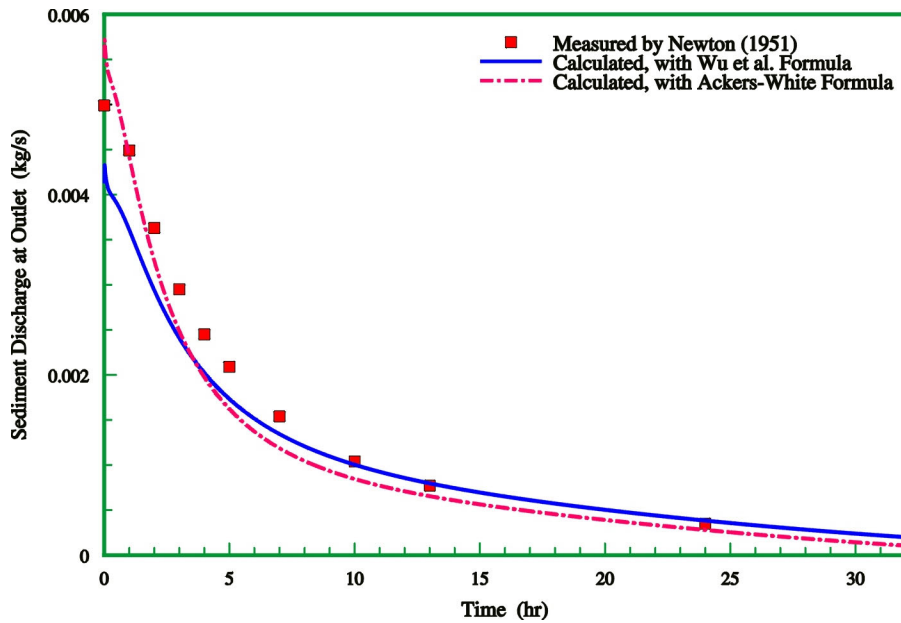


Fig. 7.10 Sediment Discharges at Outlet for Newton's Exp. Run 1

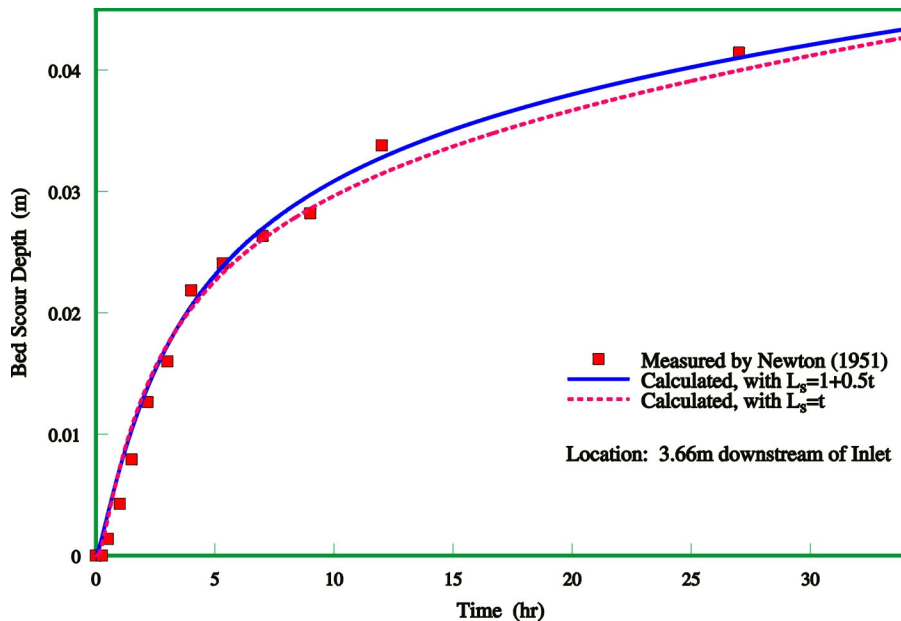


Fig. 7.11 Bed Scour Depths with Time (Newton's Exp. Run 3)

### 7.3.2 Degradation of Channel Bed with Non-uniform Sediment

Ashida and Michiue (1971) performed experiments to investigate bed degradation and armoring processes downstream of a dam. The experimental flume was 0.8m wide and 20m long. The flume bed was filled with nonuniform sediment with median size of 1.5mm and standard deviation of 3.47. Clear water was pumped into the flume at a constant discharge. The eroded sediment was captured with a sampling apparatus placed at the downstream end. A weir was positioned at the end of the flume to adjust water elevation. The experimental run 6 was simulated using the CCHE1D model. The inlet flow discharge was 0.0314 m<sup>3</sup>/s and the initial bed slope was 0.01. The computational grid consisted of 40 equal-length intervals of 0.5m. The time step was 10 seconds. At the downstream end the open boundary condition was imposed because the outlet water elevation was not exactly constant in the experiment. The bed-material porosity was calculated with Komura and Simmons' (1967) formula, and it was variable during the calculation because of the change of bed-material size. The mixing layer thickness was set to the median size of the parent bed material used in the experiment. The adaptation length  $L_s$  was set to 7.3h.

According to the trends of scour observed in the experiment, the entire scouring process could be divided into two periods. In the first period, from the start to about 120 minutes (for run 6), the bed intensively eroded, while in the second period the erosion rate reduced and an armoring layer formed gradually. The Manning's coefficient of the channel (including flume walls) in the final stage was, according to measurements, about 0.021, and the Manning's coefficient for the flume bed was estimated at about 0.023. The simulation considered the process of development of bed forms, from the initial flat bed to a fully developed bed. This process was approximately represented with a linear function between bed form height and time. The time needed to complete this development process was unknown and here a value of about 60 minutes was adopted. The Manning's coefficient for the bed in this period was calculated with the relationship  $n_b = \Delta^{1/6}/A$ , in which  $\Delta$  is the bed form height obtained from the assumed linear function, and  $A$  is a coefficient (see Li and Liu, 1967; Wu and Wang, 1999). Certainly the bed form development in this period was very complicated and the adopted method was only an approximation.

All of the four sediment transport capacity formulas implemented in the code were applied to this case, but only Wu et al's formula provided good results. Fig. 7.12 shows the comparison of the measured and calculated bed scour depths at 7m, 10m and 13m upstream from the weir. The scour depths calculated with the CCHE1D model using Wu et al's sediment transport capacity formula agree very well with the experimental data. The trends of the intensive scour in the initial period and the weak scour in the final equilibrium stage are very well reproduced. Fig. 7.13 shows the measured and calculated bed-material gradations in 600 minutes at 10m upstream from the weir. The agreement is generally good. The calculated gradation shown in the figure is that of the mixing layer. Under the mixing layer, the size distribution is unaltered. The armoring process is also well predicted.

Fig. 7.14 shows the sensitivity of the calculated scour depth to the adaptation length  $L_s$ . Several functions for  $L_s$ , such as  $L_s = 7.3h$ ,  $L_s = t$  and  $L_s = 1 + 0.5t$ , were tested. The function  $L_s = 7.3h$  provides the best result for the bed scour process, especially the scour trend to the equilibrium state. The result from  $L_s = t$  is also very close to the measured data. The result from  $L_s = 1 + 0.5t$  deviates more but is still close. It is found that the calculated scour depth is not sensitive to  $L_s$ . Even when  $L_s$  is given greatly different values, the calculated scour depths are still very close.

The sensitivity of the calculated scour depth to the mixing layer thickness was analyzed by changing the value of mixing layer thickness from one time the median size of the parent mixture to twice that value. Fig. 7.15 shows the results. It is found that the thicker the mixing layer, the larger the equilibrium scour depth. The mixing layer thickness is important to the determination of the equilibrium scour depth and also to the calculation of the size distribution of the armoring layer.

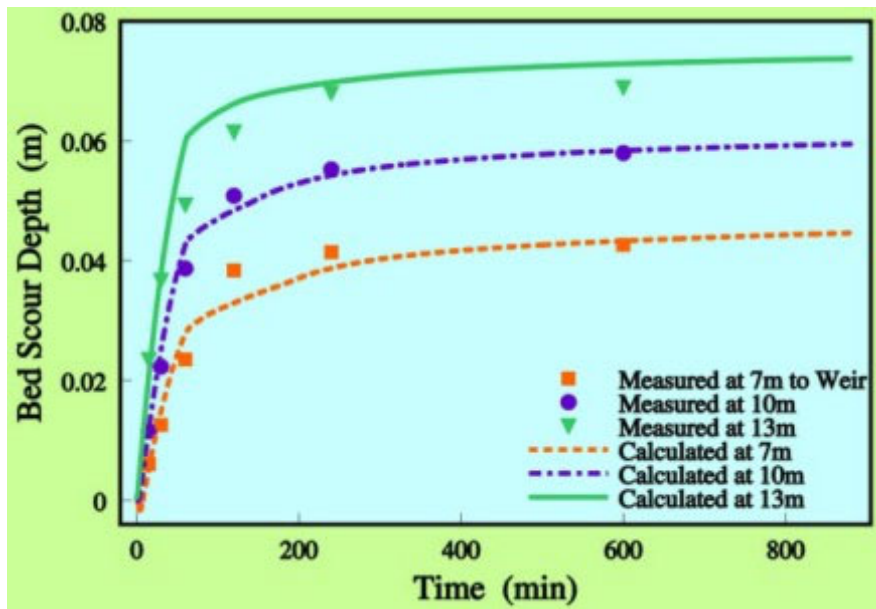


Fig. 7.12 Measured vs. Calculated Scour Depths with Time  
(Ashida and Michiue's Exp. Run 6)

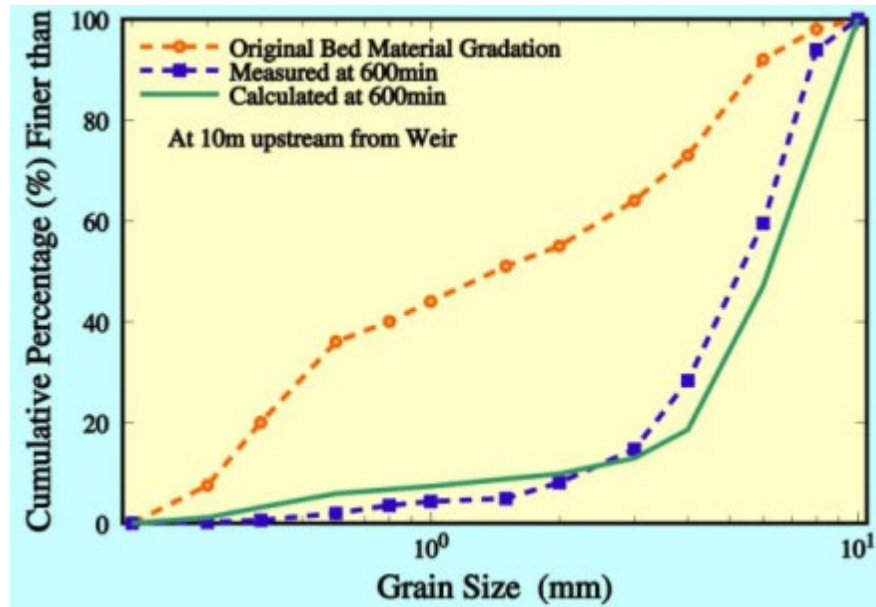


Fig. 7.13 Measured vs. Calculated Bed-Material Gradations  
(Ashida and Michiue's Exp. Run 6)

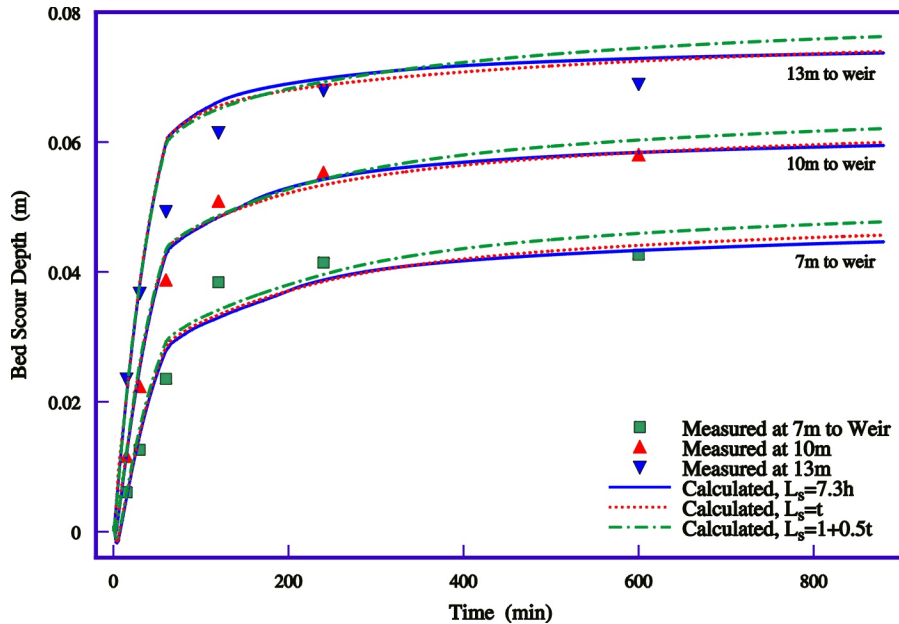


Fig. 7.14 Sensitivity of Bed Scour Depth to  $L_s$  (Ashida and Michiue's Exp. Run 6)

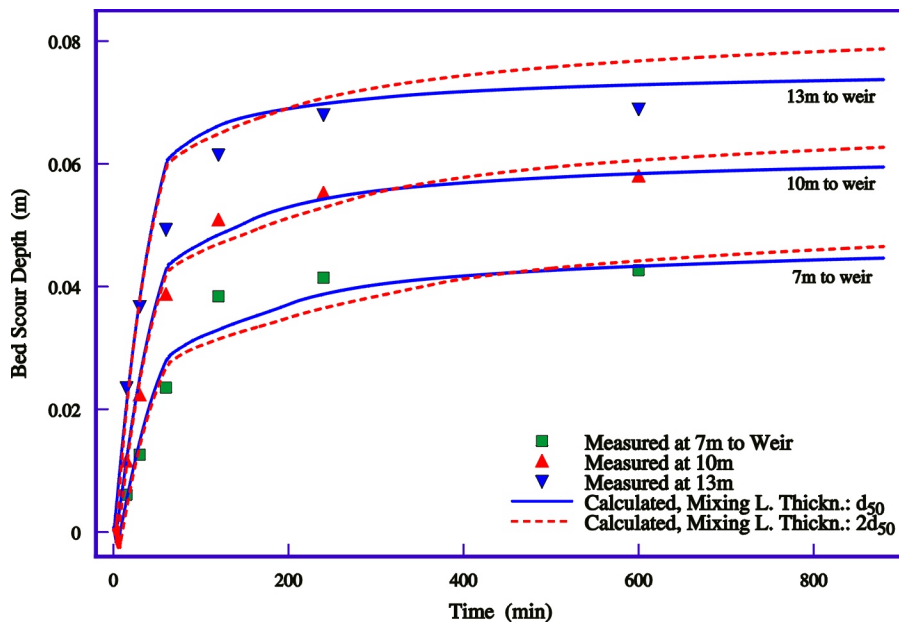


Fig. 7.15 Sensitivity of Bed Scour Depth to Mixing Layer Thickness (Ashida and Michiue's Exp. Run 6)

### 7.3.3 Channel Aggradation due to Non-uniform Sediment Overloading

The channel aggradation experiments performed at the St. Anthony Falls Hydraulic Laboratory (SAFHL; see Seal et al., 1995) were used to test the CCHE1D model. The configuration of the experiment is shown in Fig. 7.16. The experimental reach of the flume was 45m long and 0.305m wide, with an initial bed slope of 0.002. The channel walls were covered with a smooth, impermeable polyvinyl chloride (PVC) membrane. A ramp at a 45° slope was attached at the downstream end, and the tailgate was placed 3m downstream of the base of the ramp. The tailgate was kept at a constant height for each of the three runs, and the water surface at the tailgate was high enough to produce an undular hydraulic jump at the downstream end of the main gravel deposit. Sediment was fed into the experimental channel manually at the specified feed rate 1m downstream from the headgate. The feed sediment was a weakly bimodal mixture comprising a wide range of sizes from 0.125mm to 64mm, the gradation of which is shown in Fig. 7.17. An aggradational wedge developed due to sediment overloading. Its front gradually moved downstream while the upstream bed elevation continued to rise. Experiment runs 1 and 2 are calculated with the CCHE1D model. In these two runs the same water discharge  $0.049\text{m}^3/\text{s}$  was used. Sediment feed rates were 11.30kg/min and 5.65kg/min, and tailgate water elevations were 0.40m and 0.45m, respectively.

The computational domain was 45m long, consisting of 90 intervals uniformly distributed. The time step was 30 seconds. The bed-material porosity was set to 0.23 for runs 1 and 2, a value that had been confirmed by comparing the measured and calculated volumes of the deposit. The Manning's coefficient for the channel bed was about 0.03, and the Manning's coefficient for the channel walls was 0.009. The Manning's coefficient for the entire cross section was calculated with the Einstein's method. The adaptation length  $L_s$  was set to 0.5m and the mixing layer thickness was calculated with Eq. (4.77) at a first attempt.

Fig. 7.18 provides the comparison of the measured and predicted bed profiles at various times, as well as the final water surface profiles for experiment run 2. Because the dynamic wave model was used, the hydraulic jump downstream of the gravel deposit front was well predicted. This hydraulic jump can not be simulated if the diffusive wave model is used. The bed profiles were well predicted by using all the four sediment transport formulas. Table 7.9 summarizes the properties of the aggradational wedges for runs 1 and 2. The calculated locations, heights and celerities of the gravel deposit front, as well as the calculated bed slopes, are in good agreement with the measurements. The bed profiles calculated using the SEDTRA module are not so smooth as those using Wu et al's sediment transport formula, the modified Ackers-White formula or the modified Engelund-Hansen formula. This may be due to the transition problem among the three formulas used by the SEDTRA module. Another problem in SEDTRA is that the value of the power index  $x$  is very sensitive and should be carefully evaluated for each case under study. In this case it was given a value of 0.63 because the sediment mixture was weakly bimodal.

The sensitivity of the calculated bed profile to the adaptation length  $L_s$  was analyzed by defining  $L_s$  as 0.5m, 2m and 7.3h. Here,  $h$  is the average flow depth over the wedge from the inlet to the gravel deposit front, and 7.3h equals to about 1m. Shown in Fig. 7.19,  $L_s$  has very little influence on the bed slope over the wedge, and on the location, height and celerity of the gravel deposit front. The only significant influence is on the slope of the deposit front. The longer the adaptation length, the smaller the slope of the deposit front. However this is only local. As a whole, the influence of  $L_s$  on the calculated bed profiles is limited.

Fig. 7.20 shows the sensitivity of the calculated bed profile to the mixing layer thickness. The mixing layer thickness was given as  $d_{50}$ ,  $6d_{50}$  and  $0.5\Delta$ , but the difference among the calculated bed profiles is very small. As the mixing layer thickness increases six times, the deposit front just moves downstream about 1.3%. The influence of the mixing layer thickness on the deposition process is much less than on the scouring process.

Table 7.8 Flow and Sediment Conditions in SAFHL's (1995) Experiments

Experiment	Flow Discharge ( $\text{m}^3/\text{s}$ )	Inlet Sediment Discharge (kg/min)	Initial Bed Slope (m/m)	Outlet Water Level (m)	Duration (hour)
Run 1	0.049	11.30	0.002	0.40	16.83
Run 2	0.049	5.65	0.002	0.45	32.4

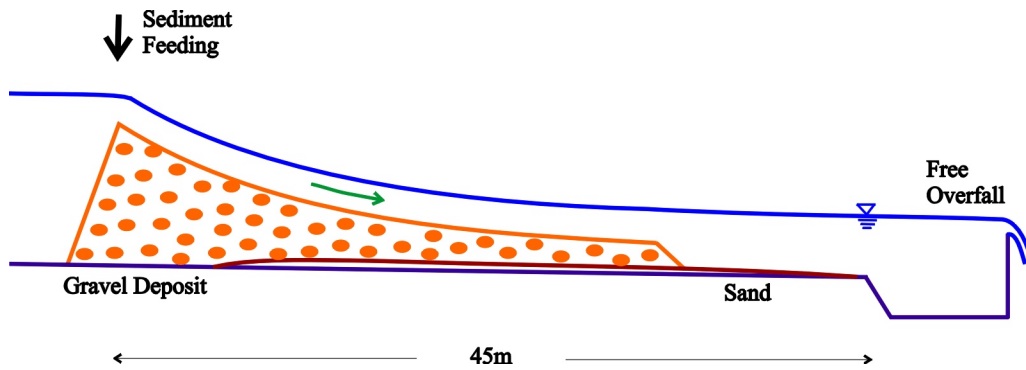


Fig. 7.16 Configuration of SAFHL's (1995) Experiment

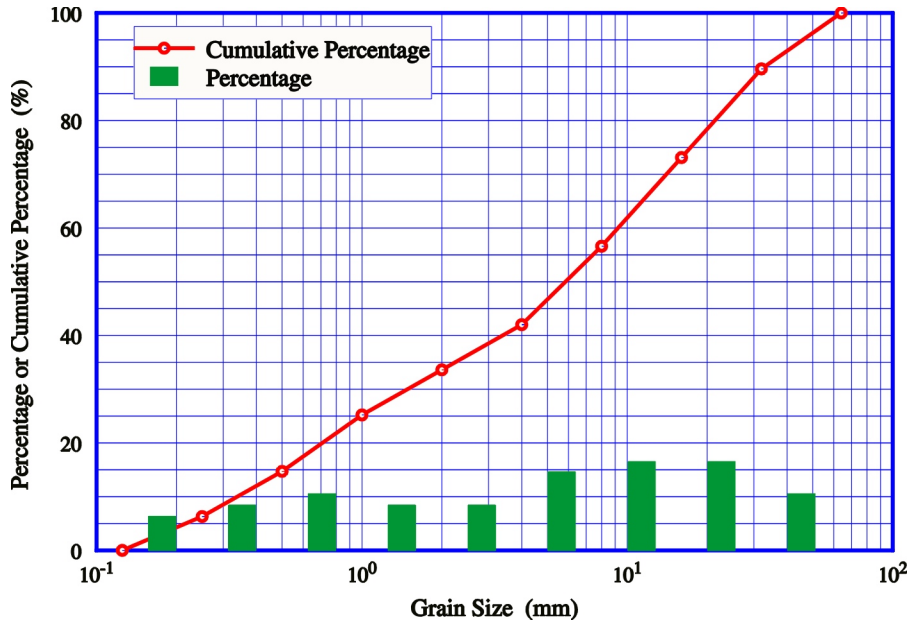


Fig. 7.17 Size Distribution of Input Sediment Mixture  
in SAFHL's Experiments

Table 7.9 Measured and Calculated Properties of Bed Profiles

Experiment	Properties	Measured	Calculated with CCHE1D using Capacity Formula			
			Wu et al	Ackers-W.	Engelund-H.	SEDTRA
Run 1	Final Front Location (m)	36.8	40.0	36.0	37.0	43.0
	Front Celerity (m/hr)	2.187	2.377	2.139	2.198	2.555
	Front Height (m)	0.233	0.196	0.209	0.198	0.191
	Upper Bed Slope (m/m)	0.022	0.0220	0.0243	0.0295	0.0202
	Lower Bed Slope (m/m)	0.014	0.0137	0.0177	0.0150	0.0116
Run 2	Final Front Location (m)	36.8	38.5	35.0	38.0	40.0
	Front Celerity (m/hr)	1.136	1.188	1.080	1.173	1.235
	Front Height (m)	0.247	0.231	0.250	0.230	0.211
	Upper Bed Slope (m/m)	0.019	0.0200	0.0211	0.0202	0.0169
	Lower Bed Slope (m/m)	0.013	0.0124	0.0160	0.0131	0.0130

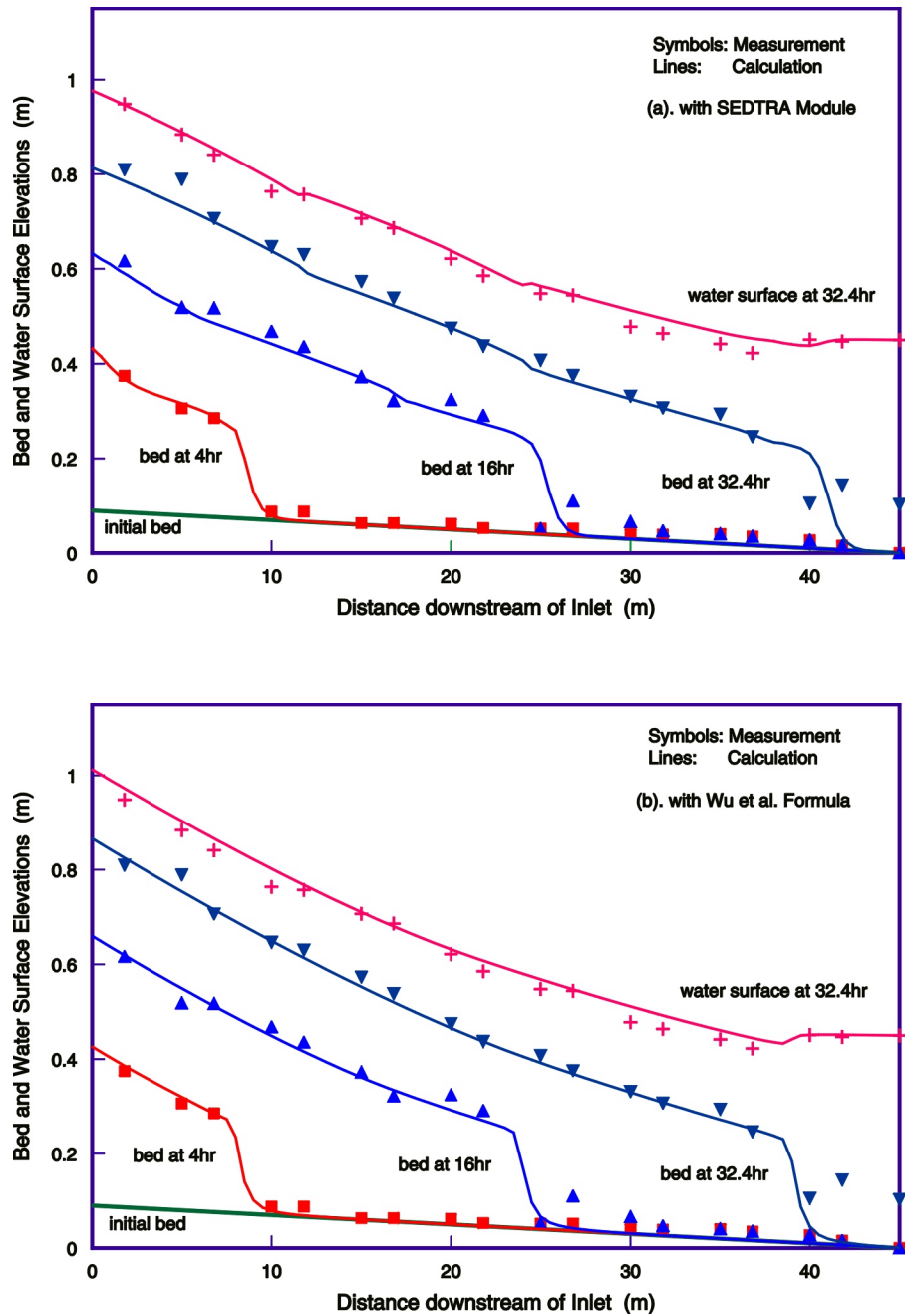


Fig. 7.18 Bed and Water Surface Profiles for SAFHL's Experiment Run 2

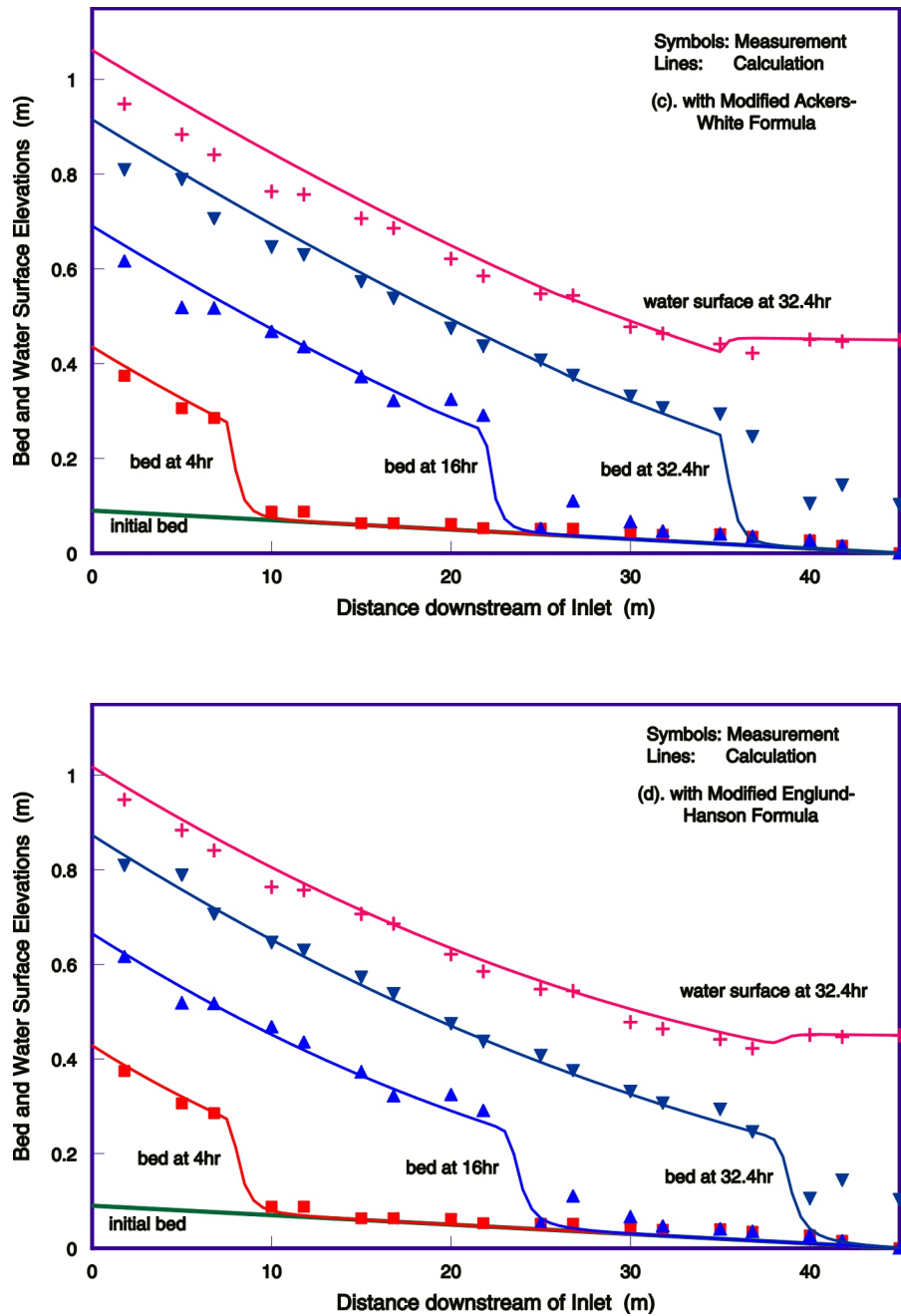


Fig. 7.18 Bed and Water Surface Profiles for SAFHL's Experiment Run 2 (Continued)

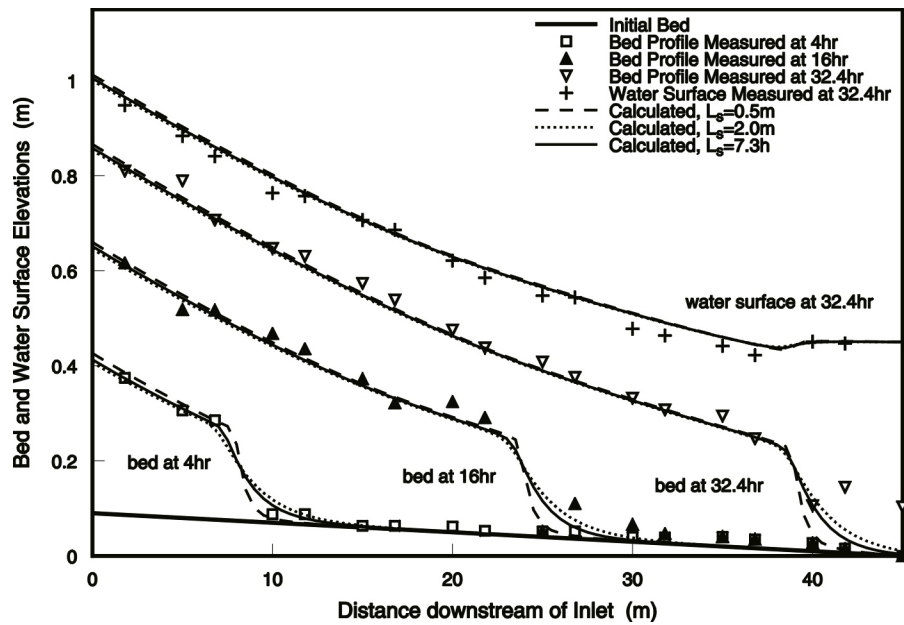


Fig. 7.19 Sensitivity of Bed Profile to  $L_s$  (SAFHL's Experiment Run 2)

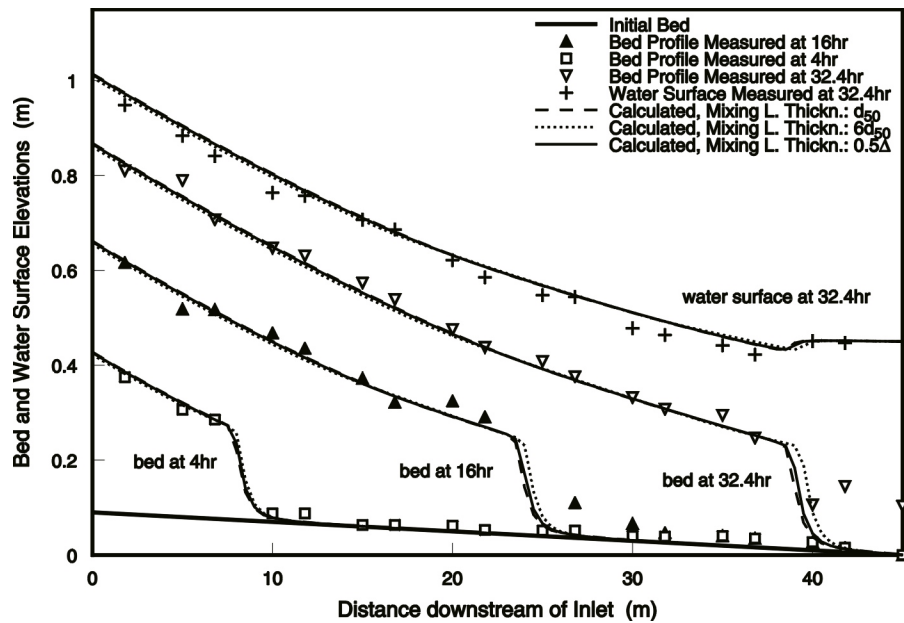


Fig. 7.20 Sensitivity of Bed Profile to Mixing Layer Thickness  
(SAFHL's Experiment Run 2)

## 7.4 Model Test against Field Data

### 7.4.1 Flood Routing in the Pu-Tze River

The Pu-Tze River is one of the major rivers in south Taiwan (Fig. 7.21). Its length is 75.67km, and the area of the drainage basin is 426.60 km<sup>2</sup>. The average annual rainfall is 1851.2 mm, and the average annual runoff is 551.49 million m<sup>3</sup>. The study reach is located at the lower and middle of this river, from the estuary to the Niu-Chou-His Bridge Station. The total length of the study reach is 39.95km, and is represented by 98 cross-sections. The average bed slope of the study reach is 0.053%, and the flow is most likely in the subcritical region. There are five main tributaries flowing into this reach. Because information on the enormous sediment mining operations in this reach and on the sediment from the upstream main stream and tributaries was not known, only the flood routing in the main stream was simulated using the CCHE1D model. The measured flow discharge at the Niu-Chou-His Bridge (inlet) was used as the inflow condition from the upstream main stream. The flow discharges from five tributaries, which were estimated from the measured flow discharges at the Niu-Chou-His Bridge and the Wan-Nei Bridge (21.07km to the estuary) according to the relevant drainage areas and rainfalls at the five subbasins (Cheng et al., 2000), were used as side inflow conditions. The influence of the tidal flow in the estuary region was not considered, so the downstream boundary condition was given as a constant water stage. The simulation period included several storms during 1996-1997. The channel geometry measured in 1996 was used. The computation time step was one hour.

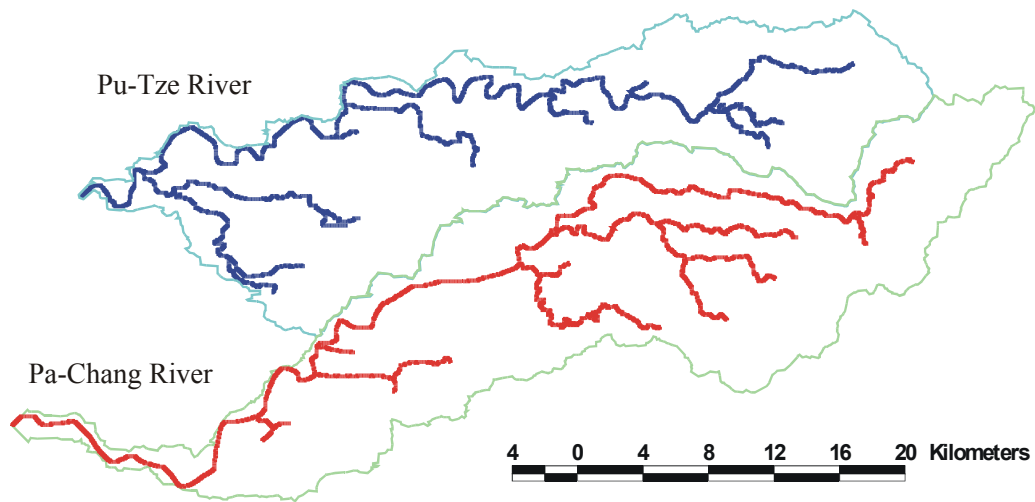


Fig. 7.21 Channel Networks of the Pu-Tze River and the Pa-Chang River  
(Excluding Channels of Strahler Order 1)

In the first attempt, it was found that the water surface elevation at the inlet was underestimated when using the Manning's roughness coefficient for channel design. Therefore, the measurement data from several storms before 1996 were used to calibrate the Manning's coefficient, and then the calibrated values were used to predict the flood routing after 1996. The time period of the calibration was about one week, while the time period of the prediction was about four days. Fig. 7.22 shows the comparison of the measured and simulated flow discharges at the Wan-Nei Bridge in both calibration and prediction periods. Figs. 7.23 and 7.24 show the comparisons of the measured and simulated water stages at the Wan-Nei Bridge and the Niu-Chou-His Bridge. The agreement between measurement and simulation is generally good. The overall trend of the flood routing in this river as well as the peak discharges and stages and the times to peak are generally well predicted. Some deviations exist, which may be attributed to the error in the estimation of the tributary inflow conditions and other factors.

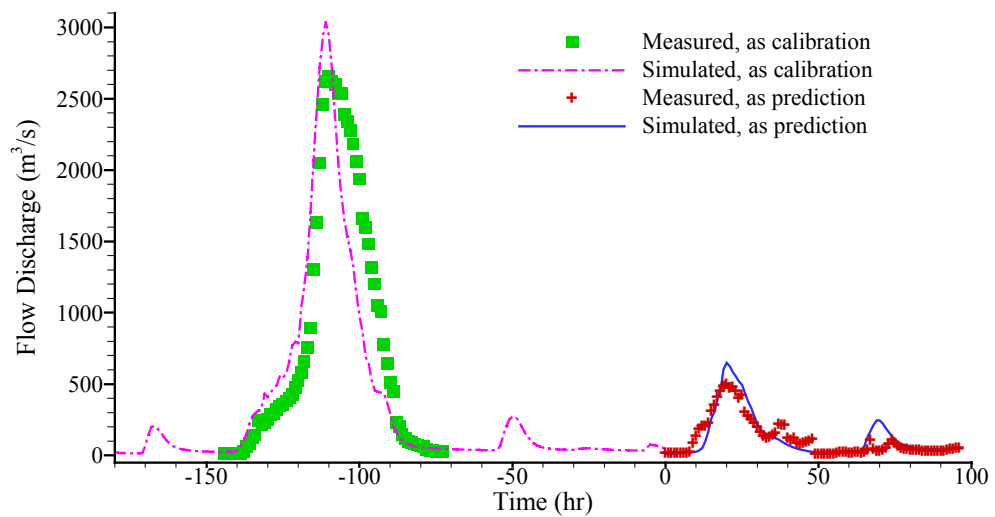


Fig. 7.22 Measured vs. Simulated Flow Discharges at Wan-Nei Bridge of Pu-Tze River

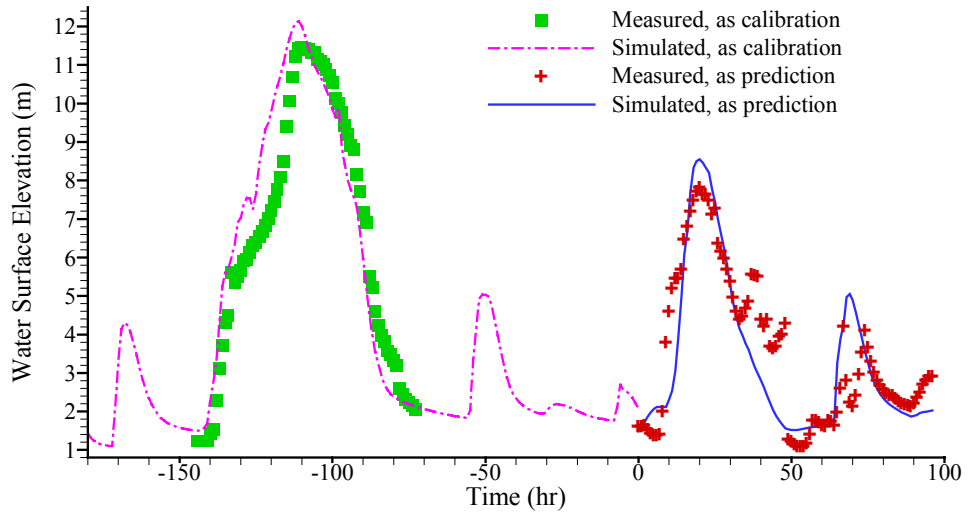


Fig. 7.23 Measured vs. Simulated Water Stages at Wan-Nei Bridge of Pu-Tze River

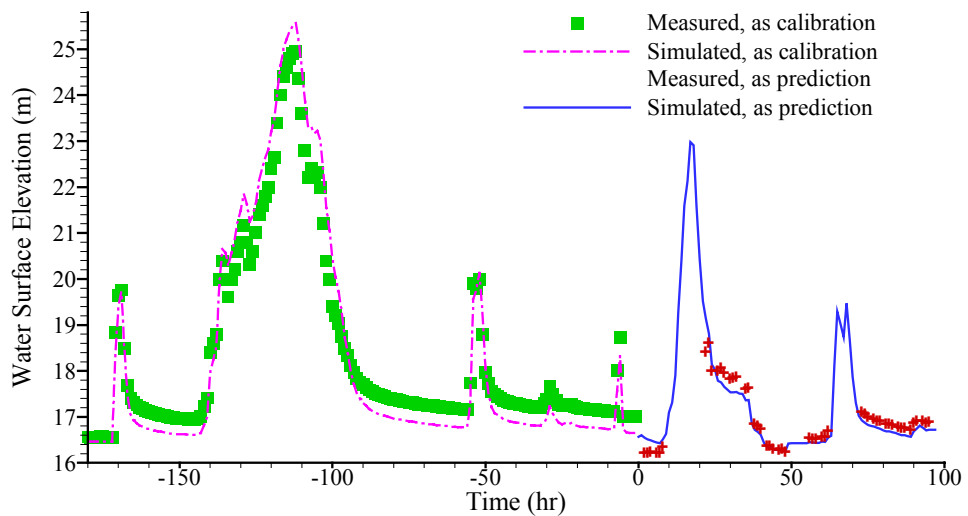


Fig. 7.24 Measured vs. Simulated Water Stages at Niu-Chou-His Bridge of Pu-Tze River

### 7.4.2 Long-Term Sedimentation Process in the Danjiangkou Reservoir

The Danjiangkou reservoir is located on the Hanjiang River, one of the largest tributaries of the Yangtze River. It has been under operation since 1968. Because a large tributary, the Danjiang River, joins the Hanjiang River just at the upstream of the dam, the Danjiangkou reservoir has two branches with nearly equivalent storage capacities. The total storage capacity at normal conditions is 17.45 billion m<sup>3</sup>, while the storage capacity of the branch in the Hanjiang River is 9.4 billion m<sup>3</sup>. Only the sedimentation process in the branch of the Hanjiang River was simulated. The water in the Hanjiang River flows into the Danjiang River during flood seasons, but the interaction between these two branches was neglected because their confluence is very close to the dam.

The computational domain included a 188 km-long reach in the main stream from the downstream of Baihe Hydrology Station to the dam, and a 12 km-long reach in the tributary Duhe River, which joins the Hanjiang River at 157km upstream of the dam. Sixty-one cross-sections were distributed in the main stream and four cross-sections were in the tributary. The simulation period comprised 13 years, from 1968 to 1980. The inflow water and sediment discharges used in the simulation were based on the measurements from the Baihe and Huanlongtan Hydrology Stations, at the inlets of the studied main stream and tributary. The measured Manning's roughness coefficient and bed-material porosity (see Danjiangkou , 1991) were used in the calculation.

Fig. 7.26 shows the comparison of the calculated and measured annual sediment depositions in different years, which illustrates the good agreement between measured and computed yields. In particular, the simulated annual depositions using three different sediment transport capacity formulas, Wu et al's (2000) formula, SEDTRA module and the modified Engelund and Hansen's formula, are very close to measured values. The modified Ackers and White's formula (Proffitt and Sutherland, 1983) did not provide reasonable results in this case. The reason being is that the sediment particle size in Danjiangkou Reservoir is very fine, beyond the applicability range of Ackers and White's formula.

Fig. 7.27 shows the calculated vs. measured longitudinal distributions of sediment depositions. Results simulated using Wu et al's sediment transport capacity formula are in good agreement with the measured data. Both the SEDTRA module and the modified Engelund and Hansen's formula over-predict deposition in the upper part of the reservoir and under-predict the deposition in the lower part.

Figs. 7.28 and 7.29 show the sensitivity of the simulated annual sediment depositions and the simulated longitudinal distribution of the deposition with respect to the non-equilibrium adaptation coefficient  $\alpha$ . The  $\alpha$  was calculated with Arminini and di Silvio's (1988) method and specified four values: 0.25, 0.5, 1.0 and 2.5. As the  $\alpha$  increases from 0.25 to 2.5, the sediment deposition in the reservoir increases and thus the sediment flushed out decreases. The values 0.5 – 1.0 of  $\alpha$  provide better results. The results calculated with the  $\alpha$  being determined by the Arminini and di Silvio's method are almost the same as those using  $\alpha=1.0$ , and also very close to the measurements.

Fig. 7.30 shows the sensitivity of the calculated longitudinal distribution of sediment deposition (1968-1979) with respect to the mixing layer thickness. The mixing layer thickness was given three values, 0.05m, 0.25m and 0.5 $\Delta$ . The calculated results are not sensitive to the variation of the mixing layer thickness. The results from using the three values of mixing layer thickness are very close to the measurements.

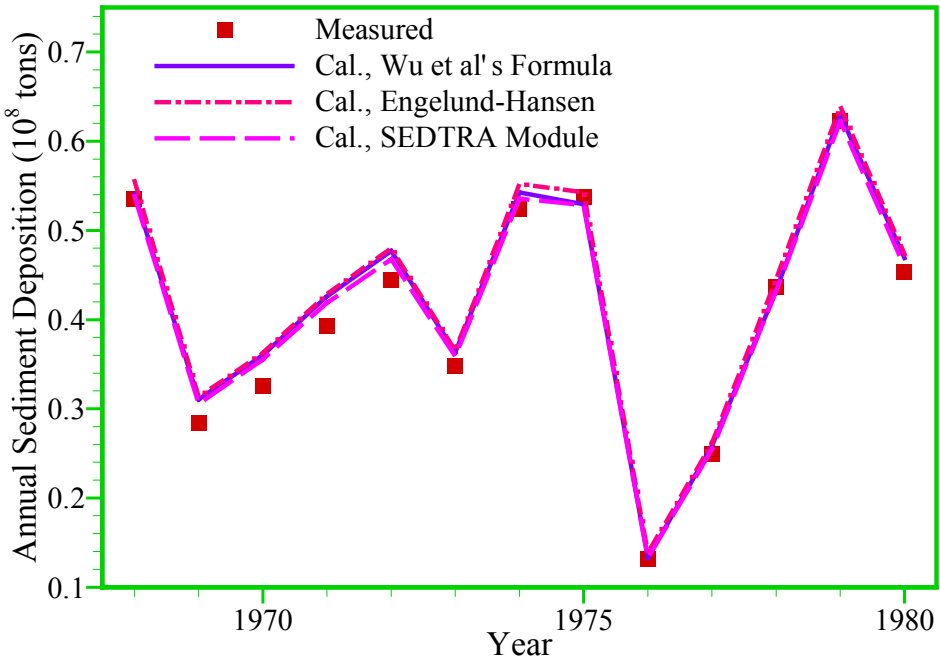


Fig. 7.26 Measured vs. Calculated Annual Sediment Depositions in the Danjiangkou Reservoir

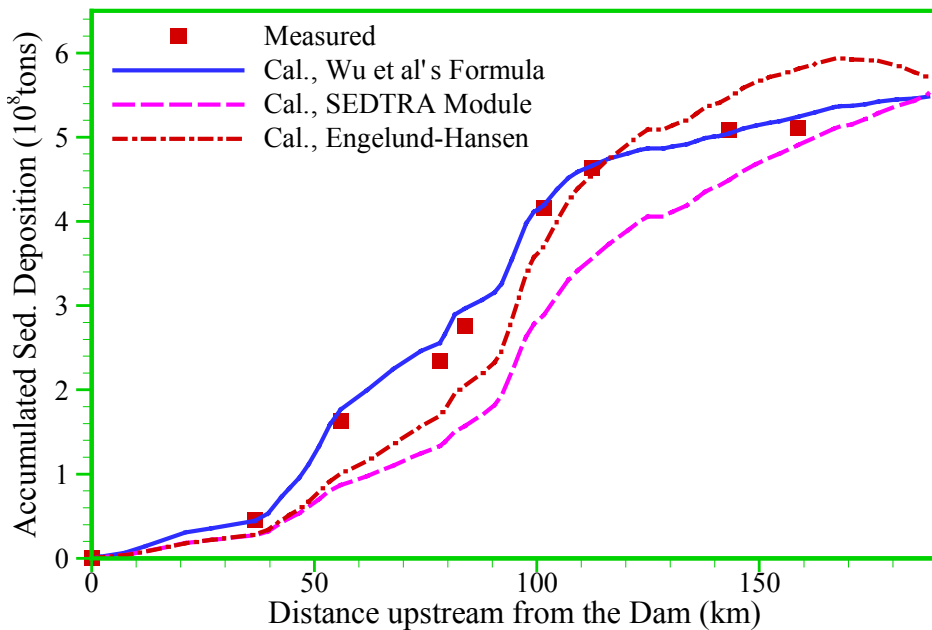


Fig. 7.27 Longitudinal Distributions of Sediment Deposition (1968-1979) in the Danjiangkou Reservoir

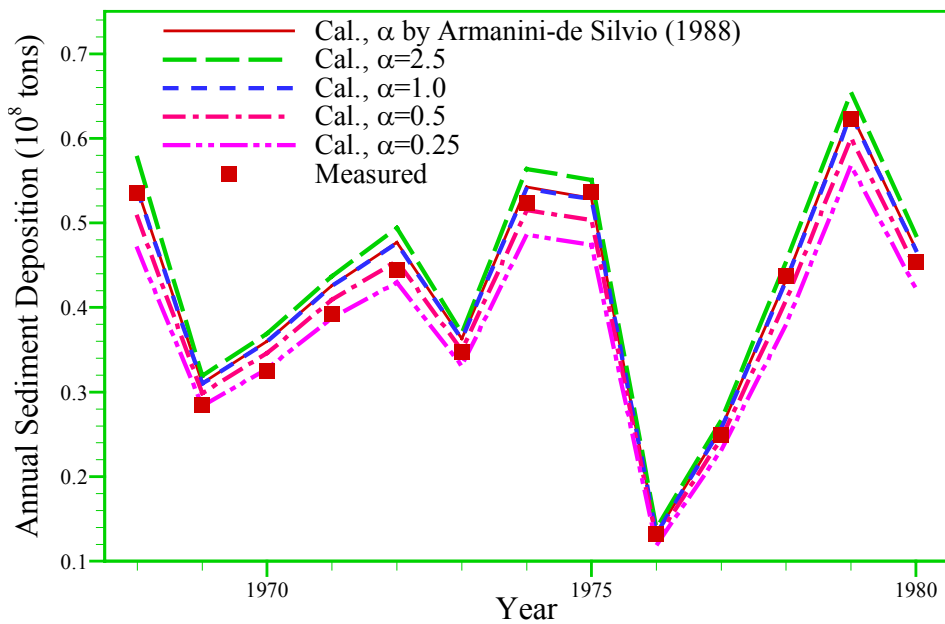


Fig. 7.28 Sensitivity of the Calculated Annual Deposition with respect to  $\alpha$

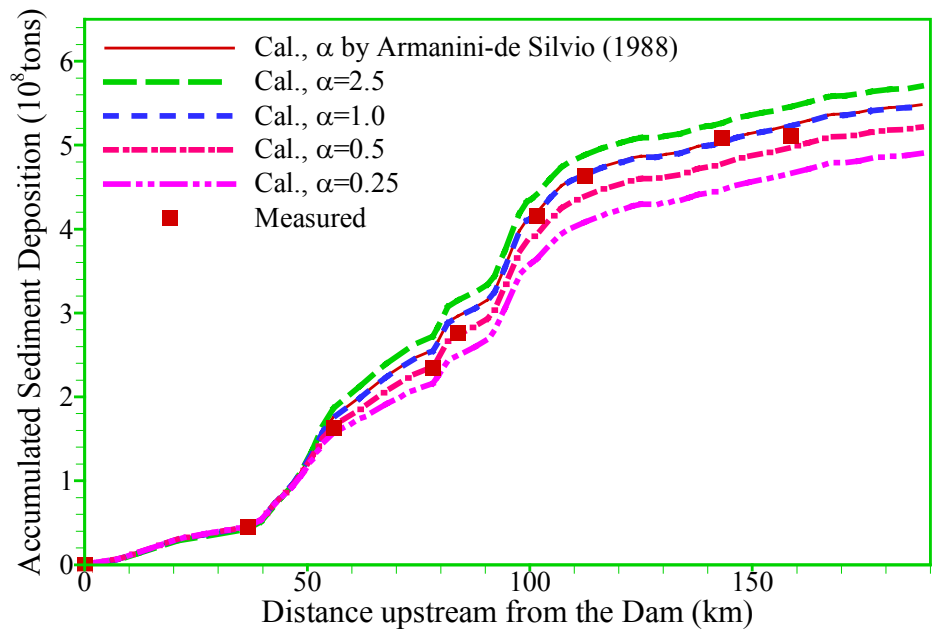


Fig. 7.29 Sensitivity of the Calculated Deposition Distribution with respect to  $\alpha$

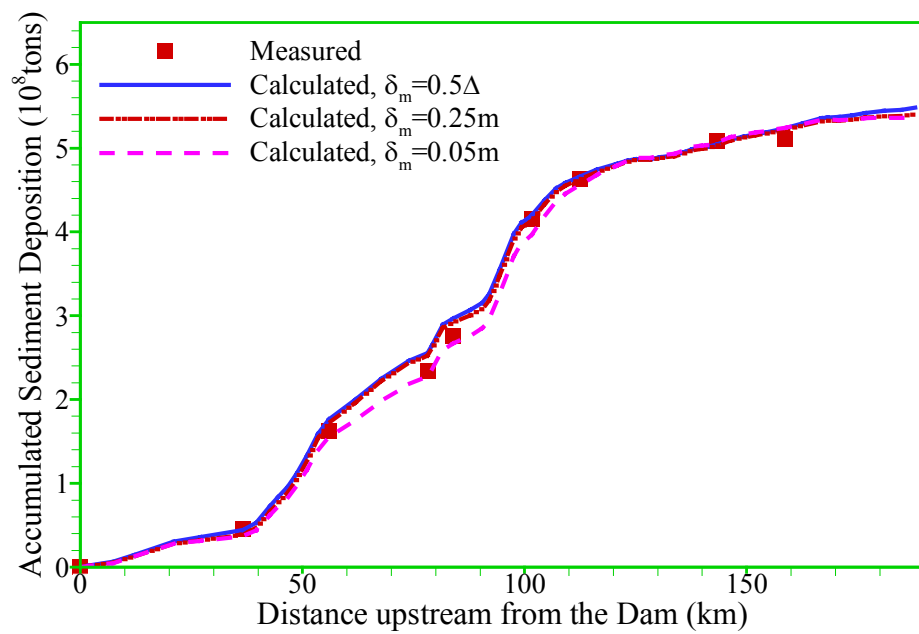


Fig. 7.30 Sensitivity of the Calculated Deposition Distribution  
with respect to Mixing Layer Thickness

### 7.4.3 Unsteady Flow and Sediment Transport in the East Fork River

The East Fork River originates in the Wind River Range of Wyoming, west of the Continental Divide and east and south of Mt. Bonneville. It was an experimental river for the study of bed load transport in 1970's. The study reach is 3.3 km in length and terminates downstream at a bed load trap constructed across the river. The general configuration of the study reach is shown in Fig. 7.31. The drainage area of the East Fork River at this bed load trap is about 500 km<sup>2</sup>. Along the study reach, the East Fork River meanders in a flood plain averaging 100m in width. During the spring runoff, diurnal fluctuations due to snowmelt are characterized by a rising stage during the morning, a peak stage at midday, and a falling stage during the afternoon. The main mode of sediment transport is bed load, and the ratio of suspended load and bed load is about 30%.

The computation domain was the 3.3km-long study reach described by 41 cross-sections, as shown in Fig. 7.31. The number shown at each cross section is the centerline distance in meters upstream of the bed load trap. The simulation period was 31 days from May 20 to June 19, 1979. The time step was 15 minutes.

Fig. 7.32 shows the comparison of the simulated and measured longitudinal water surface profiles on May 27 and June 1. In the calculation, the Manning's roughness coefficient was calibrated using the measured water surface elevation data. As shown in Fig. 7.32, the calculated longitudinal water surface profile using the calibrated Manning's coefficient agrees well with the measurement. Figs. 7.33 and 7.34 show the comparison of the calculated and measured time series of water surface elevations at the inlet and flow discharges at the outlet, respectively, which are also in good agreement with the measurements.

Fig. 7.35 compares the simulated and measured bed-material load discharges at the outlet. In the calculation, the sediment transport capacity was determined by Wu et al.'s (2000) formula. Better prediction is obtained for the low flow stage when no overbank flow occurs, while obvious deviation exists during the high flow period when there is overbank flow. Considering the difficulties in the measurement and prediction of sediment transport, the simulated results in Fig. 7.35 are generally reasonable. Other three sediment transport capacity formulas, SEDTRA module, modified Ackers and White's formula and the modified Engelund and Hansen's formula, were also tested in this case, and it was found that these three formulas significantly over-predicted the sediment discharge at the outlet.

Fig. 7.36 shows the sensitivity of the calculated sediment discharge at the outlet with respect to the non-equilibrium adaptation length of bed load. Two constant values, 20m and 200m, were given to the non-equilibrium adaptation length. It is found that less deviation exists for the low flow period while larger deviation occurs in the high flow season when the overbank flow happened. The sensitivity is insignificant.

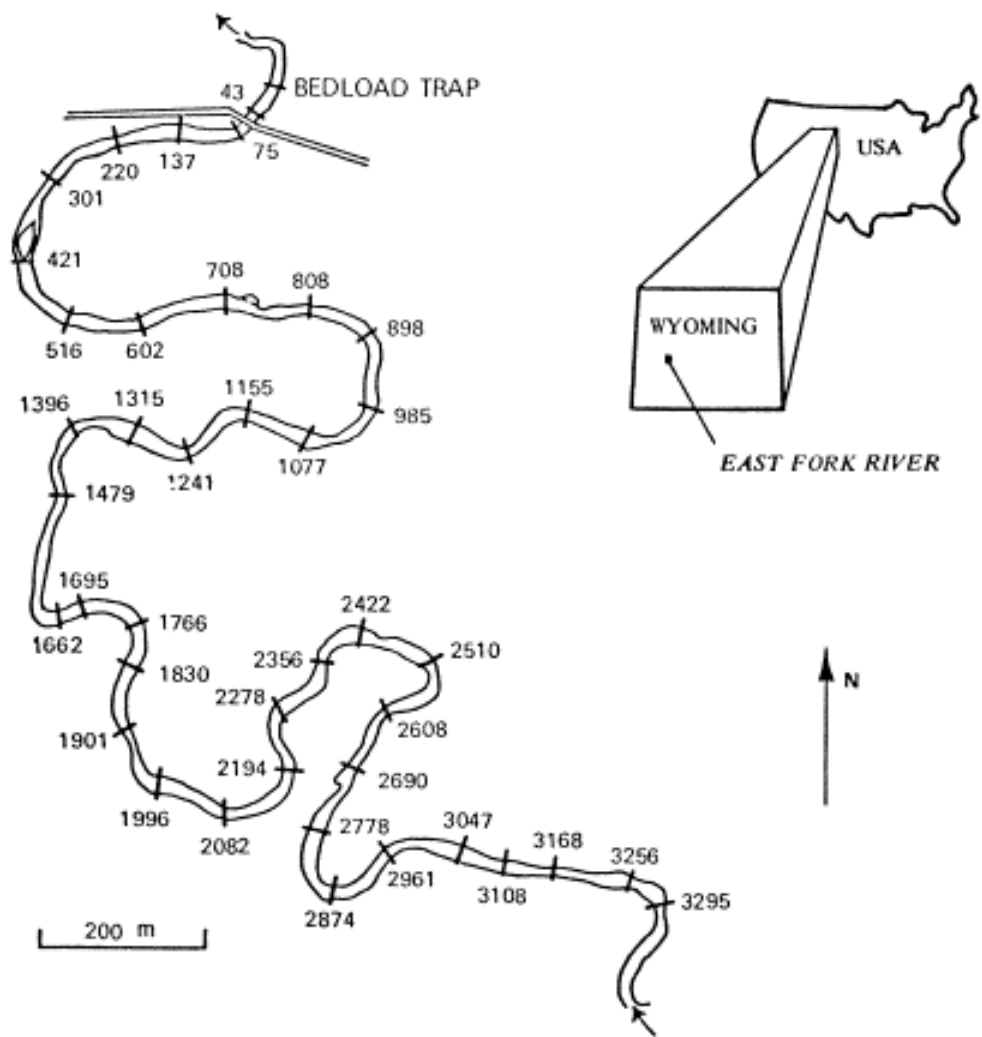


Fig. 7.31 Sketch of the Study Reach in the East Fork River  
(The numbers denote the distance (m) upstream of the bed load trap)

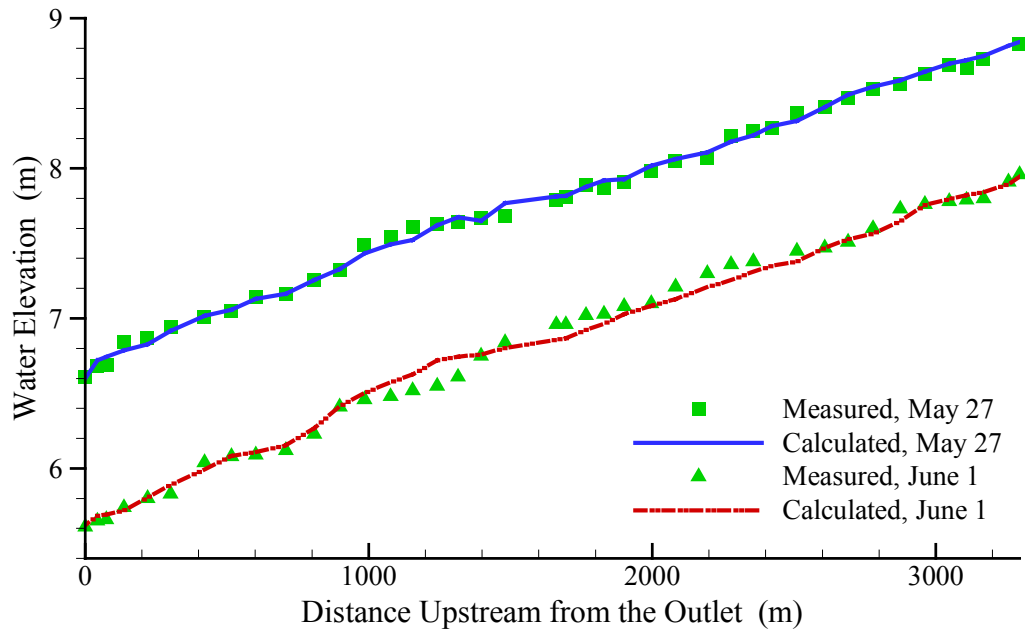


Fig. 7.32 Measured vs. Calculated Longitudinal Profiles of Water Surface

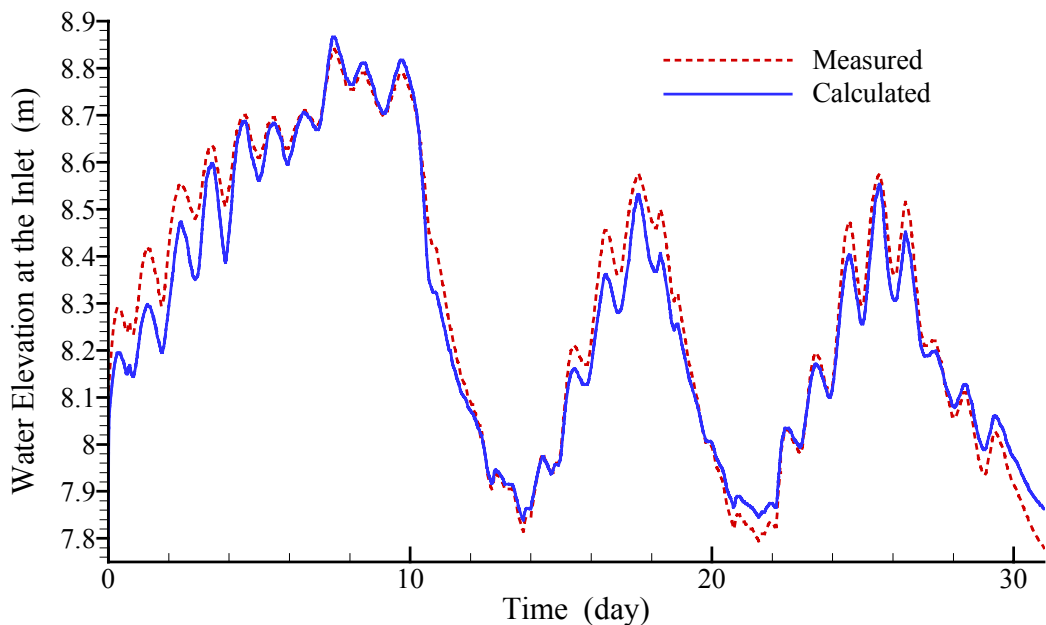


Fig. 7.33 Measured vs. Calculated Water Surface Elevations in the Inlet

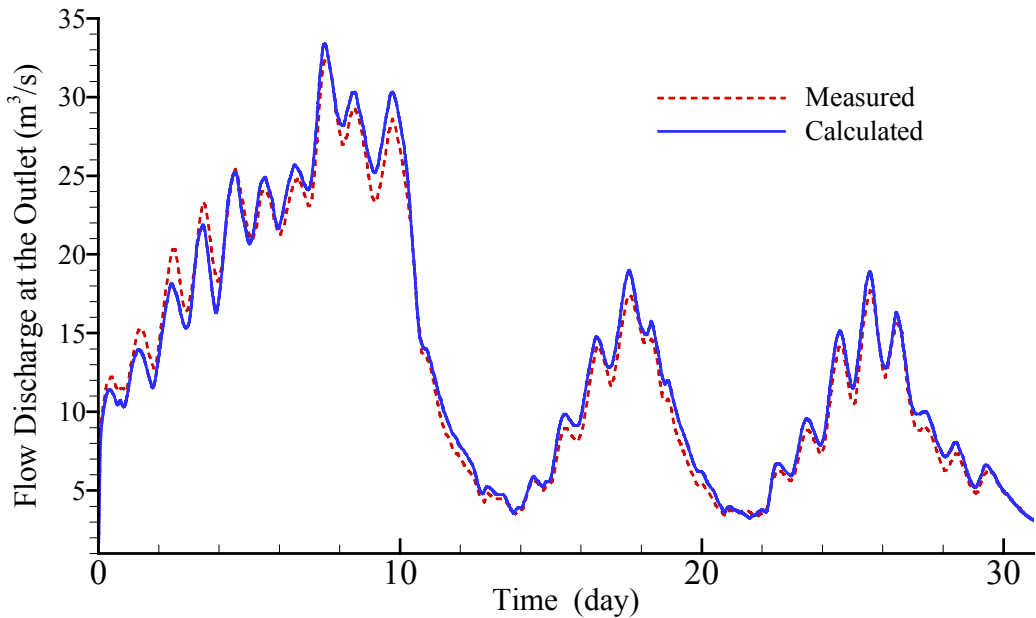


Fig. 7.34 Measured vs. Calculated Flow Discharges in the Outlet

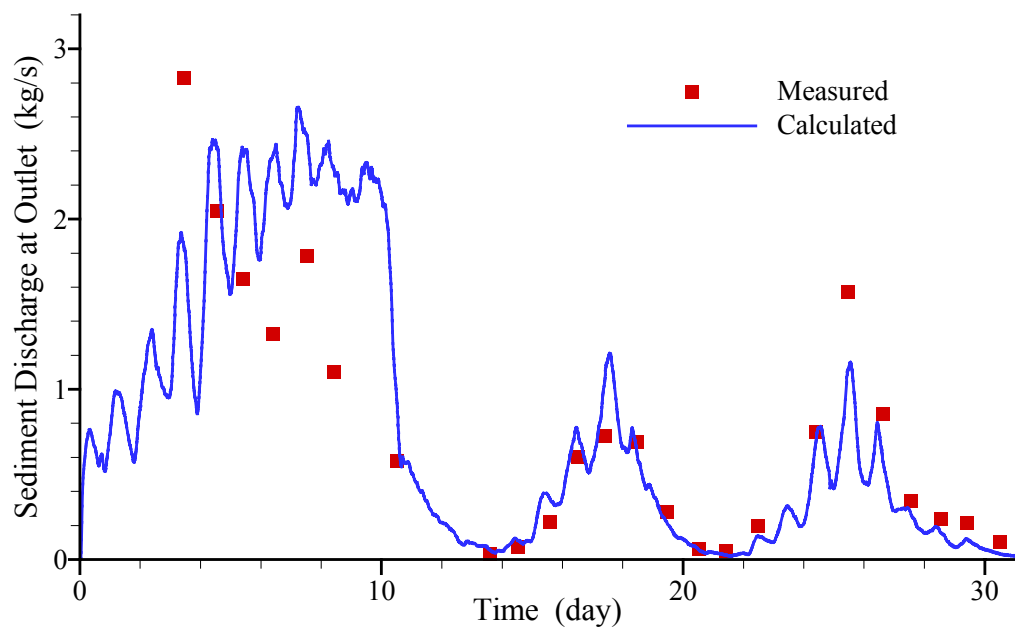


Fig. 7.35 Measured vs. Calculated Sediment Discharge at the Outlet

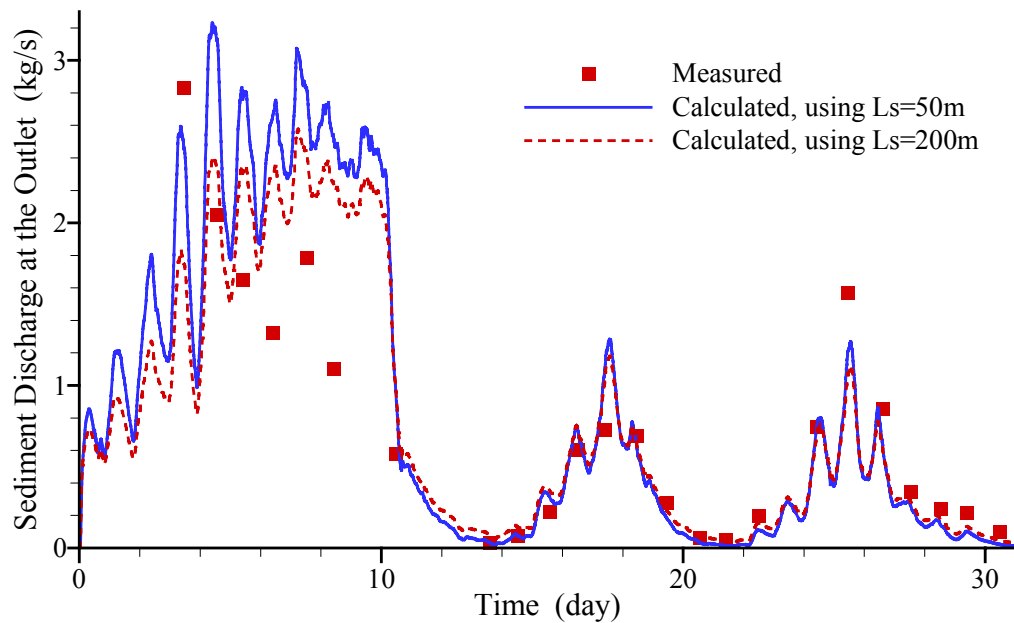


Fig. 7.36 Sensitivity of Calculated Sediment Discharge at the Outlet  
with respect to Non-Equilibrium Adaptation Length

## Chapter 8 Model Applications

### 8.1 Model Application to Goodwin Creek Watershed

#### 8.1.1 Watershed Description

The Goodwin Creek in Panola County, Mississippi, is an experimental watershed for the DEC project. The drainage area above the watershed outlet is 21.3km<sup>2</sup>. Terrain elevation ranges from 71m to 128m above mean sea level, producing an average channel slope of 0.004. The watershed is largely free of land disturbing activities with 13 percent of its total area under cultivation, 10% idle, 50% in pasture and 27% forested, according to the 1991 data (Alonso, 1997). The area exhibits an annual mean temperature of approximately 17°C, with mean monthly temperatures during 1982-1993 ranging from -0.3 to 33.7°C.

The average annual rainfall during 1982-1991 was 1460mm, and the average annual runoff at outlet was 537mm. The greatest amounts of rainfall occur during the fall and spring months of the year. Most of the channels in the watershed are ephemeral, with perennial flows occurring only in the lower reaches of the watershed. The runoff produced by storm events swiftly exits the watershed, and the discharge returns baseflow levels within one to three days.

The bank materials are mainly silt with a little of sand and gravel, and the bed materials in the channels are bimodal mixtures with sand and gravel. The sediment being transported in the channels ranges from silt (<0.062mm) to sand to gravel (<65mm). The fine materials such as silt and fine sand are mostly from upland fields and channel banks, and the coarse materials originate from gullying in some upland parts of the watershed and from bank erosion in the channels. In the low flow period, only the fine materials are transported. The coarse materials are accumulated in temporary storage in point bars and move only during large events.

Fourteen fully-instrumented flumes were constructed in the channels to control degradation of the channel bed and monitor runoff and sediment yield. The long-term measurement data of flow discharge and sediment yield in this watershed were used to validate the CCHE1D channel network model. The CCHE1D model was then applied to analyze the sediment yield budget in this watershed, and the effects of these in-stream hydraulic structures on erosion control.

#### 8.1.2 Simulation Procedures and Results

Figs. 8.1 and 8.2 show the DEM of the Goodwin Creek watershed and the subwatershed distribution created by TOPAZ from the DEM. Fig. 8.3 shows the channel network of Goodwin Creek watershed extracted by TOPAZ. Only channels of order 2 or above were

used in the computations. These channels contained ten in-stream measuring flumes and four culverts. The refined computational channel network of the Goodwin Creek, shown in Fig. 8.4, consists of 253 nodes. The measured reach lengths between measuring flumes 1 and 2 were used in the calculation in order to compare the calculated bed change with the measurement in this reach, while in other parts of this channel network the reach lengths extracted from DEM by TOPAZ were used in the calculation. The reach lengths between cross sections were between 30m and 250m. The simulation duration was 18 years from January 1978 to December 1995, with a total of 1192 storm events. The dry seasons between storms were skipped because the flow discharges in these periods were very small. The calculation time step used was 15 minutes. The runoff and sediment yield from the upland fields generated with SWAT (Bingner et al., 1997) were used as the inflow conditions for the simulation of flow and sediment transport in the channel network. Daily runoff and sediment loads were converted to triangular hydrographs and sedigraphs. The flow in channels was calculated with the dynamic wave model.

Three sediment transport capacity formulas including SEDTRA module, Wu et al's (2000) formula and the modified Engelund-Hansen formula were used, with the power index  $x$  in SEDTRA module being given a value of 0.5. The modified Ackers-White formula was also tested in this case, but it underpredicted the sediment yield and the bed changes. Therefore its results are not introduced here. The Manning's roughness coefficient was set to 0.03 on bed and 0.08-0.1 on banks and flood plains, which resulted in an overall Manning's coefficient of about 0.06 in the entire cross-section. The bed-material porosity was calculated with Komura and Simmons' (1967) formula. The bed-material mixing layer thickness was defined as half of sand dune height. The non-equilibrium adaptation length for bed load was set to 6.3 times of the average channel width for each channel link, and the non-equilibrium adaptation coefficient  $\alpha$  for suspended load is 0.001 (up to 1), but sensitivity analysis on these parameters will be introduced in the next section. Bank toe erosion and mass failure were considered, and the critical shear stress for bank toe erosion was estimated as about 4.0-4.5 Pa.

Figs. 8.5(a) and (b) show the comparison of the calculated and measured thalweg changes between flumes No.1 and No.2, from 1978 to 1988 and 1992. The results using three sediment transport capacity formulas are very close to the measurement. The bed deposition in the upstream of flume No.1 and the bed scour in the downstream of flume No.2 are well predicted by the CCHE1D model. In the transition reach between these two parts the channel bed scoured and deposited alternatively. The thalweg changes in this transition reach in the period 1978-1988 are not well reproduced but the prediction of thalweg changes between 1978 and 1992 is generally good. As a whole, the predicted bed changes are in very good agreement with the measurements.

Figs. 8.6(a), (b) and (c) show the comparison between the calculated and measured sediment yields at flumes No.1, 2 and 3. The agreements are generally good. Table 8.1 provides the detailed information on silt, sand and gravel sediment yields at flumes No.1 and 2 calculated with the CCHE1D model using three formulas. The silt and sand yields are better predicted than the gravel yield. The errors for silt and sand are less than 20%, while

the errors for gravel are much larger. This is understandable because it is usually more difficult to measure and predict the gravel transport.

Table 8.1 Cumulative Sediment Yields of Goodwin Creek Watershed in 1982-1991

Measuring Stations	Sediment Classes	Measured Sediment Yield (ton)	Calculated with CCHE1D using Capacity Formula					
			Wu et al.		Engelund-Hansen		SEDTRA	
			Yield (ton)	Error (%)	Yield (ton)	Error (%)	Yield (ton)	Error (%)
Flume No.2	Silt	145475	170987	+17.5	169333	+16.4	171724	+18.0
	Sand	63772	52092	-18.3	52024	-18.4	50957	-20.1
	Gravel	13837	7767	-43.9	8499	-38.6	10800	-21.9
	Total	223084	250944	+12.5	250076	+12.1	251882	+12.9
Flume No.1	Silt	227847	242442	+6.4	241175	+5.8	246392	+8.1
	Sand	73493	62694	-14.7	63499	-13.6	64414	-12.4
	Gravel	6918	12686	+83.4	14174	+104.9	22635	+227.2
	Total	308259	334772	+8.6	334705	+8.6	345889	+12.2

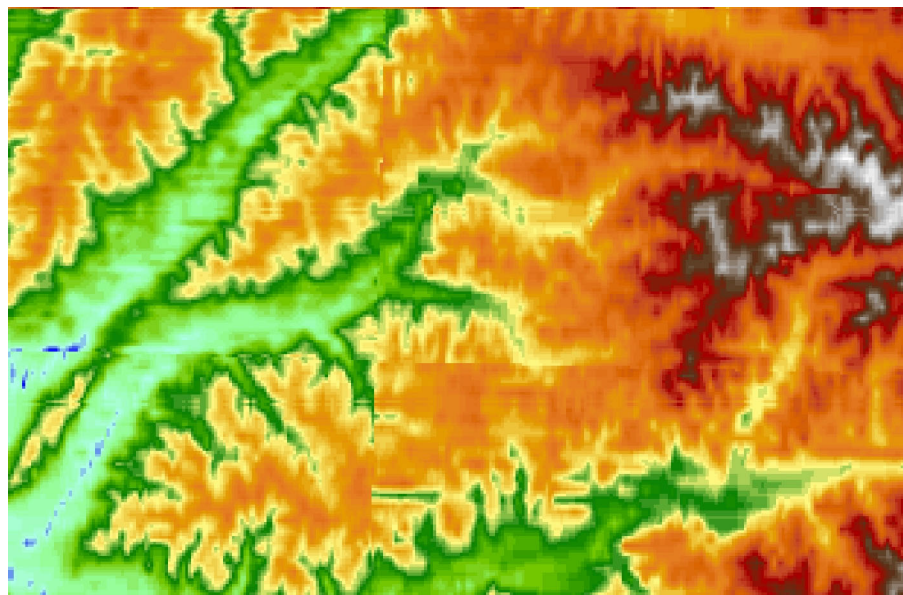


Fig. 8.1 DEM of Goodwin Greek Watershed

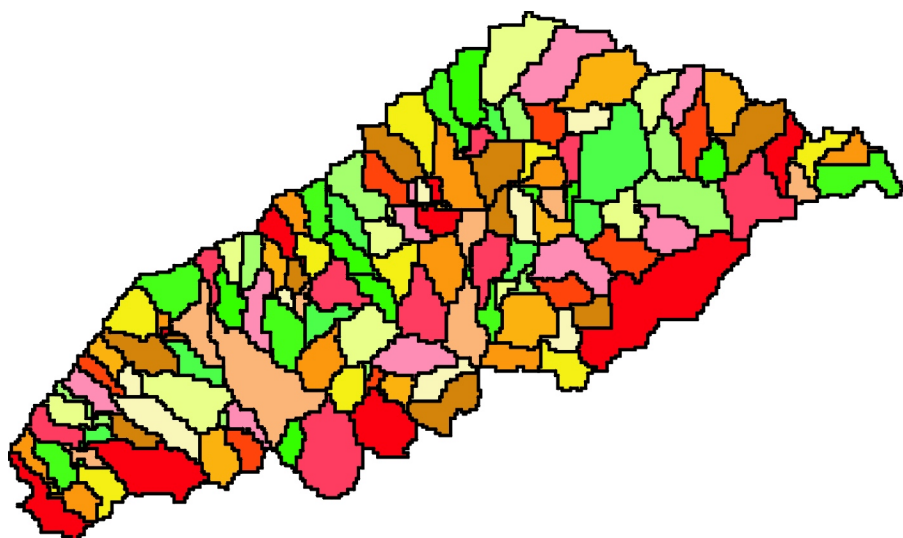


Fig. 8.2 Subwatersheds in Goodwin Greek

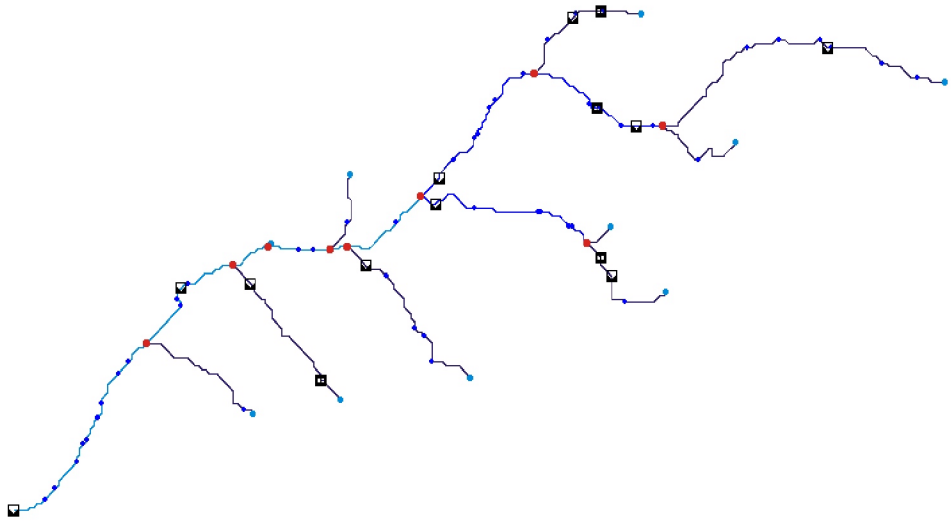


Fig. 8.3 Extracted Channel Network with Hydraulic Structures  
in Goodwin Creek Watershed

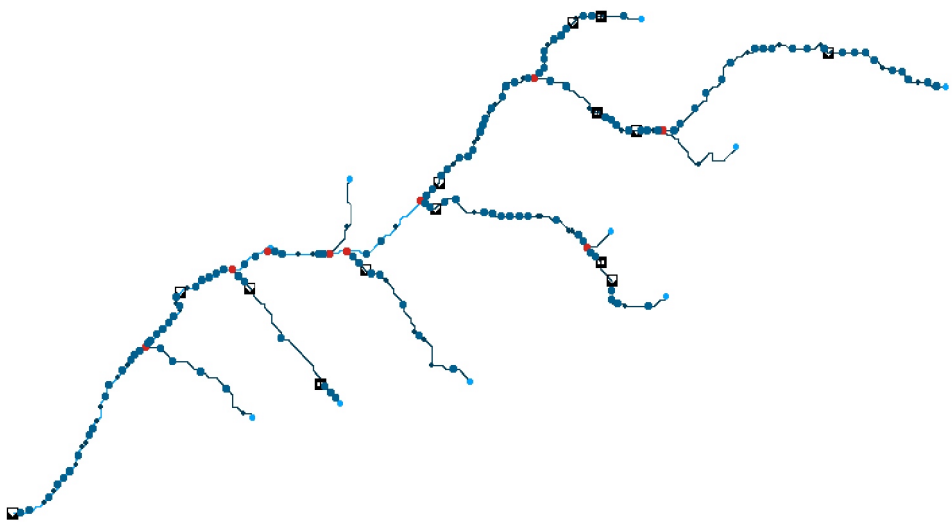


Fig. 8.4 Refined Computational Grid (253 Nodes) in Goodwin Creek

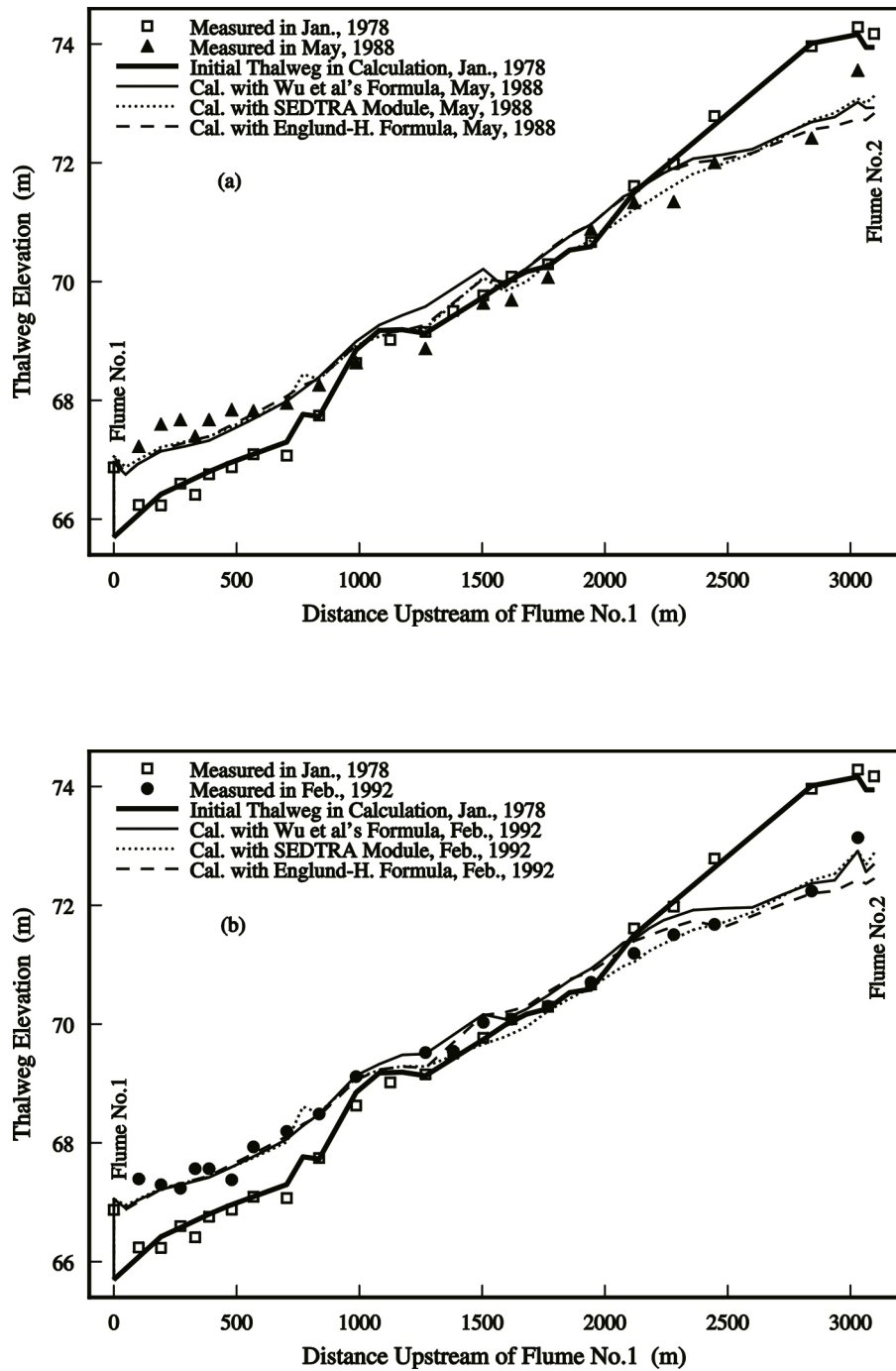


Fig. 8.5 Thalweg Changes between Flumes No. 1 and No. 2 of Goodwin Creek  
 (a). 1978-1988; (b). 1978-1992

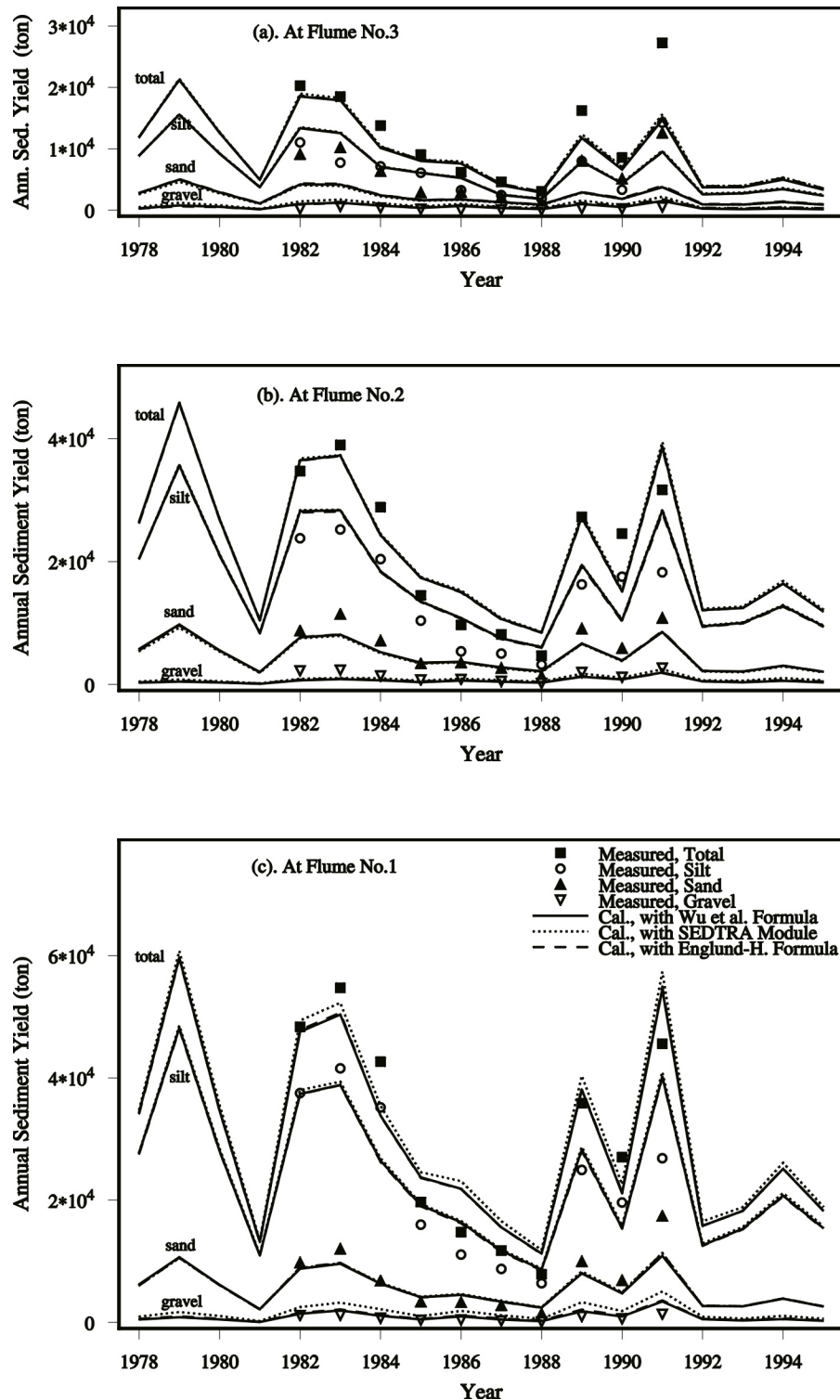


Fig. 8.6 Annual Sediment Yields at Flumes No. 1, 2 and 3 of Goodwin Creek

### 8.1.3 Sensitivity Analysis

#### *Sensitivity to Non-equilibrium Adaptation Length*

One of the most important parameters in the CCHE1D sediment transport model is the non-equilibrium adaptation length. Its sensitivity was studied in previous test cases in Chapter 7 and some encouraging results were obtained. Goodwin Creek is a very good natural stream test case for the study of the model sensitivity to this parameter, because sediment in the Goodwin Creek varies from silt to sand to gravel, and is transported as both bed load and suspended load. Here, the non-equilibrium adaptation coefficient  $\alpha$ , which is used to calculate the non-equilibrium adaptation length for suspended load, was given values of 0.001, 0.01, 0.1 and 1.0, while other parameters were kept the same. The calculated thalweg changes are shown in Fig. 8.7(a). In the reach upstream of flume No. 1, the calculated deposition trends are very close even though  $\alpha$  was given a wide range of values. However, in the reach downstream of flume No. 2, the calculated bed profiles after scour are more sensitive to  $\alpha$ . When  $\alpha=0.001$  and 0.01, the bed profiles are very smooth, but when  $\alpha=0.1$  and 1.0, some pools and shoals are generated numerically. It should be mentioned that this kind of geomorphic structures are not the result of node-to-node oscillations. The reasons for their occurrence may be attributed to the natural expansion and contraction of channel width, the simplified representation of cross section by only 4 points in the main channel, and the lack of detailed information on the bed-material gradation under the bed surface. Despite the presence of these pools and shoals, the average bed slopes calculated with four different values of  $\alpha$  are very close.

Fig. 8.7(b) shows the sensitivity of the calculated sediment yields at the watershed outlet to  $\alpha$ . Table 8.2 provides the detailed comparison of the calculated silt, sand and gravel yields using different  $\alpha$ . As  $\alpha$  increases from 0.001 to 1.0, the gravel yield increases 27%, the silt yield decreases 9%, and the sand yield decreases first and then increases with a net growth of 8%. The total sediment yield slightly decreases 5% as a result. A conclusion is therefore obtained that the calculated sediment yields at the watershed outlet are not significantly sensitive to the values of  $\alpha$ . This conclusion is very encouraging. However, it should be mentioned that the sediment yield in Goodwin Creek are mainly from upland field and channel banks, and therefore the sensitivity to  $\alpha$  in other cases without serious bank erosion and upland erosion may behave differently, which was tested in Section 7.4.2.

Because the actual value of the non-equilibrium adaptation length for bed-material load is the maximum of the non-equilibrium adaptation lengths for bed load and suspended load, the sensitivity to the non-equilibrium adaptation length for bed load  $L_{s,b}$  is also an important issue. In the above analysis of sensitivity to  $\alpha$ , the  $L_{s,b}$  is fixed as the alternate bar length. Now  $\alpha$  is fixed at 0.001, and the  $L_{s,b}$  is given values of 20m and 200m. The sensitivity to  $L_{s,b}$  is shown in Fig. 8.8 and Table 8.3. Some small difference is found in the reach downstream of flume No. 2, where scour occurs. The bed profiles in the reach with deposition and the sediment yields at watershed outlet are insensitive to  $L_{s,b}$ . As  $L_{s,b}$  increases from 20m to 200m, silt, sand and gravel yields increase 1.0%, 8.6% and 20.5%, respectively, and the total sediment yield decreases 3.1%.

Table 8.2 Sensitivity of the Calculated Sediment Yields at Watershed Outlet  
to Non-equilibrium Adaptation Coefficient  $\alpha$  for suspended Load

Sediment Classes	Calculated Average Annual Sediment Yields			
	$\alpha=0.001$	$\alpha=0.01$	$\alpha=0.1$	$\alpha=1.0$
Silt ( $\text{m}^3/\text{year}$ )	8834	8595	8258	8044
Sand ( $\text{m}^3/\text{year}$ )	2089	2011	2088	2256
Gravel ( $\text{m}^3/\text{year}$ )	338	389	421	428
Total ( $\text{m}^3/\text{year}$ )	11261	10995	10767	10728

Table 8.3 Sensitivity of the Calculated Sediment Yields at Watershed Outlet  
to Non-equilibrium Adaptation Length  $L_{s,b}$  for Bed Load

Sediment Classes	Calculated Average Annual Sediment Yields		
	$L_{s,b}=200\text{m}$	$L_{s,b}=6.3\text{B}$	$L_{s,b}=20\text{m}$
Silt ( $\text{m}^3/\text{year}$ )	8881	8834	8796
Sand ( $\text{m}^3/\text{year}$ )	2167	2089	1981
Gravel ( $\text{m}^3/\text{year}$ )	381	338	303
Total ( $\text{m}^3/\text{year}$ )	11429	11261	11080

### ***Sensitivity to Mixing Layer Thickness of Bed Material***

The mixing layer thickness is directly related to the calculation of bed-material gradation, which is very important to the whole simulation. Its sensitivity was tested in previous cases of Sections 7.3 and 7.4 and it has been found that the mixing layer thickness is more important in erosion cases than in deposition cases. In the calculation of the Goodwin Creek case introduced in Section 8.1.2, the mixing layer thickness was defined as half the sand-dune height, which should vary with flow strength and sediment properties. For comparison, two constant values of 0.01m and 0.1m were given to the mixing layer thickness, and then the simulations were re-conducted with other conditions and parameters being the same as in Section 8.1.2. The results are shown in Fig. 8.9 and Table 8.4. It is found that a small difference exists in the channel thalwegs downstream of flume No. 2, where bed scour occurs. The channel thalwegs upstream of flume No. 1 with deposition and the sediment yields at watershed outlet are insensitive to the mixing layer thickness. As the mixing layer thickness increases from 0.01m to 0.1m, the silt yield decreases 1.1%, the sand yield decreases 4.4%, and the gravel increases 17.6%, resulting in a 1.2% decrease for the total sediment yield.

Table 8.4 Sensitivity of the Calculated Sediment Yields at Watershed Outlet  
to Mixing Layer Thickness

Sediment Classes	Calculated Average Annual Sediment Yields		
	$\delta=0.01\text{m}$	$\delta=0.1\text{m}$	$\delta=0.5\Delta$
Silt ( $\text{m}^3/\text{year}$ )	8934	8840	8834
Sand ( $\text{m}^3/\text{year}$ )	2207	2110	2089
Gravel ( $\text{m}^3/\text{year}$ )	306	360	338
Total ( $\text{m}^3/\text{year}$ )	11447	11310	11261

### ***Sensitivity to Computational Time Step***

The sensitivity of the computed results to the time step  $\Delta t$  was analyzed by using three time steps of 5min, 15min and 30min. Differences in the calculated bed profiles are very small (see Fig. 8.10). As the time step  $\Delta t$  changes from 5min to 30min, the differences in silt, sand and gravel yields and the total sediment yields at watershed outlet are less than 2%, shown in Table 8.5. That means the computed results are not sensitive to the time step used. However, the time step can not be too large because the durations of storm events in the Goodwin Creek watershed are about one day. If too large time step is used, the accuracy is reduced and also numerical instability may occur.

Table 8.5 Sensitivity of the Calculated Sediment Yields at Watershed Outlet  
to Computational Time Step \Delta t

Sediment Classes	Calculated Average Annual Sediment Yields		
	$\Delta t=5\text{min}$	$\Delta t=15\text{min}$	$\Delta t=30\text{min}$
Silt ( $\text{m}^3/\text{year}$ )	8856	8834	8809
Sand ( $\text{m}^3/\text{year}$ )	2099	2089	2075
Gravel ( $\text{m}^3/\text{year}$ )	336	338	331
Total ( $\text{m}^3/\text{year}$ )	11291	11261	11215

### ***Sensitivity to Computational Grid***

The sensitivity to computational grid was analyzed by using two different grids in the simulation of the Goodwin Creek watershed. One grid was coarse, with 129 nodes directly extracted from DEM by TOPAZ, shown in Fig. 8.3. The second grid was finer, generated from the coarse grid by using the auto-generation option on the interface. This fine grid was used in the simulation of Section 8.1.2 and in the previous sensitivity analysis, and it had 253 nodes, shown in Fig. 8.4. The average grid length of the fine grid was nearly half the average grid length of the coarse grid. The simulation results are shown in Fig. 8.11 and

Table 8.6. The calculated bed profiles are very close, and so are the calculated sediment yields at the watershed outlet. The relative difference in sediment yields is less than 6%.

Table 8.6 Sensitivity of the Calculated Sediment Yields at Watershed Outlet  
to Computational Grid

Sediment Classes	Calculated Average Annual Sediment Yields		
	with Fine Grid	with Coarse Grid	Deviation
	(m <sup>3</sup> /year)	(m <sup>3</sup> /year)	(%)
Silt	8834	8834	0.0
Sand	2089	2008	-3.9
Gravel	338	318	-5.9
Total	11261	11160	-0.9

#### ***Difference in Sediment Results Using Dynamic and Diffusive Wave Models***

The differences between the dynamic and diffusive wave models in cases of impoundment backwater, channel contraction, etc., were tested in Section 7.1. Significant differences existed when the channel geometries varied rapidly, but beyond these rapidly varied regions both models provided very close results. In the Goodwin Creek case, flow patterns calculated with both flow models were very close, because the channel geometry did not vary rapidly and the influence of those in-stream hydraulic structures was very small. A further test was set up to show the difference in sediment results due to using the dynamic and diffusive wave models in the Goodwin Creek watershed. All the conditions and parameters used were the same as those in Section 8.1.2 except that the flow was simulated using either the dynamic wave model or the diffusive wave model. It was found that the calculated bed profiles and sediment yields from both flow models were so close that the differences could not be shown by figures. Shown in Table 8.7, the difference in the calculated sediment yields at watershed outlet is less than 3%.

Table 8.7 Calculated Sediment Yields at Watershed Outlet  
Using Dynamic/Diffusive Wave Models

Sediment Classes	Calculated Average Annual Sediment Yields		
	Dynamic Wave Model	Diffusive Wave Model	Deviation
	(m <sup>3</sup> /year)	(m <sup>3</sup> /year)	(%)
Silt	8834	8828	-0.07
Sand	2089	2082	-0.33
Gravel	338	348	+2.96
Total	11261	11258	-0.03

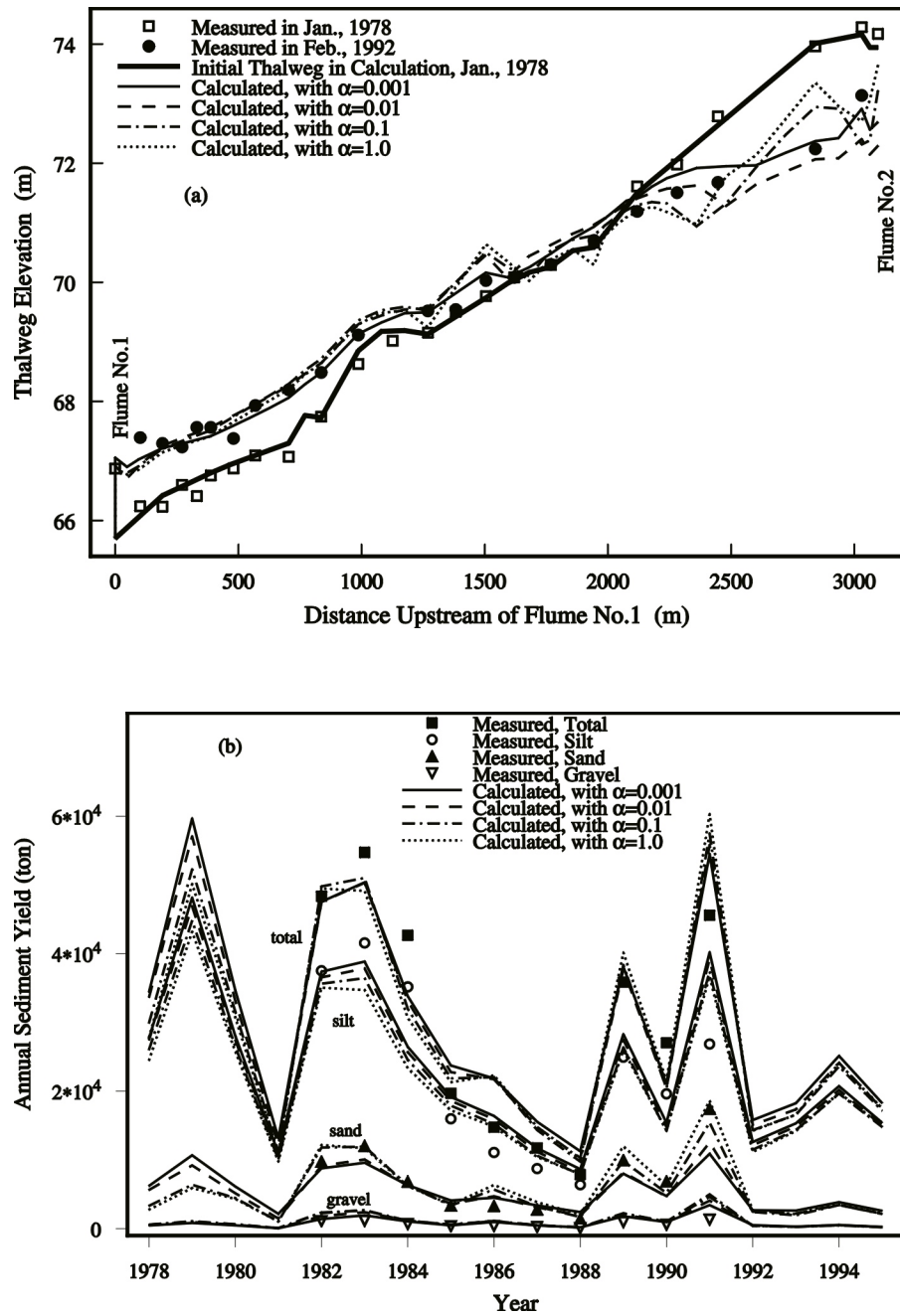


Fig. 8.7 Sensitivity to Non-equilibrium Adaptation Coefficient  $\alpha$

(a). Thalweg Changes between Flumes No. 1 and 2

(b). Sediment Yields at Watershed Outlet

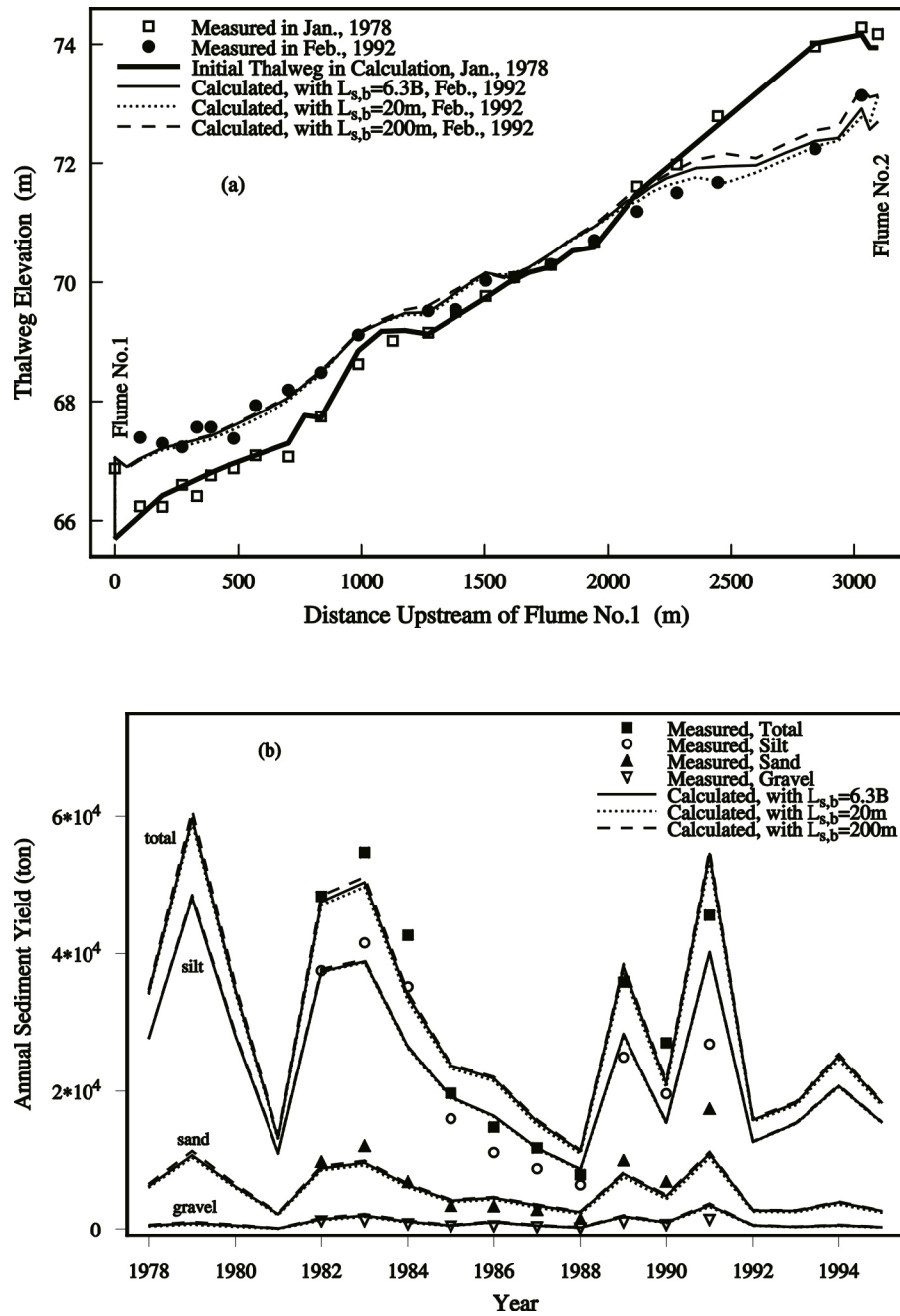


Fig. 8.8 Sensitivity to Non-equilibrium Adaptation Length  $L_{s,b}$

- Thalweg Changes between Flumes No. 1 and 2
- Sediment Yields at Watershed Outlet

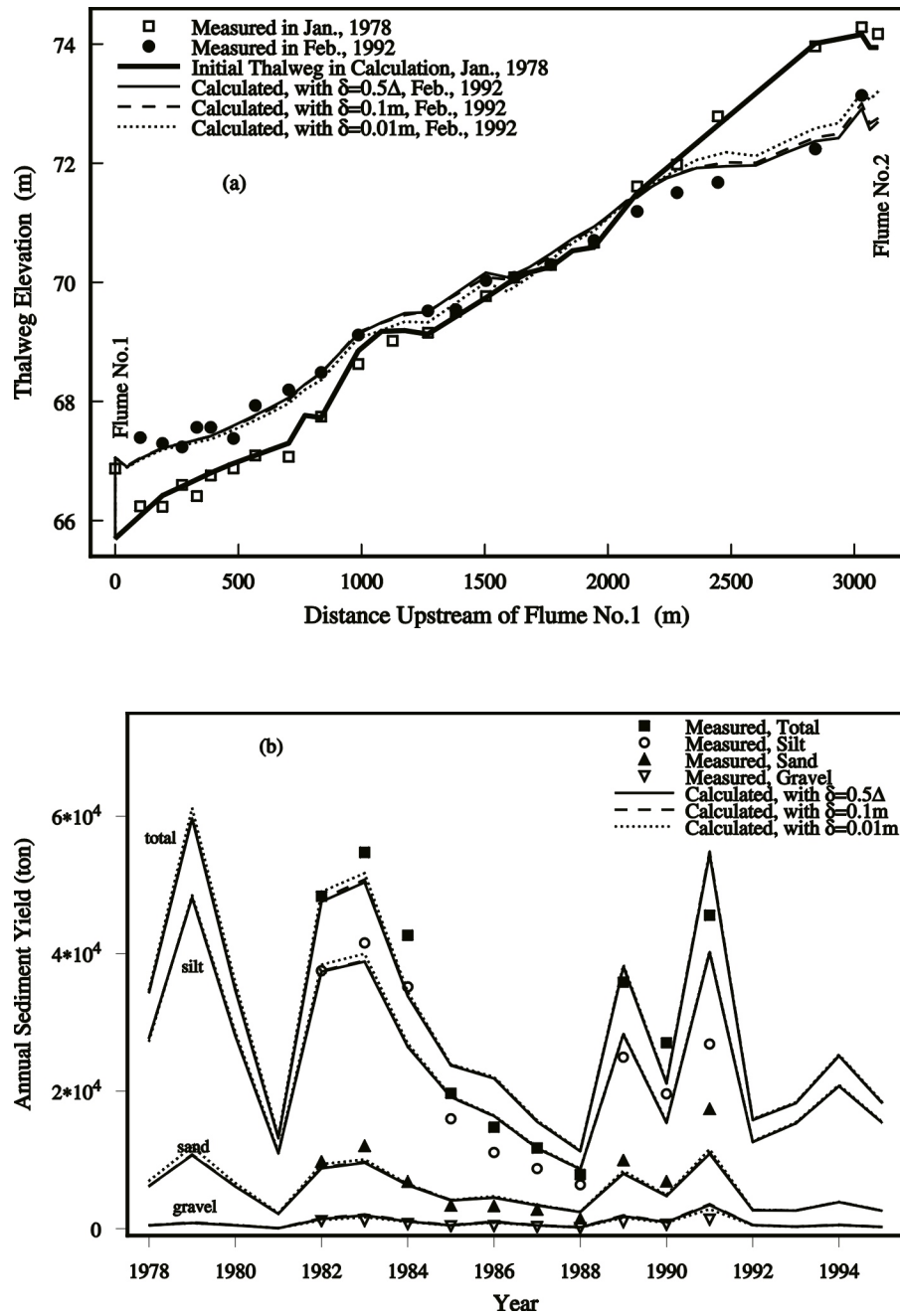


Fig. 8.9 Sensitivity to Mixing Layer Thickness of Bed Material

(a). Thalweg Changes between Flumes No.1 and 2

(b). Sediment Yield at Watershed Outlet

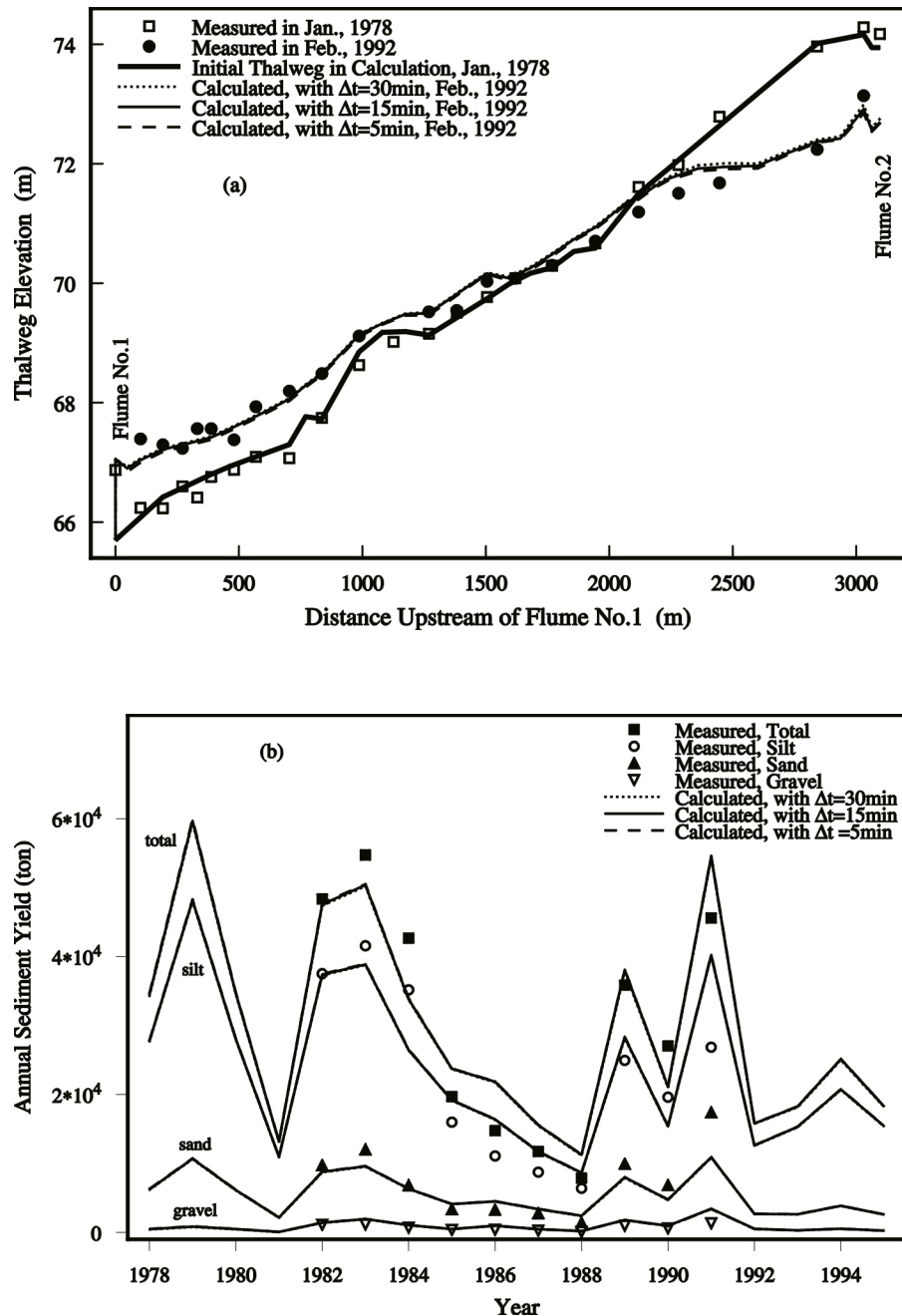


Fig. 8.10 Sensitivity to Computational Time Step  $\Delta t$   
(a). Thalweg Changes between Flumes No.1 and 2  
(b). Sediment Yield at Watershed Outlet

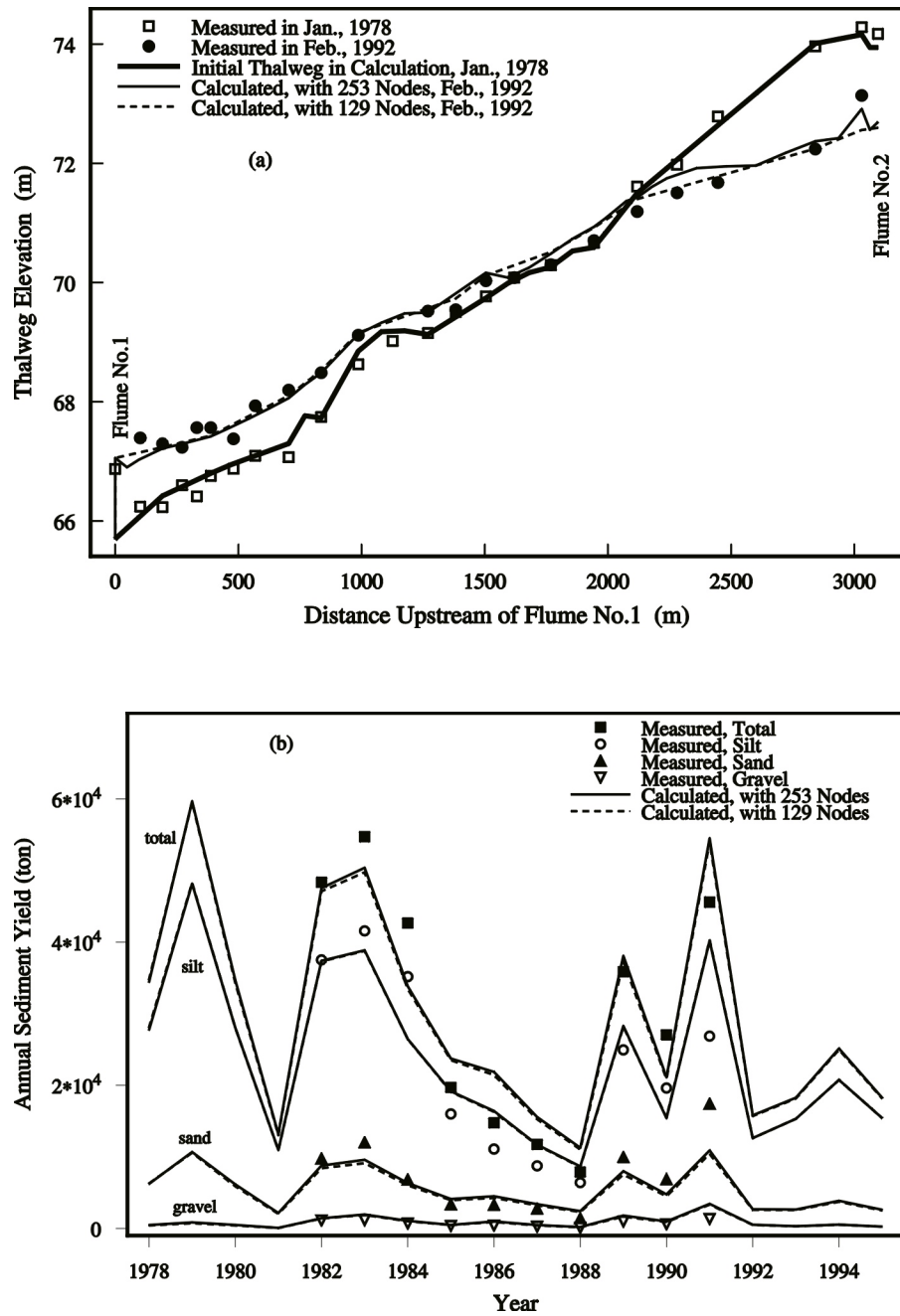


Fig. 8.11 Sensitivity to Computational Grid  
 (a). Thalweg Changes between Flumes No.1 and 2  
 (b). Sediment Yield at Watershed Outlet

### 8.1.4 Effects of Hydraulic Structures on Erosion Control

The in-stream measuring flumes in the Goodwin Creek watershed were designed for two purposes: measuring the runoff and sediment transport, and stabilizing the channel bed. Their effect on erosion control can be easily studied by numerical models. Since the CCHE1D model had been validated using the measured data, the simulation was re-conducted using the same conditions and parameters as in Section 8.1.2 except that the in-stream 10 measuring flumes and 4 culverts were assumed not to exist. Fig. 8.12 shows the thalweg changes between flumes No.1 and No.2 during 1978-1992 with and without hydraulic structures. In the case without measuring flumes, the changes in the channel thalwegs in the reach upstream of flume No. 1 between January 1978 and February 1992 were very small. With the construction of measuring flume No. 1, deposition occurred in this reach due to the backwater effect created by the structure. In the reach downstream of flume No.2, the bed eroded in the natural conditions without structures' influence, and the erosion increased when the structures appeared. The reasons are that the backwater of flume No.1 did not affect this reach, and a part of coarse sediment was detained by other hydraulic structures in the upstream reaches of the watershed.

Table 8.8 summarizes the comparison between the calculated average annual sediment yields during 1978-1995 with and without the in-stream hydraulic structures. It was found that the structures had a significant effect on the sediment yield from the channel bed. The gravel from the channel bed was reduced by 78% and the sand from bed by 52%. These hydraulic structures significantly enhanced the channel bed stability.

However, the reduction of bank erosion by these in-stream hydraulic structures was only 12% as shown in Table 8.8, which means that the in-stream hydraulic structures did not significantly enhance the stability of the channel banks. The reason may be that the heights of these measuring flumes were very low and the flow strength was not reduced enough to control the bank erosion. Other kinds of grade control structures such as low and high drop structures, and bank protection measures are needed to reduce the bank erosion in incised channels like those of Goodwin Creek. In addition, the sediment yield from upland fields is also a large part of the total sediment yield at watershed outlet. The erosion control in upland fields is also one of the key measures in a comprehensive plan for erosion control.

Table 8.8 Reduction of Sediment Yields by Hydraulic Structures in Goodwin Creek

Sediment	Sources	Calculated Average Annual Sediment Yields (1978-95)		Reduction Ratio (%)
		Without Structures (m <sup>3</sup> /year)	With Structures (m <sup>3</sup> /year)	
Silt	Upland banks bed	5270 4054 0	5270 3574 -11*	0.0 -11.8 --
	Sum	9324	8833	-5.3
Sand	Upland banks bed	688 1278 613	688 1109 292	0.0 -13.2 -52.4
	Sum	2579	2089	-19.0
Gravel	Upland banks bed	0.0 261 493	0.0 229 109	0.0 -12.3 -77.9
	Sum	754	338	-55.2
Total	Upland banks bed	5958 5593 1106	5958 4912 390	0.0 -12.2 -64.7
	Sum	12657	11260	-11.0

\*: Deposit in the neighborhood of hydraulic structures.

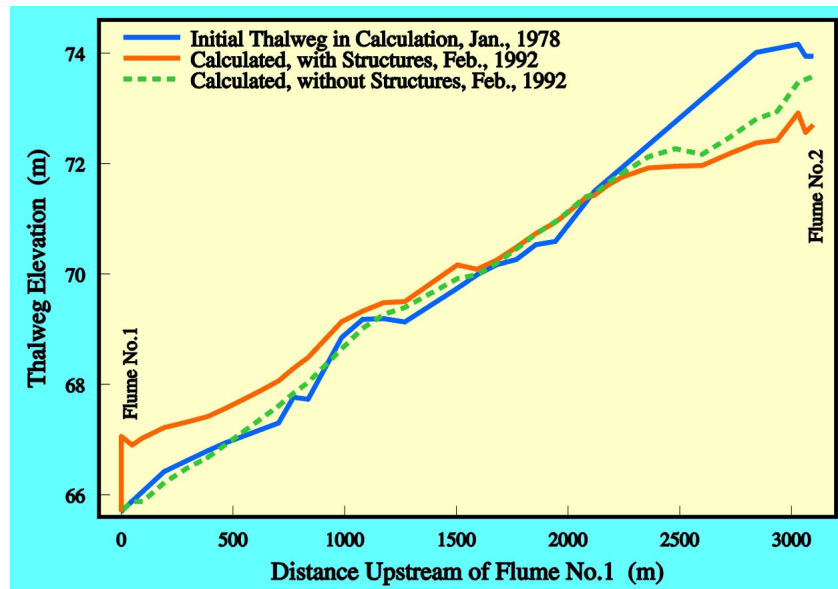


Fig. 8.12 Thalweg Changes between Flumes No. 1 and 2 in Goodwin Creek with and without Hydraulic Structures

## 8.2 Model Application to the Pa-Chang River

### 8.2.1 Case Description

The Pa-Chang River is another main river in south Taiwan (Fig. 7.21). It is 80.86km long, with a drainage basin of 474.74 km<sup>2</sup>. The average annual rainfall is 2277.4 mm, and the average annual runoff is 744.73 million m<sup>3</sup>. The study reach is 36.1 km long, whose outlet is located at the Yi-Chu Station (15.9 km upstream of the river estuary). The channel slope in the lower part of this study reach is gentle but it is very steep in the upper part. The maximum channel slope is about 1/20. Serious erosion and flooding exist in this region because of enormous rainfall and steep channels. In recent years, the Taiwan's government has paid more and more attention to the prevention and mitigation of flood and sediment erosion. A series of measurements of flow discharge, water surface elevation, bed topography, etc. were conducted during 1995-1998, which were used to test and calibrate the CCHE1D channel network model. The calibrated CCHE1D model was then applied to analyze the effectiveness of the installed and planned channel stabilization structures in this river.

### 8.2.2 Flood and Sediment Routing in the Pa-Chang River

In the calibration, 77 cross-sections were used to represent the study reach, with an average length of computational element of 475.5 m. Inflow boundary conditions were specified at the Station No. 100, which is the inlet of the study reach. The inflow discharge was calculated from the upstream Ren-Yi-Tan Dam. The inflow sediment discharge was estimated at Station No. 100 by using Yang's formula, and was represented by a curve of flow discharge and sediment discharge,  $Q_s=14.014Q^{0.8014}$ . Here, the sediment discharge  $Q_s$  is given in tons/day, and the flow discharge  $Q$  is in m<sup>3</sup>/s. An open boundary condition was specified at the outlet. Eight tributaries were not part of the current simulation but their flow and sediment were considered as side inflows to the main channel. The inflow discharge from these eight tributaries were estimated from the measured flow discharges at the Jun-Hui Bridge and Yi-Chu Station according to the drainage area and rainfall at the subbasin of each tributary. The cross-section geometry measured in 1995 was used as the initial channel topography. The bed-material size distribution measured in 1987 was used as the initial condition, because this set of size distribution data was more complete. The Manning's roughness coefficient for the design of the channel was used here, except that the Manning's coefficient around the Jun-Hui Bridge was increased to account for the effects of this bridge and a tributary. Because supercritical and critical flows occur in several cross-sections, the hybrid dynamic/diffusive wave model was adopted in this case. The computation time step was 2.5 minutes.

Figs. 8.13 and 8.14 show the comparison of the measured and simulated flow discharges and water stages at the Jun-Hui Bridge Station during 1995-1998. The flow discharge is

predicted very well by the CCHE1D model. The trend of the simulated water stage is also in reasonably good agreement with the measurement. Some deviations may be due to the dredging work around this bridge during this period.

Fig. 8.15 shows the comparison between the calculated and measured thalweg changes from 1995 to 1998. In order to avoid the influence of the uncertainty in the inflow sediment discharge and size distribution from the eight tributaries, only the thalweg changes upstream of the first tributary confluence are presented in Fig. 8.15. The numerical simulation was conducted using the CCHE1D model with three sediment transport capacity formulas: SEDTRA module (Garbrach et al, 1995), Wu, Wang and Jia's formula (2000) and the modified Engelund and Hansen's formula (see Wu and Vieira, 2000). The thalweg changes simulated by the CCHE1D model are very close to the thalweg change measured during this period. The large erosion in the upper part of the study reach is well reproduced, while the deposition in the reach from distance 46km to distance 49.8km is qualitatively predicted. The simulation results obtained with three different sediment transport capacity formulas are very close to each other, which is a positive indicator of the predictive capability of the model.

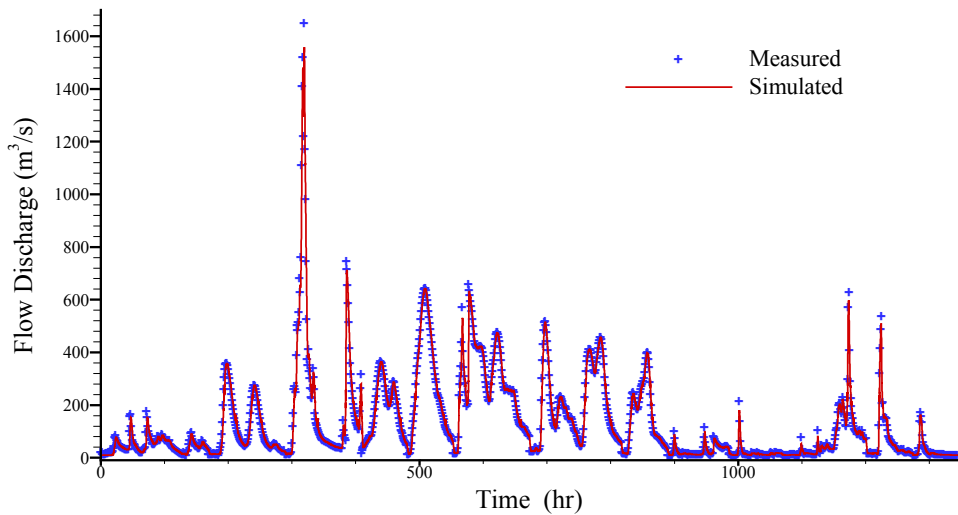


Fig. 8.13 Measured vs. Calculated Flow Discharges at Jun-Hui Bridge of Pa-Chang River in 1995-1998

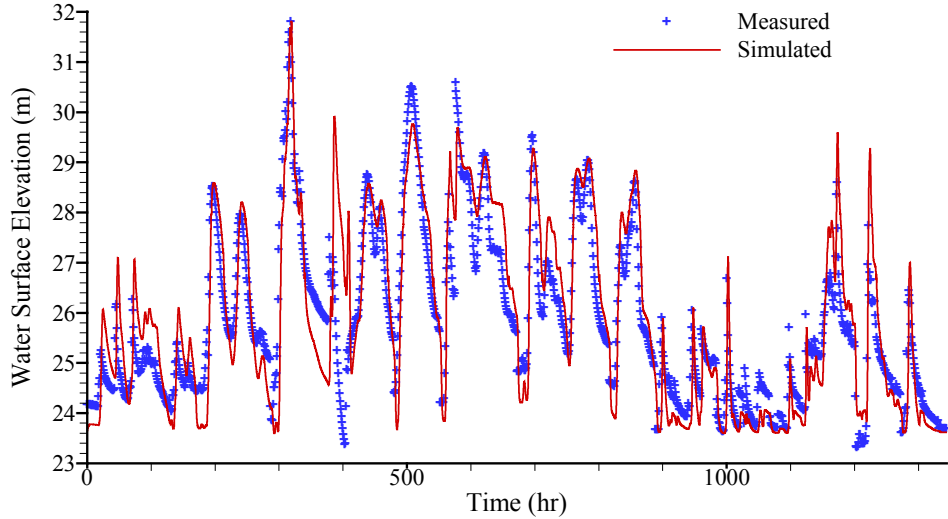


Fig. 8.14 Measured vs. Calculated Water Elevations at Jun-Hui Bridge of Pa-Chang River in 1995-1998

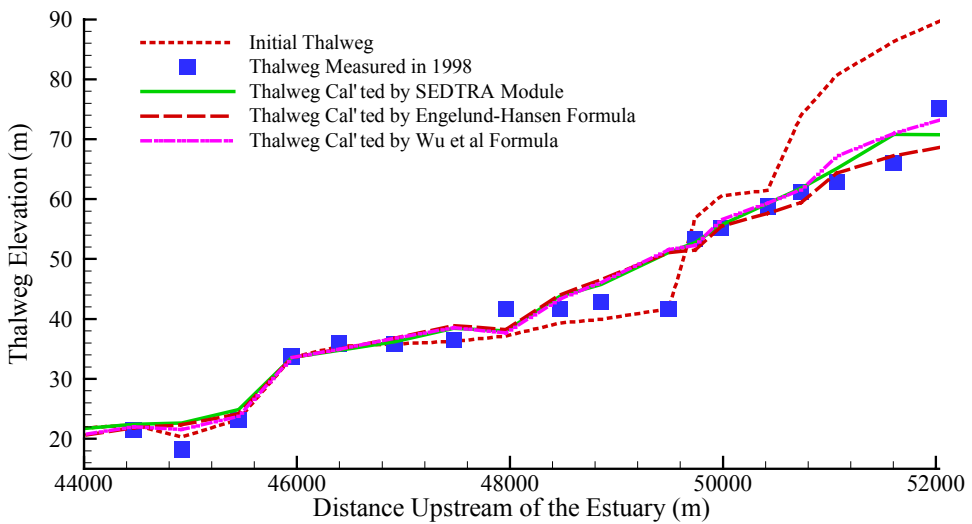


Fig. 8.15 Measured vs. Calculated Thalwegs in Pa-Chang River in 1995-1998

### 8.2.3 Effectiveness of Channel-Stabilization Structures in the Pa-Chang River

After the CCHE1D model had been tested and calibrated using the measurement data of the Pa-Chang River for the period 1995-1998, the model was applied to analyze the effectiveness of the 6 installed structures as well as a case with 12 planned structures for channel stabilization. Four scenarios were simulated. Scenario 1 was without any structures in the channel, scenario 2 contained the currently installed 6 structures, and scenario 3 contained the 18 structures (6 installed plus 12 planned structures). Scenario 4 studied the effectiveness of the 6 installed structures during a hypothetical re-occurrence of the 1996 typhoon Hopo. In these four scenarios, the channel geometry measured in 1998 and the bed-material size distribution measured in 1987 were used as initial conditions. For the scenarios 1, 2 and 3, the time series of incoming flow and sediment discharges from the 1995-1998 data were repeated twice to obtain results for a period of about 10 years. However, the storm related to typhoon Hopo of 1996 was used only once.

Fig. 8.16 shows the initial thalweg and the simulated thalwegs of scenarios 1, 2, and 3 after ten years. It is found that in scenario 1 (without channel-stabilization structures), the channel bed in the upper part of the study reach had large erosion. The maximum erosion depth at the Station No. 100 might be up to 26.5m after 10 years. In scenario 2, the channel bed around the Hsin-Soun Bridge (50.7km from the estuary) was stabilized by the 6 installed structures. But erosion still existed in the upper part where the effect of the installed structures cannot reach. In scenario 3, with all the 18 installed and planned structures, the channel was stabilized near the Hsin-Soun Bridge as well as in the upstream part. Erosion existed downstream of some structures. The reason might be that no coarse sediment (bed load) was supplied at the inlet of the simulation reach (the data of inflow sediment was not available) and the fine particles on the bed might be entrained into the flow and be carried downstream.

Fig. 8.17 shows the simulated bed change after the re-occurrence of typhoon Hopo (scenario 4). It is observed that erosion happens in the upper part and around some of the six installed stabilization structures, while deposition exists in several places in the mid-reach.

It should be noted that not all the needed information was available for the test, and that the simulation results reported here could be more accurate, if all necessary input data were available. In practice, it is likely that in most of the field investigations the available data are incomplete. This application study has shown that even under this situation, CCHE1D can still be used to obtain predictions with acceptable accuracy.

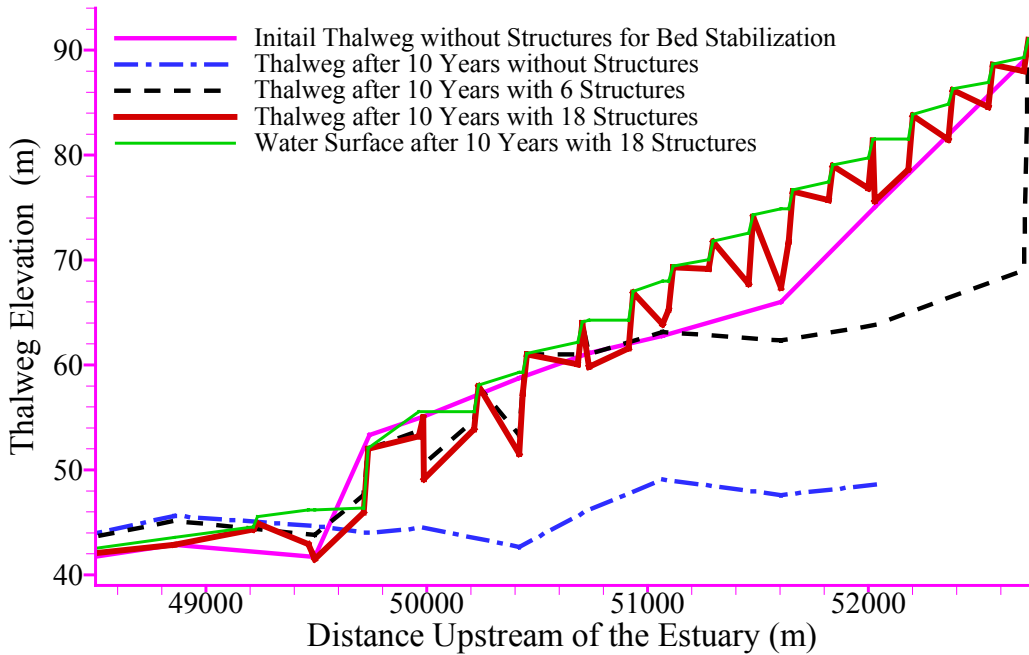


Fig. 8.16 Comparison of Calculated Thalwegs without and with Structures

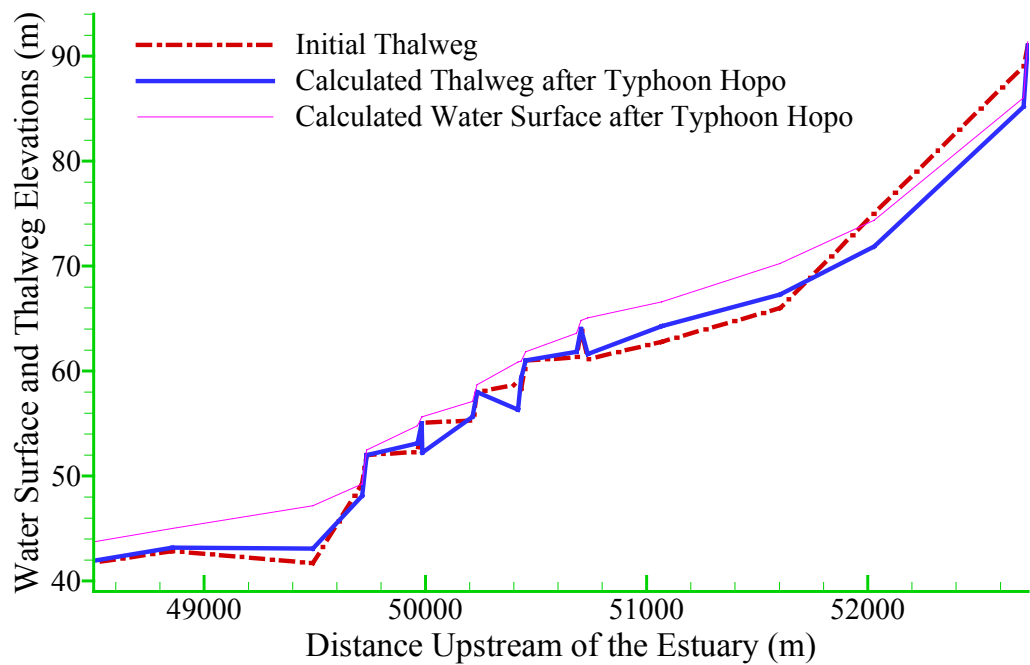


Fig. 8.17 Thalweg Change after the Re-occurrence of Typhoon Hopo

## References

- Ackers, P. and White, W.R. (1973). "Sediment transport: A new approach and analysis," *J. of Hydraulics Division, ASCE*, 99(HY11), pp. 2041-2060.
- Arminini, A. and Di Silvio, G. (1988). "A one-dimensional model for the transport of a sediment mixture in non-equilibrium conditions," *J. of Hydraulic Research*, 26(3).
- Arnold, J.G., Allen, P.M. and Bernhardt, G. (1993). "A comprehensive surface-groundwater flow model." *J. of Hydrology*, 142, pp. 47-69.
- Arulanandan, K., Gillogley, E. and Tully, R. (1980). "Development of a quantitative method to predict critical shear stress and rate of erosion of naturally undisturbed cohesive soils," *Rep. GL-80-5*, U.S. Army Corps of Engineers, Waterway Experiment Station, Vicksburg, Mississippi.
- Ashida, K. and Michiue, M. (1971). "An investigation of river bed degradation downstream of a dam," *Proc. 14th Congress of the IAHR*.
- Bagnold, R.A. (1966), "An approach to the sediment transport problem from general physics," *U.S. Geological Survey Professional Paper 422-J*.
- Barnes, Harry H., Jr. (1967). "Roughness characteristics of natural channels," *USGS Water Supply Paper 1849*, Washington, D.C.
- Bell, S.G. and Sutherland, A.J. (1983). "Non-equilibrium bed load transport by steady flows," *J. of Hydraulic Engineering*, 109(3), pp.353-367.
- Bingner, R. L., Alonso, C.V., Arnold, J. G. and Garbrecht, J. (1997). "Simulation of fine sediment yield within a DEC watershed," *Proc., Conference on Management of Landscapes Disturbed by Channel Incision*, pp. 1106-1110.
- Bosch, D., Theurer, F., Bingner, R.L., Felton, G. and Chaubey, I. (1998). "Evaluation of the AnnAGNPS Water Quality Model." *ASAE Paper No. 98-2195*, St. Joseph, Michigan.
- Brownlie, W.R. (1981), "Compilation of fluvial channel data: laboratory and field," *Rep. No. KH-R-43B*, W.M. Keck Lab. of Hydr. and Water Resources, California Institute of Technology, Pasadena, Calif.
- Chang, H.H. (1988). *Fluvial Processes in River Engineering*, Krieger Publishing Company.
- Cheng, C.C., Hsie, C.L., Hsie, H.M., et al. (2000), "The Establishment of a Flood-Warning System for Pa-Chang and Pu-Tze River Basins," Report, National Information Infrastructure Enterprise Promotion Association, Taiwan,
- Chien, N. and Wan, Z.H. (1983). *Mechanics of Sediment Movement*, Science Publications, Beijing. (in Chinese)
- Choudhury, S.A. (1996). *Modeling and Simulation of Aggradation and Degradation of Straight and Meander Alluvial Rivers*, Thesis of Master Degree, The University of Mississippi.
- Chow, V.T. (1959). *Open-Channel Hydraulics*, McGraw-Hill, New York.

- Colby, B.R. (1963), Discussion of "Sediment Transportation Mechanics: Introduction and Properties of Sediment," Progress Report by the Task Committee on Preparation of Sedimentation Manual of the Committee on Sedimentation of the Hydraulics Division, Vito A. Vanoni, Chmn., Journal of the Hydraulics Division, ASCE, Vol. 89, No. HY1, Proc. Paper 3405, pp. 266-268.
- Cunge, J.A., Holly, F.M. Jr. and Verwey, A. (1980). *Practical Aspects of Computational River Hydraulics*, Pitman Publishing Inc., Boston, MA.
- Danjiangkou Hydrology Experiment Station (1991), *Characteristic Values of the Danjiangkou Reservoir*, Yangtze River Water Resource Commission.
- Einstein, H.A. (1942). "Method of calculating the Hydraulic radius in a cross section with different roughness," Appen. II of the paper "Formulas for the transportation of bed load," *Trans. ASCE*, 107.
- Engelund, F. and Fredsøe, J. (1976), "A sediment transport model for straight alluvial channels," *Nordic Hydrology*, Vol.7, 293-306.
- Engelund, F. and Hansen, E. (1967). *A monograph on sediment transport in alluvial streams*. Teknisk Vorlag, Copenhagen, Denmark.
- Fasken, G.B. (1963). *Guide for selecting roughness coefficient n values for channels*, Soil Conservation Service, US department of Agriculture.
- FHWA (1985). *Hydraulic Design of Highway Culverts, Hydraulic Design Series No.5*, US Department of Transport.
- French, R.H. (1985). *Open-Channel Hydraulics*, McGraw-Hill Book Company, New York.
- Garbrecht, J., Kuhnle, R. and Alonso, C. (1995). "A sediment transport capacity formulation for application to large channel networks." *J. of Soil and Water Conservation*, 50(5), pp. 527-529.
- Garbrecht, J. and Martz, L. W. (1995). "An automated digital landscape analysis tool for topographic evaluation, drainage identification, watershed segmentation and subcatchment parameterization," *Report No. NAWQL 95-1*, National Agricultural Water Quality Laboratory, USDA, Agricultural Research Service, Durant, Oklahoma.
- Grissinger, E.H., Bowie, A.J. and Murphy, J. B. (1991). "Goodwin Creek bank instability and sediment yield," *Proc., Fifth Federal Interagency Sedimentation Conference*, pp. PS32-PS39.
- Han, Q.W. (1980). "A study on the non-equilibrium transportation of suspended load," *Proc. of the First International Symposium on River Sedimentation*, Beijing, China. (in Chinese)
- Han, Q.W., Wang, Y.C. and Xiang, X.L. (1980). "Reservoir sedimentation," *Technical Report*, Hydrology Department, Commission on Yangtze River Water Resources. (in Chinese)
- Han, Q.W., Wang, Y.C. and Xiang, X.L. (1981). "Initial dry density of sediment deposit," *J. of Sediment Research*, No. 1. (in Chinese)

- Hayashi, T.S., Ozaki and T. Ichibashi (1980). "Study on bed load transport of sediment mixture," *Proc. 24th Japanese Conference on Hydraulics*.
- Hicks, D.M. and Mason, P.D. (1991). "Roughness characteristics of New Zealand rivers," *Water Resources Survey*, DSIR Marine and Freshwater, New Zealand.
- HR Wallingford (1990). "Sediment transport, the Ackers and White theory revised," *Report SR237*, HR Wallingford, England.
- Karim, F. (1998), "Bed material discharge prediction for nonuniform bed sediments," *J. of Hydraulic Engineering*, ASCE, Vol.124, No.6, pp.597-604.
- Komura, S. and Simmons, D.B. (1967). "River-bed degradation below dams," *J. Hydr. Div.*, ASCE, 93(4), pp.1-13
- Kuhnle, R.A. (1993a). "Incipient motion of sand-gravel sediment mixtures," *Journal of Hydraulic Engineering*, ASCE, 119, 1400-1415.
- Kuhnle, R.A. (1993b). "Fluvial transport of sand and gravel mixtures with bimodal size distributions," *Sedimentary Geology*, 85, 17-24.
- Kuhnle, R.A., Garbrecht, J. and Alonso, C.V. (1996). "A transport algorithm for variable sediment sizes: Application to wide sediment size distributions," *Proc. Sixth Federal Interagency Sedimentation Conference*, Las Vegas, Nevada.
- Langendoen, E.J. (1996). "Discretization diffusion wave model," *Technical Report No. CCHE-TR-96-1*, Center for Computational Hydroscience and Engineering, The University of Mississippi.
- Langendoen, E.J. (1996). "Distributed flow routing in the Goodwin Greek, Mississippi," *Proc. Sixth Federal Interagency Sedimentation Conference*, Las Vegas, Nevada.
- Langendoen, E.J. (1997). "DWAVNET: Modification to friction slope formulation and solution method," *Technical Report No. CCHE-TR-97-1*, Center for Computational Hydroscience and Engineering, The University of Mississippi.
- Laursen, E. (1958). "The total sediment load of streams," *J. of Hydraulics Division*, ASCE, Vol. 108, 36p.
- Li, C.H. and Liu. J.M. (1963). "Resistance of alluvial rivers," *Technical Report*, Nanjing Hydraulic Research Institute, China. (in Chinese)
- Li, L., Bingner, R., Langendoen, E.J., Alonso, C.V. and Wang, S.S.Y. (1996). "Modeling sediment transport and channel evolution," *Proc. Sixth Federal Interagency Sedimentation Conference*. Las Vegas, Nevada.
- Liu, X.L. (1986), *Nonuniform Bed Load Transport Rate and Coarsening Stabilization*, Thesis for Master Degree, Chengdu University of Technology. (in Chinese)
- Lyn, D.A. and Goodwin, P. (1987). "Stability of a general Preissmann scheme," *J. of Hydraulic Engineering*, ASCE, 113(1), pp.16-28.
- Meade, R.H., Myrick, R.M. and Emmett, W.W. (1980). "Field data describing the movement and storage of sediment in the East Fork River, Wyoming, Part II. Bed elevations, 1979." *USGS Open-File Report 80-1190*, Denver, Colorado.

- Meselhe, E.A. and Holly, F.M., Jr. (1993). "Simulation of unsteady flow in irrigation canals with dry bed," *J. of Hydraulic Engineering*, ASCE, 119(9), pp. 1021-1039.
- Meyer-Peter, E. and Mueller, R. (1948). "Formulas for bed-load transport," *Report on Second Meeting of IAHR*, Stockholm, Sweden, 39-64.
- Newton, C.T. (1951). "An experimental investigation of bed degradation in an open channel," *Trans.*, Boston Society of Civil Engineers, pp. 28-60.
- Osman, A.M. and Thorne, C.R. (1988). "Riverbank stability analysis, I: Theory," *J. of Hydraulic Engineering*, ASCE, 114(2), pp. 134-150.
- Parker, G., Kilingeman, P.C. and McLean, D.G. (1982). "Bed load and size distribution in paved gravel-bed streams," *J. of Hydraulics Division*, ASCE, 108(4), pp.544-571.
- Patankar, S.V. (1980). *Numerical Heat Transfer and Fluid Flow*, Hemisphere Publishing Corporation.
- Phillips, B.C. and Sutherland, A.J. (1989). "Spatial lag effects in bed load sediment transport," *J. of Hydraulic Research*, IAHR, 27(1), pp.115-133.
- Preissmann, A. (1961). "Propagation des intumescences dans les canaux et Les Rivieres," *I Congres de l'Association Francaise de Calcule*, Grenoble, France.
- Proffit, G.T. and Sutherland, A.J. (1983), "Transport of nonuniform sediment," *J. of Hydraulic Research*, IAHR, 21(1), pp. 33-43.
- Rahuel, J.L. and Holly, F.M., et al (1989). "Modeling of riverbed evolution for bedload sediment mixtures," *J. of Hydraulic Engineering*, ASCE, 115(11), pp.1521-1542.
- Samaga, B.R., Ranga Raju, K.G. and Garde R.J. (1986a), "Bed load transport rate of sediment mixture," *J. of Hydraulic Engineering*, No.11, pp.1003-1018.
- Samaga, B.R., Ranga Raju, K.G. and Garde R.J. (1986b), "Suspended load transport rate of sediment mixture," *J. of Hydraulic Engineering*, No.11, pp.1019-1038.
- Seal, R., Parker, G. , Paola, C. and Mullenbach, B. (1995). "Laboratory experiments on downstream fining of gravel, narrow channel runs 1 through 3: supplemental methods and data," External Memorandum M-239, St. Anthony Falls Hydraulic Lab., University of Minnesota.
- Seal, R., Paola, C., Parker, G. and Southard, J.B. (1997). "Experiments on downstream fining of gravel, I: Narrow-channel runs," *J. of Hydraulic Engineering*, ASCE, 123(10), 874-884.
- Shields, A. (1936). "Anwendung der Aechlichkeitsmechanik und der Turbulenz Forschung auf die Geschiebebewegung," Mitteilungen der Pruessischen Versuchsanstalt fuer Wasserbau and Schiffbau, Berlin.
- Stephen, E.D. and Thorne, C.R. (1996), "Numerical simulation of widening and bed deformation of straight sand-bed rivers, I: Model development," *J. of Hydraulic Engineering*, ASCE, 122(4), pp. 184-193.
- Toffaleti, F.B. (1968). "A procedure for computation of the total river sand discharge and detailed distribution, bed to surface," *Technical Report No.5*, US Army Corps of Engineers, Vicksburg, Miss.

- Tran Thuc (1991). *Two-Dimensional Morphological Computations near Hydraulic Structures*, Doctoral Dissertation, Asian Institute of Technology, Bangkok, Thailand.
- U.S. Interagency Committee on Water Resources, Subcommittee on Sedimentation (1957). Some Fundamentals of Particle Size Analysis, *Report No.12*.
- Vanoni, V.A. (ed.) (1975). *Sedimentation Engineering*, ASCE manuals and reports on engineering practice, No. 54.
- Van Rijn, L.C. (1981). "Entrainment of fine sediment particles; development of concentration profiles in a steady, uniform flow without initial sediment load," Report No. M1531, Part II, Delft Hydraulic Laboratory.
- Van Rijn, L.C. (1984a). "Sediment transport, part I: bed load transport," *J. Hydr. Engi.*, ASCE, Vol 110, No. HY10, pp. 1431-1456.
- Van Rijn, L.C. (1984b). "Sediment transport, part III: bed forms and alluvial roughness," *J. Hydraulic Engineering*, ASCE, 110(12), pp.1733-1754.
- Vieira, D.A. and Wu, W. (2000), "One-dimensional channel network model CCHE1D 2.0 – User's manual," *Technical Report No. NCCHE-TR-2000-2*, National Center for Computational Hydroscience and Engineering, The University of Mississippi.
- Wang, S. S.-Y., Wu, W., Hsia, H.M., and Cheng, C.C. (2002), "Simulation of Flood and Sediment Routing in the Pa-Chang River and the Pu-Tze River of Taiwan using CCHE1D Model," accepted for publication, *The Fifth International Conference on Hydroscience and Engineering*, Warsaw, Poland.
- Wang, Z.B. and Ribberink, J.S.(1986). "The validity of a depth-integrated model for suspended sediment transport," *J. of Hydraulic Research*, IAHR, 24(1).
- Wang, Z.Y. (1999). "Experimental study on scour rate and river bed inertia," *J. of Hydraulic Research*, IAHR, 37(1), 17-37.
- Wei, Z.L. (1999). Private Communication.
- Wellington, N.W. (1978). *A Sediment-Routing Model for Alluvial Streams*, M. Eng. Sc. Dissertation, University of Melbourne, Australia.
- Wilcock, P.R. (1993), "Critical shear stress of natural sediments," *J. of Hydraulic Engineering*, Vol. 119, pp. 491-505.
- Wilcock, P.R. and McArdell, B.W. (1993), "Surface-based fractional transport rate: mobilization thresholds and partial transport of a sand-gravel sediment," *Water Resources Research*, Vol. 29, No.24, pp.1297-1312.
- Wilcock, P.R., and Southard, J.B. (1988). "Experimental study of incipient motion in mixed-size sediment," *Water Resources Research*, 24, 1137-1151.
- Williams, G.P. (1970). "Flume width and water depth effects in sediment transport experiments," *Professional Paper No. 562-H*, U.S. Geological Survey.
- Williams, G.P. and Rosgen, D.L. (1989), "Measured total sediment load (suspended loads and bed loads) for 93 United States streams," *USGS Open-File Report 89-67*.

- Wu, W. and Li, Y. (1992a). "A New One-Dimensional Numerical Modeling Method of River Flow and Sedimentation," *Journal of Sediment Research*, No. 1, pp.1-8. (in Chinese)
- Wu, W. and Li, Y. (1992b). "One- and Two-Dimensional Nesting Mathematical Model for River Flow and Sedimentation," *The Fifth International Symp. on River Sedimentation*, Karlsruhe, Germany, Vol. 1, pp.547-554.
- Wu, W. and Wang, S. S.Y. (1999). "Movable Bed Roughness in Alluvial Rivers," *Journal of Hydraulic Engineering*, ASCE, 125(12), 1309-1312.
- Wu, W., Rodi, W. and Wenka, Th. (2000). "3D numerical modeling of flow and sediment transport in open channels," *Journal of Hydraulic Engineering*, ASCE, 126(1), 4-15.
- Wu, W., Wang, S.S.-Y. and Jia, Y. (2000). "Nonuniform Sediment Transport in Alluvial Rivers." *J. of Hydraulic Research*, IAHR, Vol. 38, No. 6.
- Wu, W. and Wang, S. S.-Y. (2001), "Selection and Test of Nonuniform Sediment Transport Formulas," *The Eighth Int. Symp. on River Sedimentation*, Cairo, Egypt, Nov. 3-5.
- Wu, W., Vieira, D.A. and Wang, S.S.-Y. (1998). "New Capabilities of the CCHE1D Channel Network Model." *ASCE's 2000 Joint Conference on Water Resources Engineering and Water Resources Planning and Management*, Minneapolis, USA. (on CD-ROM)
- Wu, W. and Vieira, D.A. (2000), "One-dimensional channel network model CCHE1D 2.0 — Technical manual," *Technical Report No. NCCHE-TR-2000-1*, National Center for Computational Hydroscience and Engineering, The University of Mississippi.
- Yalin, M.S.(1972). *Mechanics of Sediment Transport*, Pergamon Press.
- Yang, C.T. (1973). "Incipient motion and sediment transport," *J. of Hydraulics Division*, ASCE, 99(HY10), pp. 1679-1704.
- Yang, C.T. (1995). *Sediment Transport: Theory and Practice*, The McGraw-Hill Companies, Inc.
- Yang, C.T., Trevino, M.A. and Simoes, F.J.M. (1998). *User's Manual for GSTARS 2.0 (Generalized Stream Tube Model for Alluvial River Simulation version 2.0)*, Sedimentation and River hydraulics Group, Technical Service Center, Bureau of Reclamation, U.S. Department of the Interior, Denver, Colorado, USA.
- Young, R.A., Onstad, C.A., Bosch, D.D. and Anderson, W.P. (1987). "AGNPS, Agricultural non-point source pollution model, A watershed analysis tool," Conservation Research Report 35, Agricultural Research Service, US Department of Agriculture, Washington, D.C.
- Zhang, R., Xie, J., Wang, M. and Huang, J. (1989). *Dynamics of River Sedimentation*, Water Resources and Electric Power Publication, Beijing. (in Chinese)
- Zhang, Y. and Langendoen, E.J. (1997). "An introduction to BEAMS," *Technical Report*, Center for Computational Hydroscience and Engineering, The University of Mississippi.